TIME-REVERSAL TECHNIQUES IN SEISMIC DETECTION OF BURIED OBJECTS

A Thesis
Presented to
The Academic Faculty

by

Pelham D. Norville

In Partial Fulfillment
of the Requirements for the Degree
Doctor of Philosophy in the
School of Electrical and Computer Engineering

Georgia Institute of Technology
May 2007

TIME-REVERSAL TECHNIQUES IN SEISMIC DETECTION OF BURIED OBJECTS

Approved by:

Professor Waymond R. Scott, Jr., Advisor
School of Electrical and Computer Engineering
Georgia Institute of Technology

Professor James H. McClellan
School of Electrical and Computer Engineering
Georgia Institute of Technology

Professor Glenn S. Smith
School of Electrical and Computer Engineering
Georgia Institute of Technology

Professor Laurence J. Jacobs
School of Civil and Environmental Engineering
Georgia Institute of Technology

Professor W. Marshall Leach, Jr.
School of Electrical and Computer Engineering
Georgia Institute of Technology

Date Approved: 28 March 2007

ACKNOWLEDGEMENTS

This dissertation is the result of my graduate studies at the Georgia Institute of Technology. The completion of this work would not have been possible without the assistance and support of a great number of people to whom I would like to express my gratitude.

My deepest thanks go first to Professor Waymond R. Scott, Jr. who has served as my thesis advisor and mentor during my time at Georgia Tech. Dr. Scott's dedication to his profession and to his students is readily apparent in all his work. His command of acoustics and electromagnetics have guided me throughout my studies. In addition to his scientific guidance, I am grateful for his frequent advice and counsel and his constant encouragement.

I wish to also thank the member of my dissertation committee, Prof. Glenn S. Smith, Prof. James H. McClellan, Prof. W. Marshall Leach, and Prof. Laurence J. Jacobs for their time, effort and constructive criticism. My gratitude is also extended to Dr. Mubashir Alam and Dr. James McClellan for their help in designing the Wiener filter that was used in processing much of the initial experimental data presented in this work.

Dr. Gregg D. Larson and James S. Martin along with Prof. Scott were instrumental in completing all of the measurements in the experimental facility. Both Mr. Martin and Dr. Larson were essential in the design and implementation of experimental measurement system hardware, and Dr. Larson's assistance in creating LabView software to drive the system and much of the MatLab code used for processing the data is also greatly appreciated. Their knowledge of these systems and their continual support were extremely helpful in the completion of this work.

I owe many thanks to Dr. Christoph Schröeder who developed numerical modelling software used in the numerical simulations. I must also thank those who helped to maintain the Beowulf computer cluster used to perform the computations for the numerical models used in this dissertation. Benny Venkatesan built the first cluster, and is has subsequently been upgraded and maintained by a number of others including IT professional Didier Contis, and fellow graduate students Todd Lee, Mike McFadden and David Reid. In particular, Todd and Mike made significant improvements that resulted in the latest iteration of the cluster. Their work in improving and maintaining this computer as a resource for all the students in our research group is greatly appreciated.

I would also like to thank all my colleagues and fellow graduate students who have contributed to this work through their technical expertise and through their friendship, thoughtful discussion, and support: Thorsten Hertel, L.E. Rickard Petersson, Kangwook Kim, Benjamin Declety, Benny Venkatesan, Todd Lee, Ricardo Lopez, David Reid, Tegan Counts, and Mike McFadden.

Laura Jenkins has also been a source of inspiration for me through her patience, kindness and encouragement. Her support has been invaluable to me and I thank her for it. Finally, I would like to thank my parents, Warren and Susan Norville and my sister, Sarah Norville Peinhardt for their unconditional love, support and faith in me in all my endeavors. I want to thank my parents for instilling in me a love of learning, a desire to be inquisitive, and a drive to always do my best. Their support is unwavering and is a constant source of strength for me.

TABLE OF CONTENTS

LIST OF TABLES

LIST OF FIGURES

SUMMARY

This dissertation presents an investigation of the behavior of time-reversal focusing in soils. A basic study of time-reversal using a linear finite-difference time-domain (FDTD) model of the soil is presented. Initial numerical models show time-reversal focusing to be effective in elastic media, including when a large number of scattering objects were present in the medium. When scattering objects are present, time-reversal focusing demonstrates superior focusing ability when compared to other excitation methods such as uniform excitation or time-delay focusing.

The numerical studies are followed by multiple investigations of experimental time-reversal focusing performed in sand. Time-reversal focusing effectiveness is evaluated first for experimental conditions similar to the numerical model, with multiple near-surface scattering objects present in the medium. Time-reversal focusing is shown to be effective in the experimental context as well. Further experiments examine time-reversal focusing in the more extreme case where the entire ballistic wave is blocked, and the only energy reaching the focus point is reflected from scattering objects in the medium.

Time-reversal focusing is effective in focusing the remaining energy to the focus location which was in a shadowed region behind the large barrier that blocked the ballistic wave. A comparison to other focusing methods demonstrates that under these conditions, most focusing attempts with traditional methods will fail completely while time-reversal focusing does not. Additional configurations of time-reversal focusing examine its effectiveness when scattering is caused by an asymmetrical surface layers. The impact of an asymmetrical or non-uniform excitation array is also examined for time-reversal focusing in the presence of scattering objects.

An investigation of the effects of scattering object geometry is undertaken to examine the effect scattering object shape, orientation, and number of scattering objects on focusing resolution in time-reversal focusing. Scattering object field density is found to have a strong, but diminishing effect on focusing resolution as the scattering object field density increased. Loss of surface wave energy available for focusing due to mode-conversion is found to be correlated with the density of the scattering object field.

Soil is a complicated non-linear medium which normally behaves in a quasi-linear fashion for the range of amplitudes in which the earlier experiments were performed. The impact of the weak non-linear nature of the soil on time-reversal focusing is examined through a study of time-reversal focusing behavior for a variety of amplitudes that generate different levels of non-linearity in the soil. This study of nonlinearity is coupled with a study of the impact of noise on time-reversal focusing. It appears that both non-linearity and noise have an impact on time-reversal focusing effectiveness. Further, the loss from these mechanisms seems to be interrelated. Noise seems to enhance non-linear loss in the soil.

CHAPTER I

INTRODUCTION

Time-reversal focusing is a powerful technique that allows propagating waves to be focused to a particular location, even in the presence of clutter. Time-reversal focusing is most useful when it is difficult or impossible to characterize the clutter and wave propagation speed in an area of examination. While other focusing methods require some knowledge of the propagation medium characteristics such as propagation speed, time reversal does not require this information. Because of it's insensitivity to clutter and inhomogeneity, elastic-wave time reversal shows great promise for application to the detection of buried objects.

Time-reversal phenomena have been examined in several studies. Primarily, these papers have focused on time reversal in inhomogeneous media in the ultrasound regime. The medium in most of these analyses is a fluid, and therefore does not support shear waves as in buried object detection. The underlying principles that are demonstrated in these studies indicate that time-reversal focusing should be effective in the detection of buried targets.

1.1 Historical Overview

Time-reversal focusing for inhomogeneous media was first proposed as a broadband acoustical analog to the optical phase conjugated mirror [4]. An optical phase conjugated mirror is a single-frequency device that records data on an array of sensors, conjugates the phase of this data, and re-transmits it. This phase conjugation in frequency is equivalent to reversing the signal in time. For optical devices, this must be performed for each frequency since optical sensing devices are generally narrow-band sensors. The time-reversal method for acoustic waves differs in that the entire

process is often completed in the time domain, thanks to the relatively broadband capabilities of acoustic sensors. Instead of performing phase conjugation on recorded data, the entire time record of a received signal is reversed in time ($t \Rightarrow -t$) and then re-transmitted.

Fink *et al.* first developed time-reversal focusing in inhomogeneous media using the concept of a time-reversal mirror (TRM). The development of this process stems from basic wave propagation theory. The governing wave equation for acoustic pressure waves in a fluid serves as the starting point for a basic analysis of time reversal,

$$\nabla p - \frac{1}{c^2\left(\vec{r}\right)} \frac{\partial^2 p}{\partial t^2} = 0 \tag{1}$$

where $p\left(\vec{r}, t\right)$ represents acoustic pressure in space and time, and $c\left(\vec{r}\right)$ is the wave speed as a function of position.

This equation is valid for the case in which there are no external forces present on the medium. It also assumes that the medium is lossless with respect to wave propagation. The assumption of a lossless medium is not physical, but if the losses are very small, the additional terms in the equation have a negligible effect and can be ignored.

An examination of the wave equation shows that there are only second order time derivatives present. Because of the lack of odd order time derivatives, if there is a solution to this equation $p\left(\vec{r}, t\right)$, then $p\left(\vec{r}, -t\right)$ must also be a solution to this equation. Experimentally, it is impossible to record a signal for an infinite duration before time-reversing the signal. This requirement of an infinitely long signal may be relaxed if all energy in the spatial region of interest is small outside of this some finite time interval, $(0, T)$. In this case, a signal is recorded over the $(0, T)$ interval and then time reversed. After being time reversed, this time-limited signal, $p\left(\vec{r}, T - t\right)$ should be almost exactly equal to $p\left(\vec{r}, -t\right)$.

In order to record the signals to be time reversed, a 3-D surface is constructed around a location of interest, usually a source location (Figure 1). This surface

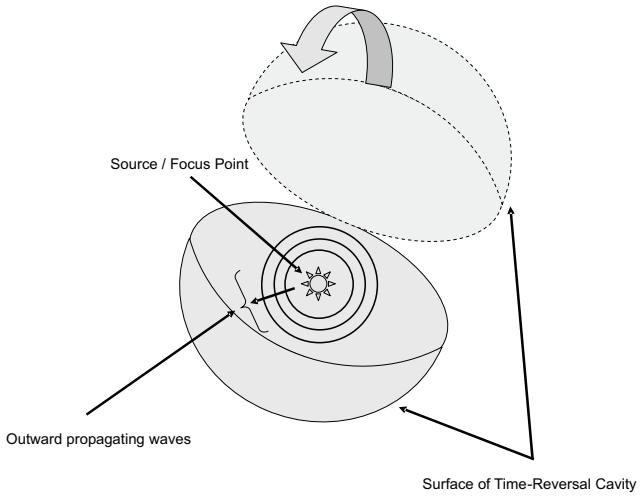

Figure 1: The time-reversal cavity: a 3-D surface surrounding the source location. All waves that impinge on the surface of the TRC are recorded, time reversed and re-transmitted. They will then focus at the source location.

is known as a time-reversal cavity (TRC) [5, 6]. All waves that impinge on the interior of the 3-D surface are recorded. If these waves are time reversed ($t \Rightarrow -t$) and simultaneously transmitted from their respective locations on the 3-D surface, they will focus back to the original source location [7]. This result seems somewhat intuitive, but would be difficult or impossible to realize in the form of an experiment because it is difficult to receive and then transmit a continuum of signals on the 3-D surface. In addition to this difficulty, it should be noted that even if all the propagating waves are recorded on the surface of the cavity, the time-reversed signal will not be an exact solution since evanescent waves attenuate too rapidly to be accurately recorded or reproduced any distance from the source, and therefore cannot be time reversed.

A 3-D TRC is not trivial to construct. In fact, such a cavity is impractical for most time-reversal focusing applications - particularly in elastic materials. This leads to the development of the time-reversal mirror (TRM)[5]. The TRM is a simplification of the 3-D TRC that can be feasibly implemented. The TRM (Figure 2) is a 1 or 2-D array of sources/sensors that can record and transmit acoustic signals. The TRM is

the realized portion of the more ideal TRC. The TRM exhibits limitations that are commonly associated with classical time-delay focusing techniques. [5]:

- Diffraction effects create a limit, proportional to wavelength, beyond which the spot size cannot be further reduced.

- Unlike the enclosed TRC, the TRM has a finite aperture, which causes increased spot size at the focal point. The focusing resolution is proportional to the angular aperture size of the TRM.

- As in classical focusing techniques, grating lobes may be introduced for frequencies where the spacing between TRM array elements is greater than $\lambda/2$, where λ is the wavelength at the frequency of interest. Further, if the dimensions of the recording face of the transducers themselves are greater than $\lambda/2$, the resolution of the array is reduced due to averaging of the incident field across the face of the transducer.

Even with these limitations, the TRM provides a robust method for focusing acoustic waves. In [6], Wu, *et al.* demonstrate the effectiveness of time reversal in focusing ultrasonic pressure waves on solid targets in a fluid. This study demonstrates the usefulness of time-reversal focusing in applications to lithotripsy. The challenge in lithotripsy is to focus energy through various types of body tissue to the location of a kidney stone. The experiments are conducted in water with large piezoelectric transducer arrays (64 – 128 transducers) over a frequency range of 1 – 3.5 MHz. The physical setup is similar to that depicted in Figure 2. In order to introduce variations in sound speed, aberrating layers of rubber or silicone are introduced into the background medium. The targets used in the study are vertical metal wires 0.7 – 1.5 mm in diameter, or actual kidney stones suspended in water. Comparisons are made between time-delay focusing and the time-reversal focusing techniques. Time-delay focusing uses a knowledge of the propagation speed in the medium, along with

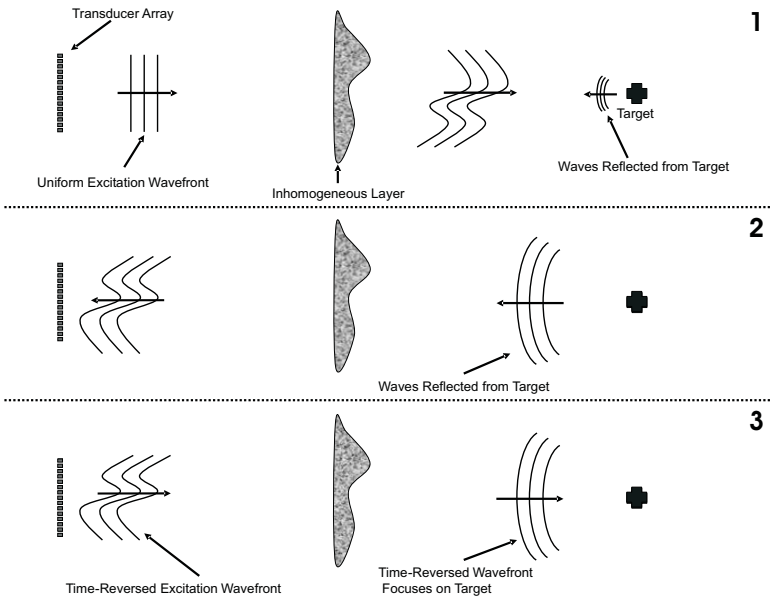

Figure 2: Time reversal using the time-reversal mirror (TRM). **1.** A uniform excitation wavefront is launched from the array, and travels through the inhomogeneous layer to arrive at the target. **2.** Waves are reflected from the target and travel back through the inhomogeneous layer to arrive at the TRM. **3.** The reflected waves are recorded on the TRM, time reversed and re-transmitted. They propagate through the inhomogeneous layer and focus on the target.

distances to a known target in order to calculate time delays such that the pulses from all the array elements arrive simultaneously. The authors of [6] demonstrate that time-delay focusing is unable to provide optimal focusing to an arbitrary location due to discrepancies in the assumed and actual sound speeds. Time reversal, however, is able to focus on the target much more effectively without requiring *a priori* knowledge of the wave speeds in the medium.

In addition to the advantage of not requiring *a priori* knowledge of the medium characteristics, time reversal can be used in an iterative sense to select the most highly reflective target in a medium. Each time that time reversal is performed, the time-reversed signal recorded during the previous iteration is used as the excitation. In this way, the signature from other scattering objects is reduced while improving the response at the location of the largest scatterer. This is especially useful in

applications such as lithotripsy where generally the object of interest is the largest stone (kidney stone, gall stone, etc.).

In their initial research, Fink *et al.* consider time-reversal focusing in a fluid medium[4, 5, 6]. Since fluid media only support pressure waves, a logical extension of the study of time reversal is to examine its effectiveness in an elastic medium. Elastic media support a variety of wave types, including Rayleigh surface waves. While wave propagation in elastic media differs from that in fluids, the underlying wave propagation equation is very similar,

$$\rho_s \frac{\partial^2 \vec{u}}{\partial t^2} = (\lambda + 2\mu)\left(\nabla\left(\nabla \cdot \vec{u}\right)\right) - \mu\left(\nabla \times \left(\nabla \times \vec{u}\right)\right) \tag{2}$$

where $\vec{u}$ is displacement, λ and μ are the Lamé constants of the medium and ρ_s is the density. This equation demonstrates the lack of odd-order time derivatives, just as in Equation 1.

The investigation of time-reversal focusing of Rayleigh waves in elastic solids was first motivated by the detection of surface and subsurface flaws in a solid [1, 8]. Such detection techniques are useful in developing advanced non-destructive testing methods. In experiments performed by Ing *et al.*[1], a solid duralumin plate serves as the propagation medium and piezoelectric transducers are coupled to the plate through a plexiglass wedge (Figure 3). The background medium is homogenous and the experiments are performed in the ultrasonic frequency regime. These experiments verify that for elastic waves directly coupled to a homogeneous solid, time-reversal focusing using a TRM in pulse-echo mode is an effective method for detecting surface and subsurface flaws.

In addition to the experimental setup formed by Ing, there is another common configuration used in non-destructive testing. Pressure waves are generated in a fluid, usually water, and propagate through the fluid to reach a solid medium (Figure 4). In this case, mode conversion at the liquid-solid interface [9] generates elastic waves inside the solid. The elastic waves propagate through the solid, being reflected if they

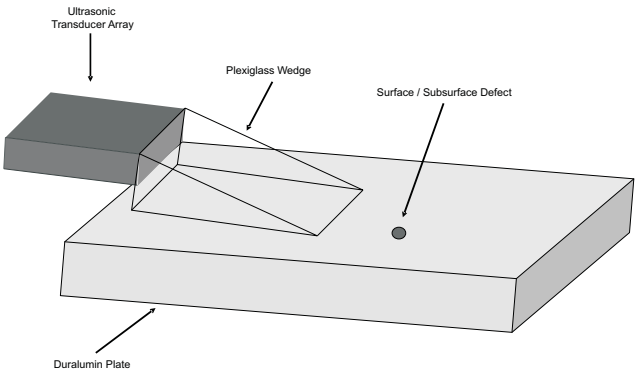

Figure 3: Setup for experiments performed by Ing, *et al.* [1] using a piezoelectric transducer array coupled to a Duralumin plate via a plexiglass wedge.

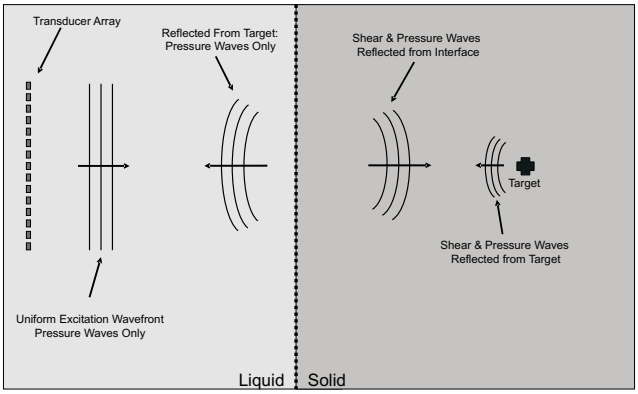

Figure 4: TRM setup incorporating a liquid-solid interface. The transducers are located in the fluid medium while the target is inside the solid medium.

interact with a target or scattering object in the medium. These reflected waves arrive at the liquid-solid interface where pressure waves are generated that travel back to the TRM where they are recorded. These waves are used to create the time-reversal signals that focus at the location of the target.

Theoretical calculations of the behavior of time reversal through a liquid-solid interface indicate that time-reversal performs well across this interface [7]. It should be noted for this experiment however that SH polarized shear waves[1] are not time-reversible since they are completely reflected inside the solid. This does create a

[1]Refer to [9] for a thorough explanation of elastic wave mechanics

small degradation of the focusing ability, but given that the wave type of interest, the Rayleigh wave, is a P-SV polarization wave, this effect is insignificant. Experimental results confirm the predicted effectiveness of time reversal through a liquid-solid interface [8].

The solid objects considered in the experiments are defect-containing titanium plates. In addition to the self-focusing that occurs through iteration of the time-reversal method, this work demonstrates a reduced level of speckle noise in the background as the iterative time-reversal focusing becomes stronger. The ability to reduce signatures from background clutter is an important quality of time reversal, and iterative time reversal in particular. Other experiments with similar configurations [10] confirm the results of [8].

Most of the experiments presented thus far concentrate on time-reversal focusing in homogeneous media. In [8], time-reversal is shown to improve results over classical focusing techniques by reducing speckle noise created by microstructural level inhomogeneities. Returning to experiments in water, Derode *et al.* [2] created an experiment incorporating a high number of discrete scattering objects (Figure 5). The resultant inhomogeneity leads to high-order scattering of the excitation wavefront. Specifically, the experiment is configured such that a TRM and a target location are separated by a layer of scatterers. Two scattering scenarios are created. The first is a random set of multiple parallel thin steel rods. The rods are 0.8 mm in diameter and cover 3.9% of the surface area within the defined region where scattering objects may be placed. The second scenario uses small glass spheres of 1.5 mm diameter distributed in an agar gel layer. The volume fraction of the scatterer region occupied by the spheres is 5.9%.

The initial goal of these experiments is to demonstrate that time reversal is robust enough to achieve strong focusing even in the presence of high-order scattering. The

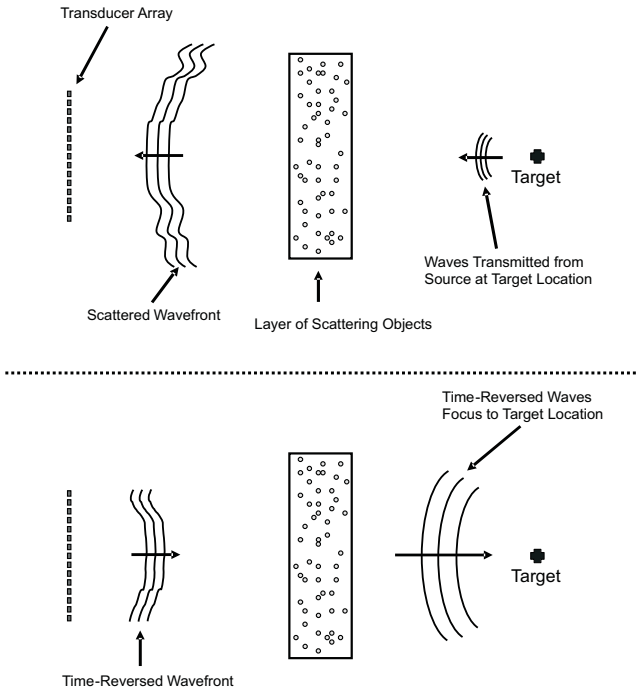

Figure 5: The experimental setup used by Derode *et al.* [2] incorporating a layer of discrete scattering objects. In the first half of the experiment a source is placed at the target location. The received signals are time-reversed and re-transmitted by the TRM. After passing through the scattering layer, the waves focus to the target location.

results demonstrate however, that high-order scattering can improve focusing resolution beyond the level observed in a homogeneous material. This super-resolution effect is caused by the multi-pathing that occurs in the inhomogeneous medium.

As the incident wave propagates through the scattering layer, it is reflected off multiple scattering objects before arriving at the target location. These multiple bounces cause the incident wave to subtend a greater arc angle upon arrival at the target than if arriving directly from the TRM transducer array. This greater arc angle causes a TRM to have an effective aperture that is significantly larger than the physical aperture [11].

Classical diffraction limits indicate that the spot size of a focus point is limited by the aperture of the TRM. From classical focusing, the minimum spot size of a focus point a distance L away from a TRM of aperture, a, with a center wavelength of λ is

proportional to $\frac{\lambda L}{a}$. The experimental results from [2] indicate that in the presence of high-order scattering, the resolution of the focusing can be increased to $\frac{1}{6}\frac{\lambda L}{a}$. This effect has been called super-resolution, for its ability to resolve a focal point beyond the diffraction limit.

The notion of super-resolution in time reversal has also been examined from a theoretical standpoint in [11, 12]. Blomgren, *et al.* [12] treat the inhomogeneous background as a random distribution of inhomogeneity with a standard deviation from the mean material properties. Through this statistical description of inhomogeneity and a system of simplifying assumptions, they derive a relationship between the effective aperture and the level of inhomogeneity in the medium. By determining the size of the effective aperture through observation of the focal point spot size, the level of inhomogeneity can be determined. While this theoretical relationship can be demonstrated through numerical simulations, a statistical distribution is significantly different from the larger-scale discrete inhomogeneities presented in [2] and other physical experiments.

The experiments performed thus far in acoustic time reversal were performed in both fluid and solid background media. Liquid-solid interfaces have also been explored. In fluid media, homogeneous backgrounds have been augmented with scattering objects to create high-order scattering of incident waves. In the solid media explored thus far, any inhomogeneity is the result of microstructural variations, which are much smaller than a wavelength.

These experiments provide a solid foundation in the investigation of acoustic time reversal, but the experimental cases that have been examined are still significantly different from those encountered in the buried object detection problem. For buried targets, the frequency range of interest is typically centered around 400 - 1000 Hz, and the detection problem must be carried out in an elastic solid background medium. Inhomogeneity may be encountered by the addition of hard solid objects, such as

rocks or other near-surface scatterers, by voids in the medium, or variations in the background material properties.

In ultrasonic target detection, the targets are typically located by a reflection off the target that arrives back at the location of a measurement array or TRM. In the buried object detection scheme proposed here, results are commonly evaluated by scanning over a surface and looking for structures that have been excited into resonance, usually indicating a potential target. The unique nature of the buried target detection problem encourages further study of time-reversal focusing behavior in configurations that are applicable to the detection of buried targets.

1.2 Contribution of Research

The work presented in this document investigates the performance of time-reversal focusing in soils, with a particular emphasis on the detection of buried targets. Because of the common inhomogeneity and scattering in soil media, focusing methods offer an attractive way to deliver high amplitude signals to a desired location. Time-reversal focusing is an appealing way to deliver these signals because it can provide tight and accurate focusing even in the presence of inhomogeneity.

While time-reversal focusing has been studied extensively in fluids, and even in some solid media, studying the phenomenon in soil entails a significantly different analysis. Only limited-scale studies in any type of granular media have been performed [13], indicating a need for further study. The complexity of wave propagation in soil goes beyond that of many common fluids or elastic media. Soil is a complicated non-linear particulate medium in which many interparticle forces along with specific physical characteristics define the behavior of waves supported in the medium [14]. In order to exploit the advantages of time-reversal focusing in soil, it must be studied in this medium. This includes an understanding of how signal amplitude affects non-linearity in soil. Experimental examinations of soil compared to numerical models

and analytical formulations have found that soil behaves in a nearly-linear way for small amplitude displacements.

Evaluation of time-reversal focusing in soils is approached through numerical modelling and through experimental work designed to evaluate the behavior of time reversal in soils under various conditions. Experiments examine the effectiveness of time-reversal focusing in the presence of a variety of scattering conditions combined with nearly-linear wave propagation. The effects of mode-conversion of surface-bound waves on time-reversal focusing are also examined. In addition, the non-linear nature of the soil also affords the opportunity to study the effects of non-linearity on the time-reversal process and these effects are also studied.

1.3 Outline

This first chapter has summarized the historical investigations of time-reversal focusing, and how the research in this document will further investigate time-reversal focusing in soils, with an emphasis on application to the detection of buried targets. Chapter 2 begins with an introduction to the problem of buried landmine detection, and an introduction to the experimental methods that have been developed in order to study buried object detection. The basic theory and implementation of time-reversal focusing are also introduced. Finally, a finite-difference time-domain numerical model is introduced. While the basic model has been previously documented in the literature [15], an additional component has been added to allow for the computation of power exiting the solution space. This addition to the model is described and validated.

Chapter 3 presents the results of a set of experiments designed to study time-reversal focusing in the presence of simple clutter. Time-reversal focusing's effectiveness is compared to other excitation methods. Numerical simulations using the finite-difference time-domain model provide an initial investigation of time-reversal

focusing. Experimental time-reversal focusing performed in the laboratory investigates time-reversal focusing behavior in the physical medium of soil, and includes an investigation of the effect of scattering objects on time-reversal focusing. Chapter 4 extends the investigations of time-reversal focusing in cluttered media to an extreme case where the primary incident "ballistic" wave is blocked by large scattering objects. Experimental results evaluate the effectiveness of time-reversal focusing in comparison to other focusing methods in this extreme case. New experimental methods are also introduced that yield faster experimental completion times and improved signal-to-noise ratios for experimental data.

Chapters 5 and 6 continue the experimental investigation of time-reversal focusing behavior under a variety of experimental conditions. Chapter 5 presents time-reversal focusing for large asymmetrical surface layers, which drastically alter the propagation direction of an incident wave. Chapter 6 evaluates time-reversal focusing in comparison to other excitation methods for the case where the scattering objects are present in the medium and the excitation array is no longer a regularly spaced array. The application of the non-uniform array is extrapolated to the case of semi-autonomous sensors and excitation sources for use in a buried object detection scenario where a uniform excitation array may not be feasible. To this point, much of the research presented evaluates time-reversal focusing for various scattering conditions. Chapter 7 evaluates the effect of the scattering object geometry on time-reversal focusing. Particular emphasis is placed on the impact of mode-conversion of surface-bound elastic waves into non-surface-bound waves. The effect of the number of scattering objects, as well as their shape and orientation is evaluated in this chapter.

Chapter 8 examines the effects of noise and non-linearity on time-reversal focusing. Soil has a complicated structure which behaves as a non-linear medium for sufficiently large excitation amplitudes. Noise is also inherent in any experimental measurement. This noise plays a particularly important role for a non-linear medium such as soil

where high amplitude drive signals will force the medium to behave in a non-linear manner. The effects of noise on time-reversal focusing are also evaluated, especially with respect to the relationship between signal-to-noise ratio and non-linear effects.

CHAPTER II

INVESTIGATIVE METHODS: ELASTIC WAVE PROPAGATION IN SOLIDS

2.1 The Landmine Detection Problem

A landmine detection system (Figure 6), under development at the Georgia Institute of Technology, functions by exciting elastic waves that propagate through the soil[3]. A feature of this system is a non-contact or lightly-contacting sensor that is used to measure ground motion, making it possible to sense motion directly above a landmine. While multiple wave types are generated by the system's excitation signal, the wave of primary importance in detecting landmines is the Rayleigh surface wave. This wave propagates near the surface along the boundary between the air and the soil and interacts with objects buried in the medium. For most objects, this interaction is observed as scattering of the Rayleigh wavefront off of the object. When the buried object is a landmine, due to it's structure, and the depth at which it is usually buried, the Rayleigh wave may excite a resonance in the layer of soil between the surface and the flexible top of a landmine. These resonances enhance the surface displacements and are the primary detection cue for buried landmines[3].

Scattering from clutter objects in the medium causes the Rayleigh wave to become disorganized. If a large number of objects are present, the scattering can interfere with the Rayleigh wave to the point that it no longer effectively illuminates the buried landmine. Any resonance that is excited will be difficult to detect in the presence of the numerous scattered waves reflecting from objects in the medium. By applying time-reversal focusing methods to seismic detection techniques, energy can be focused to a specific location within the medium, irrespective of the presence of clutter or wave

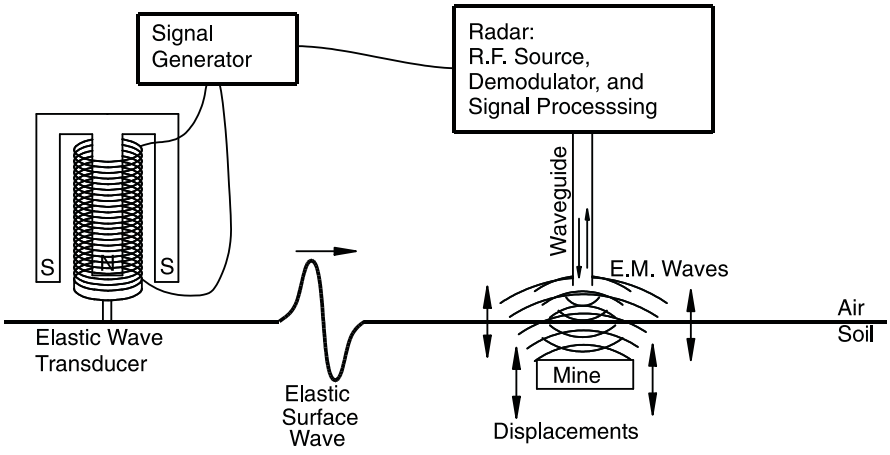

Figure 6: Schematic of the elastic wave landmine detection system using a non-contacting sensor. [3]

velocity gradients. This allows one to focus energy to a certain spot in order to excite a resonance in any target that may be present there.

2.2 Basic Time Reversal Theory

The governing wave equation for elastic waves in solids serves as the starting point for a basic analysis of time-reversal,

$$\rho_s \frac{\partial^2 \vec{u}}{\partial t^2} = (\lambda + 2\mu)\left(\nabla\left(\nabla \cdot \vec{u}\right)\right) - \mu\left(\nabla \times \left(\nabla \times \vec{u}\right)\right) \tag{3}$$

where $\vec{u}$ is displacement, λ and μ are the Lamé constants of the medium and ρ_s is the density. This equation is valid for the case for which there are no external forces (body forces) present on the medium. It also assumes that the medium is lossless with respect to wave propagation. The assumption of a lossless medium is not physical, but if the losses are very small, the additional terms in the equation have a negligible

effect and can be ignored.

As was mentioned in Chapter 1, examination of the wave equation shows that there are only second-order time derivatives present. Because of the lack of odd-order time derivatives, if there is a solution to this equation $\vec{u}(\vec{r}, t)$, then $\vec{u}(\vec{r}, -t)$ must also be a solution to this equation. Because experimentally it is necessary to work with time reversal in a causal fashion, a finite time duration must be selected over which the equation will be considered. The formulation $\vec{u}(\vec{r}, T - t)$ over the interval $(0, T)$ satisfies the causality requirement. If all energy in the spatial region of interest is small outside of this time interval, then this solution should be almost exactly equal to $\vec{u}(\vec{r}, -t)$.

As in the case of a fluid, a time-reversal cavity is constructed around a location of interest, usually a source location. All waves impinging on this surface are recorded, time-reversed, and re-transmitted. Classical time-reversal focusing further simplifies this to a time-reversal mirror (TRM) where only a portion of the time-reversal cavity is realized. The TRM concept is well documented in the literature [4].

In the case of elastic surface waves, the principal wave mode of interest is the Rayleigh wave, a surface wave that decays exponentially with depth. Though some energy is lost from mode conversion and from scattering objects in the soil, most of the Rayleigh wave's energy remains near the surface. Given that landmines are buried near the surface and the energy in the Rayleigh wave is concentrated in that region, the landmine detection problem is approached here as a quasi-2-D problem.

To construct a TRM, receivers are realized as a simple array. The array subtends some angle of the 3-D surface that would be necessary to surround the focus point. This array is much more practical to implement than a time-reversal cavity, but it is subject to the limitations of array techniques. The number and spacing of the array elements will have effects on grating lobes. The spot size of the focus point is also limited by the TRM aperture and diffraction effects proportional to wavelength[5].

Figure 7: Geometry of the implementation of time-reversal focusing.

The TRM concept has been verified in the ultrasound regime for fluid and elastic media[1, 7].

2.3 The Time-Reversal Focusing Method

2.3.1 Implementation

For the experimental implementation of time-reversal focusing, elastic wave sources are located in an array $S_n = (x_{S_n}, y_{S_n} | n = 1, 2, \ldots N)$ (Figure 7). First, consider the effect of time-reversal from a single source, S_n.

Step 1: Transmit an excitation signal, $\epsilon(t)$ from source S_n.

Step 2: Receive a signal, $f_n(t)$, at the desired focusing location, R. Propagation through the medium is described by a Greens function, $G(S_n, R, t)$ such that,

$$f_n(t) = \epsilon(t) * G(S_n, R, t). \tag{4}$$

Step 3: Time-reverse the received signal: $f(t) \Rightarrow f(-t)$.

Step 4: Transmit the time-reversed signal, $f(-t)$, from S_n. Then the recorded signal at any location $\vec{r}$ on the surface will be,

$$U_n(\vec{r}, t) = [\epsilon(-t) * G(S_n, R, -t)] * G(S_n, \vec{r}, t). \tag{5}$$

Recalling the associative property of convolution, $U_n(\vec{r},t)$ then is the cross correlation of the two Greens' functions convolved with the time-reversed excitation function, $\epsilon(-t)$. In the special case when $\vec{r}=R$, this becomes the autocorrelation function. This yields a mathematical explanation for the observed focusing of the signal that occurs at R. This process can be extended to include additional transmitters in the array such that,

$$U(\vec{r},t)=\sum_{n=1}^{N}\left[\epsilon(-t)*G(S_n,R,-t)\right]*G(S_n,\vec{r},t)\,. \tag{6}$$

In the experimental implementation of this method, **Step 1** - **Step 3** are performed once for each transmitter S_n in the array. **Step 4** is performed simultaneously for all transmitters $S_{1\ldots N}$.

Traditional time-reversal focusing using a TRM requires that either a source be located at the desired focus location (R) or that an excitation be launched from the transducer array. In the latter case, after the excitation is launched from the transducer array, reflections off a target at the focal location act as a passive source. These reflections are recorded at the TRM, time-reversed and retransmitted. In the landmine or buried target detection problem, the signal reflected off a target is often not strong enough to be significantly above the noise floor. This makes it impractical to use reflected signals as a source for time-reversal focusing. Further, in the case of landmine detection, it would be unwise to place a seismic source at a location where a landmine is believed to be buried.

While the time-reversal focusing method used in the experiments (Figure 7) is similar to the concept of a TRM, there is noteworthy difference. A TRM relies on reciprocity of the propagation from the source to the focus point, $G_n(R,S_n,t)=G_n(S_n,R,t)$. Applying reciprocity to $U(\vec{r},t)$ will yield the autocorrelation function for the case of $\vec{r}=R$. In the case of an anisotropic propagation medium, reciprocity may not be valid, and the traditional TRM implementation could fail to yield the

autocorrelation function for the special case of $\vec{r} = R$.

2.3.2 Excitation Methods

To investigate the relative effectiveness of time-reversal focusing in elastic media, time-reversal excitation methods will be compared to time-delay focusing methods. Uniform excitation of the transducer array will also be used to serve as a baseline measurement to demonstrate the improvement of each focusing method over a non-focused excitation method.

The results are presented with respect to a differentiated Gaussian pulse excitation (Equations 7, 8), with center frequency, ω_c, and time delay, t_d. When collecting the experimental data, the excitation signal is a chirp, $\epsilon\,(t)$, described by (Equation 9) where A_1, A_2, Pa, P, t_p, f_1, and f_2 are constants which define amplitude, amplitude change rate, frequency change rate, total length of the chirp, and frequency range of the chirp, respectively. For the excitation used in the experiments, those values are: $A_1 = 1$, $A_2 = 0.25$, $Pa = 0.15$, $P = 0.75$, $t_p = 3.596\,s$, $f_1 = 30\,\text{Hz}$, and $f_2 = 2\,\text{kHz}$. The signal is quiescent for 0.5 s for a total duration of 4.096 s. The specific characteristics of the excitation chirp were determined empirically to yield an acceptable signal level, while maintaining an excitation amplitude that is sufficiently linear [3, 16].

In the numerical results, the differentiated Gaussian pulse is used to collect the data. In the experimental results, a chirp signal is used since it is a more effective signal for building up a sufficient signal to noise ratio without exiting large amplitude signals [16]. After collecting the data, $U(\vec{r}, t)$, the chirp signal is removed via deconvolution and the data is convolved with a differentiated Gaussian pulse yielding $D(\vec{r}, t)$. This exchange of the chirp signal for the differentiated Gaussian pulse is best described mathematically in the frequency domain (Equation 10), where $\mathcal{F}$ and $\mathcal{F}^{-1}$ are the standard Fourier and Inverse Fourier transforms respectively [17].

Care should be taken that the frequency range of the Gaussian pulse is chosen to be within the frequency range of the initial chirp signal such that the pulse contains useful information over the entire frequency range of interest.

$$\gamma(t) = (t - t_d)\, e^{\frac{(t-t_d)^2}{\tau_w}} \tag{7}$$

$$\tau_w = \frac{\sqrt{2}}{\omega_c} \tag{8}$$

$$\epsilon(t) = \left\{ A_1 + \left[(A_2 - A_1) \frac{t}{t_p} \right]^{P_a} \right\} \sin\left\{ t(2\pi) \left[f_1 + \left(\frac{f_2 - f_1}{p+1} \right) \left(\frac{t}{t_p} \right)^P \right] \right\} \tag{9}$$

$$D(\vec{r}, t) = \mathcal{F}^{-1} \left\{ \frac{\mathcal{F}\{U(\vec{r}, t)\}}{\mathcal{F}\{\epsilon(t)\}} \mathcal{F}\{\gamma(t)\} \right\} \tag{10}$$

Uniform excitation: All sources are excited with identical differentiated Gaussian pulses. This excitation method is simple to create, and requires no *a priori* knowledge of the physical characteristics of the medium. Without any clutter, pulses leave each source at the same time and form wavefront that travels away from the sources in a uniform manner. In the presence of clutter, the wave front may be scattered, reducing the uniformity of the excitation throughout the medium.

Time-delayed focusing: Here the pulses are time-delayed such that all pulses arrive at a focus location at the same time. Ideally, this method focuses energy to a specific point, creating a larger excitation at the focal point, but this effect is sensitive to variations in wave propagation speed. Calculation of the time-delays for each pulse requires knowledge of the propagation speed throughout the entire medium. When the Rayleigh wave speed is known, along with the distance from source S_n to the target, the time delays can be calculated such that all the pulses arrive at the same time.

Time-reversal focusing: Separate measurements are performed in which a pulse

is propagated from one of the sources, recorded at the focal point and then time-reversed ($t \Rightarrow -t$). The time-reversed signals are then transmitted from their corresponding source locations (Figure 7). Unlike time-delayed focusing, time-reversal requires no knowledge of the propagation speed in the medium.

2.4 The Numerical Model

A numerical model is constructed and used to compare time-reversal to other methods of excitation [18]. The numerical technique used to create the model is the three-dimensional finite-difference time-domain (FDTD) method. A first-order particle-velocity and mechanical-stress formation for the elastic wave fields is developed and then discretized from its continuous differential form. The solution space is then divided into a grid composed of individual cubes known as unit cells (Figure 8a). Each of the elastic wave stresses and velocities are located at discrete spatial points in the three dimensional grid. Using the finite differences between field quantities in adjacent unit cells, the field quantities are computed at each discrete time step. The solution space is surrounded on all four sides and the bottom by a perfectly matched layer (PML) that absorbs all outgoing waves (Figure 8b). This prevents reflections from the edges of the grid, which makes the solution space appear as an infinite half-space. The top surface of the grid is terminated using a free surface boundary condition, which approximates an air-soil interface. A detailed description of the basic model can be found in [15]. Beyond the basic model described in [15], a method of computationally calculating the power flowing through any surface (Poynting vector) within the simulation has been added to the model and is described in this section.

Numerous authors have previously addressed the analytical computation of the wave fields [19, 20, 9, 21, 22], and the power contained in each of the elastic wave modes as they propagate through a medium [23]. These treatments each assume a simple uniform propagation medium that is free from inhomogeneity or scattering

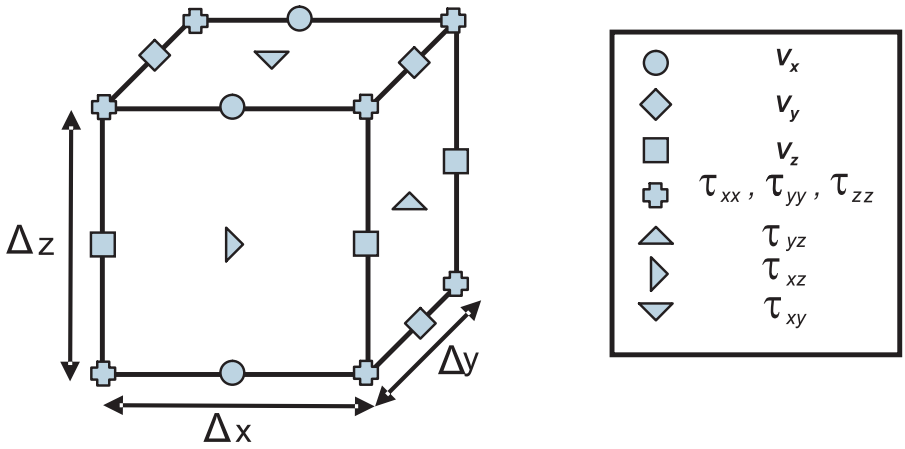

(a) The unit cell for the FDTD model.

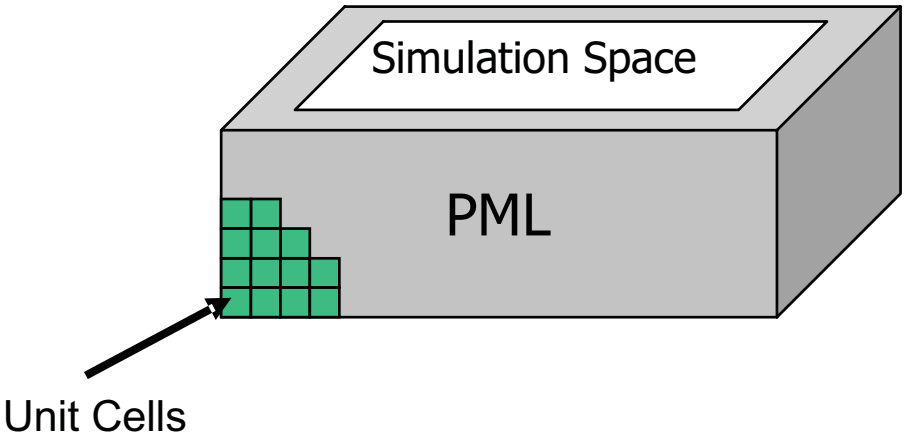

(b) The solution space for the FDTD simulation: composed of unit cells. The center is the area of the simulation while the edges are terminated by a perfectly matched layer (PML).

Figure 8: Finite-difference time-domain model construction

objects. For scattering objects and layering profiles with irregular geometries, an analytical solution becomes intractable. The power of the FDTD algorithm lies in its ability to model the elaborate elastic wave fields that may exist in such a complicated medium. The addition of the Poynting vector calculator to such a broadly applicable algorithm allows for a more detailed exploration of the effects of inhomogeneity in the propagation medium.

2.4.1 Essential Elements of the Three-Dimensional Numerical Model

To create the numerical model using FDTD, a first-order particle-velocity and mechanical - stress formation for the elastic wave fields is developed and then discretized from its continuous differential form. The first -order system of equations contains nine linearly independent equations that completely describe the three velocity components, v_x,v_y,v_z,and the six stress tensor components τ_{xx},τ_{yy},τ_{zz},τ_{yz},τ_{xz},τ_{xy},. The nine equations are

$$\rho\frac{\partial v_x}{\partial t} = \frac{\partial \tau_{xx}}{\partial x} + \frac{\partial \tau_{xy}}{\partial y} + \frac{\partial \tau_{xz}}{\partial z} \tag{11}$$

$$\rho\frac{\partial v_y}{\partial t} = \frac{\partial \tau_{xy}}{\partial x} + \frac{\partial \tau_{yy}}{\partial y} + \frac{\partial \tau_{yz}}{\partial z} \tag{12}$$

$$\rho\frac{\partial v_z}{\partial t} = \frac{\partial \tau_{xz}}{\partial x} + \frac{\partial \tau_{yz}}{\partial y} + \frac{\partial \tau_{zz}}{\partial z} \tag{13}$$

$$\frac{\partial \tau_{xx}}{\partial t} = (\lambda + 2\mu)\frac{\partial v_x}{\partial x} + \lambda\frac{\partial v_y}{\partial y} + \lambda\frac{\partial v_z}{\partial z} \tag{14}$$

$$\frac{\partial \tau_{yy}}{\partial t} = \lambda\frac{\partial v_x}{\partial x} + (\lambda + 2\mu)\frac{\partial v_y}{\partial y} + \lambda\frac{\partial v_z}{\partial z} \tag{15}$$

$$\frac{\partial \tau_{zz}}{\partial t} = \lambda\frac{\partial v_x}{\partial x} + \lambda\frac{\partial v_y}{\partial y} + (\lambda + 2\mu)\frac{\partial v_z}{\partial z} \tag{16}$$

$$\frac{\partial \tau_{yz}}{\partial t} = \mu\left(\frac{\partial v_y}{\partial z} + \frac{\partial v_z}{\partial y}\right) \tag{17}$$

$$\frac{\partial \tau_{xz}}{\partial t} = \mu\left(\frac{\partial v_x}{\partial z} + \frac{\partial v_z}{\partial x}\right) \tag{18}$$

$$\frac{\partial \tau_{xy}}{\partial t} = \mu\left(\frac{\partial v_x}{\partial y} + \frac{\partial v_y}{\partial x}\right) \tag{19}$$

where μ and λ are the Lamé constants and ρ is the density. Together these three quantities describe the material's physical properties.

The continuous equations can be converted to a discrete form that closely approximates the continuous equations. The solution space is divided into a grid composed of individual cubes known as unit cells (Figure 8a). Each of the elastic wave stresses and velocities are located at discrete spatial points in the three dimensional grid. Using the finite differences between field quantities in adjacent unit cells, Equations 11 - 19 are re-arranged and discretized. These equations are used to compute the field quantities at discrete spatial and time steps. The discretized equations all follow a similar form. For the sake of brevity, only the discretized form of Equations 11 and (14 are presented below,

$$\rho\frac{V_x^{l+0.5}|_{i,j,k}-V_x^{l-0.5}|_{i,j,k}}{\Delta t} = \frac{T_{xx}^{l}|_{i,j,k}-T_{xx}^{l}|_{i-1,j,k}}{\Delta x}+ \frac{T_{xy}^{l}|_{i,j,k}-T_{xy}^{l}|_{i,j-1,k}}{\Delta y} + \frac{T_{xz}^{l}|_{i,j,k}-T_{xz}^{l}|_{i,j,k-1}}{\Delta z} \tag{20}$$

$$\frac{T_{xx}^{l+1}|_{i,j,k}-T_{xx}^{l}|_{i,j,k}}{\Delta t} = (\lambda+2\mu)\frac{V_x^{l+0.5}|_{i+1,j,k}-V_x^{l+0.5}|_{i,j,k}}{\Delta x}+ \lambda\frac{V_y^{l+0.5}|_{i,j,k}-V_y^{l+0.5}|_{i,j-1,k}}{\Delta y} + \lambda\frac{V_z^{l+0.5}|_{i,j,k}-V_z^{l+0.5}|_{i,j,k-1}}{\Delta z} \tag{21}$$

In the equations above, V and T are the velocity and stress field values analogous to v and τ in the continuous equations. These values are evaluated at discrete points in space and time. The time values are noted by l and the spatial location by the coordinates i, j, and k. While the i,j, k indices define the FDTD cell of any field value, the field components are offset in space within the FDTD grid. Table 1 shows the physical location of each field component within the FDTD grid.

Once the field values for $V_x^{l-0.5}$, T_{xx}^{l}, T_{xy}^{l}, T_{xz}^{l} are known at all the spatial locations in the grid, Equation 20 can be re-arranged to yield $V_x^{l-0.5}$,

	Coordinate			
Component	x	y	z	t
V_x	$i\Delta x$	$(j-0.5)\Delta y$	$(k-0.5)\Delta z$	$(l+0.5)\Delta t$
V_y	$(i+0.5)\Delta x$	$j\Delta y$	$(k-0.5)\Delta z$	$(l+0.5)\Delta t$
V_z	$(i+0.5)\Delta x$	$(j-0.5)\Delta y$	$k\Delta z$	$(l+0.5)\Delta t$
T_{xx}	$(i+0.5)\Delta x$	$(j-0.5)\Delta y$	$(k-0.5)\Delta z$	$l\Delta t$
T_{yy}	$(i+0.5)\Delta x$	$(j-0.5)\Delta y$	$(k-0.5)\Delta z$	$l\Delta t$
T_{zz}	$(i+0.5)\Delta x$	$(j-0.5)\Delta y$	$(k-0.5)\Delta z$	$l\Delta t$
T_{yz}	$(i+0.5)\Delta x$	$j\Delta y$	$k\Delta z$	$l\Delta t$
T_{xz}	$i\Delta x$	$(j-0.5)\Delta y$	$k\Delta z$	$l\Delta t$
T_{xy}	$i\Delta x$	$j\Delta y$	$(k-0.5)\Delta z$	$l\Delta t$

Table 1: Field component positions of the (i, j, k) cell in the FDTD grid at timestep l.

$$V_x^{l+0.5}|_{i,j,k} = V_x^{l-0.5}|_{i,j,k} + \frac{\Delta t}{\rho}\left[\frac{T_{xx}^l|_{i,j,k} - T_{xx}^l|_{i-1,j,k}}{\Delta x} + \frac{T_{xy}^l|_{i,j,k} - T_{xy}^l|_{i,j-1,k}}{\Delta y} + \frac{T_{xz}^l|_{i,j,k} - T_{xz}^l|_{i,j,k-1}}{\Delta z}\right]. \tag{22}$$

In a similar manner, Equation 21 is re-arranged to yield T_{xx}^{l+1},

$$T_{xx}^{l+1}|_{i,j,k} = T_{xx}^l|_{i,j,k} + \Delta t\left[(\lambda + 2\mu)\frac{V_x^{l+0.5}|_{i+1,j,k} - V_x^{l+0.5}|_{i,j,k}}{\Delta x} + \lambda\frac{V_y^{l+0.5}|_{i,j,k} - V_y^{l+0.5}|_{i,j-1,k}}{\Delta y} + \lambda\frac{V_z^{l+0.5}|_{i,j,k} - V_z^{l+0.5}|_{i,j,k-1}}{\Delta z}\right]. \tag{23}$$

Following the form described above, the remaining continuous equations are discretized and re-arranged such that each of the field components are known at discrete spatial and temporal locations within the FDTD grid.

The edges of the computational space are terminated on four sides and the bottom by a perfectly matched layer (PML) that absorbs all outgoing waves (Figure 8b). This prevents reflections from the edges of the grid, which makes the solution space appear as an infinite half-space. The top surface of the grid is terminated using a free surface boundary condition, which approximates an air-soil interface.

2.4.2 Computational Method for Calculating the Poynting Vector of Elastic Waves in FDTD

The definition for the acoustic Poynting vector, describing power density in watts/m^2) is given by [24],

$$P = -\mathbf{V}\cdot\mathbf{T} = \hat{x}\left(-V_xT_{xx} - V_yT_{yx} - V_zT_{zx}\right) + \hat{y}\left(-V_xT_{xy} - V_yT_{yy} - V_zT_{zy}\right) + \hat{z}\left(-V_xT_{xz} - V_yT_{yz} - V_zT_{zz}\right) + \tag{24}$$

where V_n is velocity in the $\hat{n}$ direction, and T_{ij} uses the customary notation to denote the stress along the i plane, in the j direction.

An examination of the FDTD model (Figure 8) reveals that all the field quantities required in order to compute the Poynting vector are known.[1] Due to the staggered spatial grid and the temporal leap-frog scheme of the FDTD algorithm, field values are located at different points in time and space. Figure 8a shows the spatial layout of the field components. Due to the temporal staggering in the FDTD algorithm, the stress and velocity components are also offset in time[15]. In order to compute the Poynting vector for a particular cell in the FDTD grid, the components must be spatially and temporally averaged to co-locate the field values.

The spatial averaging is addressed first. Examining the FDTD grid and its orientation with respect to the free surface boundary, the location of the components T_{xx}, T_{yy}, and T_{zz} appears to be the best spatial location to co-locate all the field values. Examining the location of these components in Figure 1, the spatial location at which all field quantities should be located is $[(i+0.5)\Delta x, (j-0.5)\Delta y, (k-0.5)\Delta z, (l+0.5)\Delta t]$. Known field values can be averaged in order to determine the field values at the same location in time and space. Table 2 shows how the field values are averaged to spatially co-locate the field values.

After completing the spatial averaging, temporal averaging must be accounted for. As noted in the description of the FDTD model[15], the T and V components are not only offset in space, but also in time due to temporal staggering of the FDTD update equations. The values of T are known at integer timesteps, l, but V values are known one-half timestep apart, at timesteps $l+0.5$, i.e., $T^{l\Delta t}$ and $V^{(l+0.5)\Delta t}$ are known where l is any timestep. In order to compute $\mathbf{P}$, all values of T and V must be evaluated at the same points in time. Since the computation for each component of the Poynting vector is similar, temporal averaging will be demonstrated only for $\mathbf{P} \cdot \hat{\mathbf{x}}$,

[1] For isotropic materials, $T_{ij} = T_{ji}$

Component	**Average Field Value**
V_x	$\frac{V_x(i,j,k)+V_x(i+1,j,k)}{2}$
V_y	$\frac{V_y(i,j,k)+V_y(i,j,k-1)}{2}$
V_z	$\frac{V_z(i,j,k)+V_z(i,j-1,k)}{2}$
T_{xx}	$T_{xx}(i,j,k)$
T_{yy}	$T_{yy}(i,j,k)$
T_{zz}	$T_{zz}(i,j,k)$
T_{yz}	$\frac{(T_{yz}(i,j,k)+T_{yz}(i,j-1,k-1))}{2}$
T_{xz}	$\frac{(T_{xz}(i,j,k)+T_{yz}(i+1,j-1,k))}{2}$
T_{xy}	$\frac{(T_{xy}(i,j,k)+T_{xy}(i+1,j,k-1))}{2}$

Table 2: Field components averaged to co-locate all field values at $[(i+0.5)\Delta x, (j-0.5)\Delta y, (k-0.5)\Delta z, (l+0.5)\Delta t]$ in the FDTD grid.

$$P \cdot \hat{x} = -\hat{x} \left(V_x T_{xx} + V_y T_{yx} + V_z T_{zx} \right). \tag{25}$$

The time $t = (l + 0.5)\Delta t$ is taken as the time at which all the field quantities will be evaluated to compute $\mathbf{P} \cdot \hat{\mathbf{x}}$. From the FDTD update equations (Equations 22 - 23), $V_x^{l+0.5}$, $V_y^{l+0.5}$, $V_z^{l+0.5}$, T_{xx}^{l}, T_{yx}^{l}, T_{z}^{l}, T_{xx}^{l+1}, T_{yx}^{l+1}, T_{z}^{l+1} are known. The stresses at the desired time, $t = (l + 0.5)\Delta t$ can be computed by simple time averaging,

$$T_{xx}^{l+0.5} = \frac{T_{xx}^{l} + T_{xx}^{l+1}}{2} \tag{26}$$

$$T_{yx}^{l+0.5} = \frac{T_{yx}^{l} + T_{yx}^{l+1}}{2} \tag{27}$$

$$T_{zx}^{l+0.5} = \frac{T_{zx}^{l} + T_{zx}^{l+1}}{2}. \tag{28}$$

The other stress components, $T_{yy}^{l+0.5}$, $T_{zz}^{l+0.5}$, $T_{yz}^{l+0.5}$, can be found in a similar manner.

Because of the intensive memory requirements to store all field values throughout the entire grid, the stresses, T_{nn} are not simultaneously stored at $t = (l)\Delta t$, and $t = (l + 1)\Delta t$. In order to compute the Poynting vector, $\mathbf{P}$ is computed twice. $\mathbf{P_1}$ is evaluated before the new stresses are computed when the stresses are known at $t = (l)\Delta t$. The stresses at $t = (l + 1)\Delta t$ are computed, using the velocities known at $t = (l + 0.5)\Delta t$. Then, $\mathbf{P_2}$ is computed using these new stresses at $t = (l + 1)\Delta t$. The flow diagram in Figure 9 illustrates the procedure.

Now that the temporal and spatial averaging procedures have been developed, the update equations for P_{1x} and P_{2x} are presented. These equations are valid for all locations that are not near the edges of the FDTD grid.

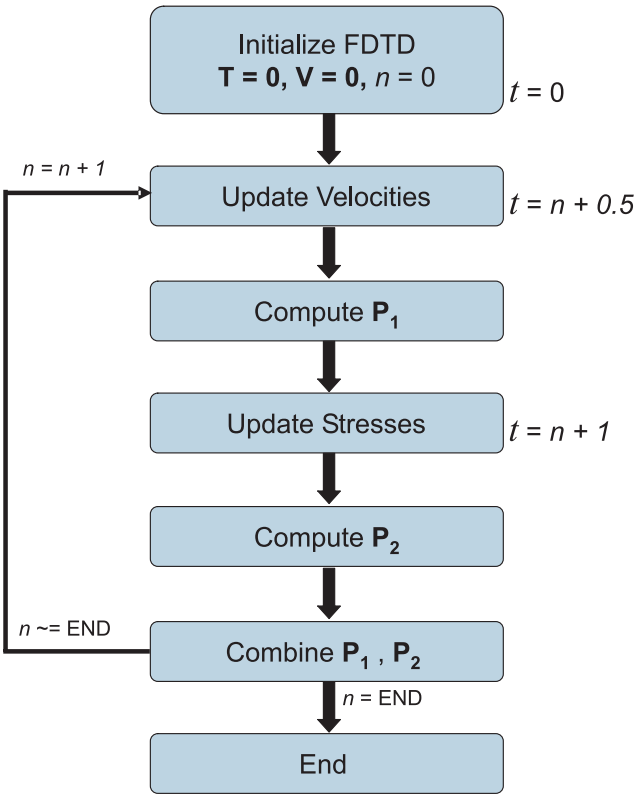

Figure 9: A flow diagram illustrating the implementation of the Poynting vector algorithm in FDTD.

$$
\begin{aligned}
P_{1x} = \; & -\hat{x}\Bigg(\left[\frac{\left(V_x^{l+0.5}(i,j,k)+V_x^{l+0.5}(i+1,j,k)\right)}{2} \right] T_{xx}^{l}(i,j,k) \\
& + \left[\frac{\left(V_y^{l+0.5}(i,j,k)+V_y^{l+0.5}(i,j,k-1)\right)}{2} \right] \left[\frac{T_{yx}^{l}(i,j,k)+T_{yx}^{l}(i+1,j,k-1)}{2} \right] \\
& + \left[\frac{\left(V_z^{l+0.5}(i,j,k)+V_y^{l+0.5}(i,j-1,k)\right)}{2} \right] \left[\frac{T_{zx}^{l}(i,j,k)+T_{zx}^{l}(i+1,j-1,k)}{2} \right] \Bigg)
\end{aligned}
\tag{29}
$$

$$
\begin{aligned}
P_{2x} = \; & -\hat{x}\Bigg(\left[\frac{\left(V_x^{l+0.5}(i,j,k)+V_x^{l+0.5}(i+1,j,k)\right)}{2} \right] T_{xx}^{l+1}(i,j,k) \\
& + \left[\frac{\left(V_y^{l+0.5}(i,j,k)+V_y^{l+0.5}(i,j,k-1)\right)}{2} \right] \left[\frac{T_{yx}^{l+1}(i,j,k)+T_{yx}^{l+1}(i+1,j,k-1)}{2} \right] \\
& + \left[\frac{\left(V_z^{l+0.5}(i,j,k)+V_y^{l+0.5}(i,j-1,k)\right)}{2} \right] \left[\frac{T_{zx}^{l+1}(i,j,k)+T_{zx}^{l+1}(i+1,j-1,k)}{2} \right] \Bigg)
\end{aligned} \tag{30}
$$

$$
P \cdot \hat{x} = \frac{P_{1x} + P_{2x}}{2} \tag{31}
$$

Similarly,

$$
\begin{aligned}
P_{1y} = \; & -\hat{y}\Bigg(\left[\frac{\left(V_x^{l+0.5}(i,j,k)+V_x^{l+0.5}(i+1,j,k)\right)}{2} \right] \left[\frac{T_{xy}^{l}(i,j,k)+T_{xy}^{t}(i+1,j,k-1)}{2} \right] \\
& + \left[\frac{\left(V_y^{l+0.5}(i,j,k)+V_y^{l+0.5}(i,j,k-1)\right)}{2} \right] T_{yy}^{t}(i,j,k) \\
& + \left[\frac{\left(V_z^{l+0.5}(i,j,k)+V_y^{l+0.5}(i,j-1,k)\right)}{2} \right] \left[\frac{T_{zy}^{l}(i,j,k)+T_{zy}^{l}(i,j-1,k-1)}{2} \right] \Bigg)
\end{aligned} \tag{32}
$$

$$P_{1z} = -\hat{z}\Bigg(\left[\frac{\left(V_x^{l+0.5}(i,j,k)+V_x^{l+0.5}(i+1,j,k)\right)}{2} \right] \left[\frac{T_{xz}^{l}(i,j,k)+T_{xz}^{l}(i+1,j-1,k)}{2} \right]$$

$$+ \left[\frac{\left(V_y^{l+0.5}(i,j,k)+V_y^{l+0.5}(i,j,k-1)\right)}{2} \right] \left[\frac{T_{yz}^{l}(i,j,k)+T_{yz}^{l}(i,j-1,k-1)}{2} \right] \tag{33}$$

$$+ \left[\frac{\left(V_z^{l+0.5}(i,j,k)+V_y^{l+0.5}(i,j-1,k)\right)}{2} \right] T_{zz}^{l}(i,j,k) \Bigg)$$

P_{2y}, P_{2z}, and $P \cdot \hat{y}$, $P \cdot \hat{z}$ are computed in the same manner as P_{2x} and $P \cdot \hat{x}$.

2.4.3 Boundaries

The update equations developed for $P \cdot \hat{x}$, $P \cdot \hat{y}$, $P \cdot \hat{z}$ are easily computed away from the edges of the grid where spatial averaging is simple to compute. The edges of the grid, however, require special treatment because spatial averaging is not possible when there are no physical field values stored beyond the edge of the FDTD grid.

Treatment of the edges that terminate in the PML is simple. The PML is a layer of FDTD cells that attenuate waves as they propagate through it. For this reason, calculation of the power passing through a surface inside the PML would reveal little about the physical characteristics of the medium. Any surface on which the Poynting vector is calculated should be sufficiently far from the PML to avoid spatial averaging that includes the PML cells.

Waves bound to the surface, and therefore propagating immediately adjacent to the free surface boundary are of primary interest in many investigations of elastic wave behavior. Special treatment of the free surface boundary is required in the FDTD algorithm [15]. Due to the spatial averaging that is required for computation of the Poynting vector, the special updates for the V_n and T_{nn} values are not sufficient

to compute the Poynting vector. Additional special updates are required to calculate the Poynting vector adjacent to the free surface. By the definition of a free surface, no energy will propagate through the surface, so $P \cdot \hat{z}$ will be zero on the surface. Therefore, the special updates only need to be computed for $P \cdot \hat{x}$ and $P \cdot \hat{y}$.

Because of the location of the free surface boundary with respect to V_z, spatial averaging is not possible. Normally, V_z would be computed as,

$$V_z[(i+0.5)\Delta x, (j-0.5)\Delta y, (k-0.5)\Delta z] = \frac{V_z(i,j,k) + V_z(i,j-1,k)}{2}. \tag{34}$$

By definition of the free surface boundary,

$$T_{xz}(x, y, z = 0) = 0 \tag{35}$$

$$T_{yz}(x, y, z = 0) = 0 \tag{36}$$

$$T_{zz}(x, y, z = 0) = 0. \tag{37}$$

Note from Equation 29 that when $V_z|_{z=0}$ it is multiplied by $T_{xz}|_{z=0}$, which by definition must equal zero on a free surface. So, the entire term in Equation 29 need not be computed on the free surface boundary. Similarly, from Equation 30, $V_z|_{z=0}$ is multiplied by $T_{yz}|_{z=0} = 0$.

2.5 Validation of Numerical Results

In order to verify the functionality of the Poynting vector calculator, a simple problem was modelled, in which the analytical solution may be calculated. The analytical solution used for comparison is that of the power radiated from a circular disk source that excites only the normal stress, τ_{zz}. The numerical solution is computed in the frequency domain for a disk that is small compared to a wavelength.

The analytical solution is obtained by using a Fourier transform method to generate an integral equation. This equation is solved using numerical integration [25, 23]. Analytical results for a specific set of material parameters are available [23] and will serve as a basis for comparison to the numerical results.

For verification, the set of material parameters, $\sigma = \frac{1}{4}$ and $\mu_m = \sqrt{3}$ are used where σ is Poisson's ratio, and $\mu_m = \sqrt{c_{11}/c_{44}}$ where c_{11} and c_{44} are the compressional and shear elastic constants of the medium. These parameters, are combined with a chosen density, $\rho = 1400\,\mathrm{kg/m^3}$ and a shear wave speed, $C_s = 87\,\mathrm{m/s}$ to completely describe the necessary material properties of the propagation medium.

In order to compare the frequency domain analytical solution to the time-domain results generated using the FDTD algorithm, a single frequency ($f = 450$ Hz) sine wave is used as the FDTD excitation signal. The signal must be quiescent at the beginning of the numerical simulations, and ramped up to its final amplitude during the simulation to avoid non-physical changes in the field values. Once the source reaches its final amplitude, the field values may be time averaged over an integer number of wave periods to obtain a time-averaged power for comparison to the frequency domain results.

2.5.1 Total Power: Analytical Comparison

The first comparison of the numerical and analytical results is generated by computing the total power radiated by the source. Since the analytical solution is only valid while the source is small compared to a wavelength, the analytical and numerical solutions should diverge as the size of the source increases. Figure 10 shows that the numerical and analytical solutions are comparable for a small source, but as the source increases in size the results diverge as expected.

Inspection of the ratio of the FDTD-to-Analytic power results reveals that the ratio is not constant with respect to the source size even for a source that is small compared to a wavelength. There are several reasons that this may be the case. The first is the effect of the FDTD staircase meshing [26, 27]. The analytical result uses a disk as the source. In order to model such a source in the cartesian coordinate system chosen for this implementation of the FDTD algorithm, a disk must be approximated

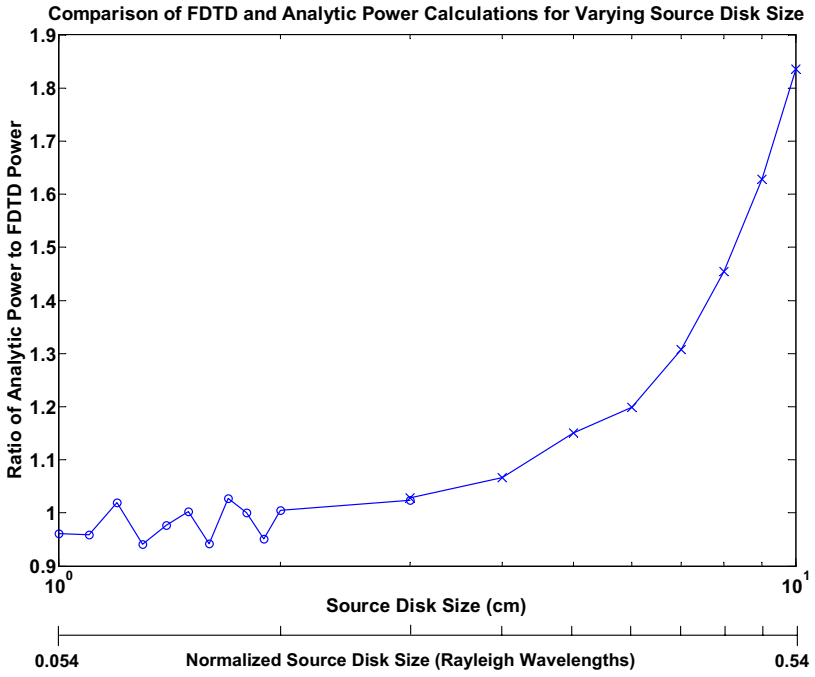

Figure 10: Comparison of FDTD and Analytic Power calculations for varying source disk size. The disk size is noted both in absolute size (cm) and relative size with respect to the Rayleigh wavelength (λ_R) in the propagation medium at 450 Hz.

by some number of cubic cells. This means that the "disk" in FDTD will be neither perfectly round, nor infinitesimally thin.

A second cause of the error is the spatial staggering of field components within the FDTD grid. For the analytical solution, the edge of the disk source is perfectly abrupt, such that the transition of the amplitude of the stress field from the source to the medium is spatially instantaneous. In the case of the FDTD source, the stress source transitions from an amplitude at A to zero over the width of a cell. The effects of both of these errors diminish as the cell size decreases with respect to a wavelength.

2.5.2 Total Power: Poynting Surface Size

The total power exiting the closed surface is good verification of the power calculator's accuracy. If a closed surface is chosen around a source, the energy propagating

through this surface should be the same regardless of the size of the physical size of the closed surface. This fact provides an additional method for verifying the accuracy of the Poynting Vector calculation.

An numerical simulation is performed that uses a 1 cm disk source on the surface and encloses it with a cube on five sides. The sixth side of the cube is the free-space surface. Since elastic waves do not propagate in a vacuum, it is not necessary to calculate outgoing power on this surface since it will always be zero.

The disk is excited with a differentiated Gaussian pulse, and the power exiting the box is computed. The experiment is repeated multiple times, with varying parameters for the Poynting surface box that encloses the source. Table 3 shows the results. The change in the recorded power from an extremely small box to much larger ones is negligible. It is worth noting that extremely small Poynting surfaces very close to the source will be less accurate at computing the power exiting the surface. The reason for this is the evanescent modes that are present very close to the edges of the source. These evanescent field values vary rapidly across the grid, and these rapid spatial changes in evanescent field amplitude may not be captured given the spatial size of the FDTD grid. However, since evanescent waves do not propagate, and their amplitudes fall off exponentially, the solution quickly converges as the box becomes larger.

Surface Dimension X (cm)	**Surface Dimension Y (cm)**	**Surface Dimension Z (cm)**	**Normalized Power**
6	6	6	1.0291
13	13	15	1.0145
13	13	29	1.0109
30	30	30	1.0036
50	50	45	1.0000
70	70	45	1.0036

Table 3: A comparison of the normalized total power exiting an enclosed surface for different size surfaces. The power is computed using the power calculator developed in this chapter.

CHAPTER III

TIME REVERSAL FOCUSING IN CLUTTERED SAND

3.1 Introduction

Section 2.1 described the landmine detection problem, and the system under development at the Georgia Institute of Technology. The detection system functions by exciting elastic waves that propagate through the soil. Several wave types are generated by the seismic source, but the most important one for detection of landmines is the Rayleigh surface wave that propagates along the air-soil interface of the ground. When the Rayleigh wave passes through an object buried in the sand, it excites that object into vibration. Objects such as rocks and sticks scatter wave fronts, but usually vibrate very little themselves. Landmines, due to their regular structure, exhibit a resonant vibration between the flexible top of the landmine and the soil layer above the mine. The resonating landmine excites surface displacements of the ground which are then measured using the non-contacting electromagnetic sensors.

The effectiveness of the detection system depends on relatively large displacements of the ground at the location of a landmine in order to excite this flexural resonance. In a highly cluttered medium, most of the energy in the transmitted wave is scattered from objects in the medium. The result is that very little coherent energy reaches the target, and any small resonance that is excited is difficult to detect due to the numerous waves continuously bouncing off the scattering objects in the medium. In application to a landmine detection system, time-reversal focusing may be used as an interrogation tool to deliver energy to some location that was ineffectively interrogated using other excitation methods.

Time-reversal focusing methods allow for energy to be focused at any location in a

highly cluttered medium, without any knowledge of the characteristics of the medium. Time-reversal focusing may also be more than a focusing method that is impervious to the adverse impact of clutter. Some investigations of time-reversal focusing have noted improvements in focusing resolution due to the presence of clutter [2, 11, 12] (Section 1.1).

This chapter will examine the effectiveness of time-reversal focusing using both the numerical model and the experimental system described in Sections 2.1 and 2.4. The numerical models will provide an initial investigation into time-reversal phenomena in a noise free, and perfectly linear, environment. Once time-reversal focusing has been examined in the numerical models, experiments will be performed to assess its actual effectiveness in an experimental context.

3.2 Numerical Time-Reversal Focusing

3.2.1 The Numerical Model

A numerical model is constructed and used to compare time-reversal to other methods of excitation [18]. This model is created using the FDTD numerical method described in Section 2.4. Time reversal is compared to uniform excitation and time-delay focusing methods. The numerical simulations show that time-reverse focusing gives improved results in the presence of clutter over other excitation methods.

Several parameters were used to define the solution space for the model. The physical size of the space is 210 cm $\times$ 210 cm $\times$ 50 cm. This space is discretized into equally sized unit cells of 0.5 cm on a side for a total computational model size of 420 $\times$ 420 $\times$ 100 cells. The solution space is surrounded on four sides and the bottom with a ten-cell thick perfectly matched layer (PML) to absorb all outgoing waves. The surface is terminated in a free surface boundary to simulate the air-soil interface. The time step (Δt) between successive calculations is set to 0.75 μs and the simulation is run for approximately 40 ms for a total of 52,981 time steps. The

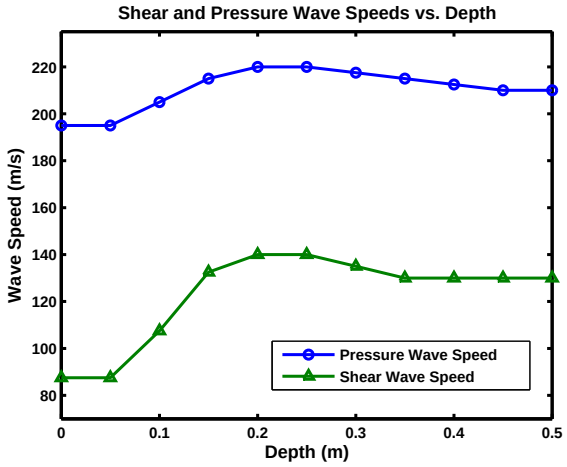

Figure 11: The shear and pressure wave profiles used in the numerical simulations. The profiles are based off measured characteristics of the sand in the experimental facility.

computation of results is performed on 33 nodes in a Beowulf Cluster. Each node is powered by an Athlon64 Dual Core 4200+ processor, and requires approximately 6 hours for computation of the results for each simulation.

Soil is generally a layered medium with each layer having its own set of physical characteristics. To accurately simulate a physical situation and to encourage better agreement between numerical and experimental results, a soil profile is selected that approximates the measured characteristics of damp compacted sand [15]. The profile in Figure 11 matches the characteristics measured in the experimental facility at the Georgia Institute of Technology that is used for the experimental measurements.

Spheres are used as scattering objects in the numerical simulations to break up the wave fronts. Though they are uniform in shape, spheres are sufficient to break up wave fronts if the medium is sufficiently filled, and the spheres are appropriately sized such that their diameters are some significant fraction of a wavelength within the frequency range of interest. The spheres are modelled with material parameters similar to those of many types of stone or other dense scattering media commonly found in soil: $V_{pressure} = 3824\,\mathrm{m/s}$, $V_{shear} = 2342\,\mathrm{m/s}$, $Density(\rho) = 2280\,\mathrm{kg/m^3}$. A

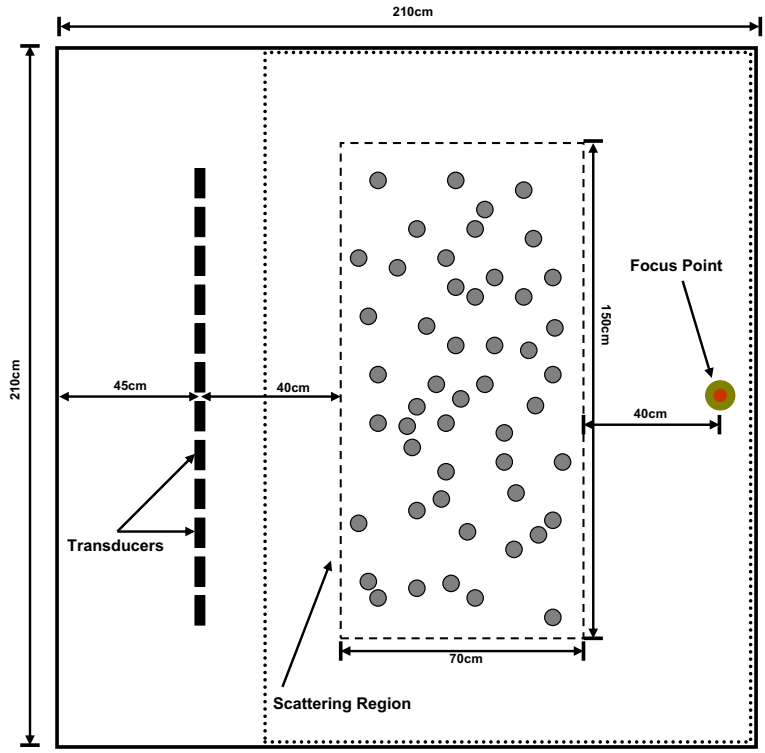

Figure 12: The numerical model setup. The spheres are randomly distributed in the numerical simulation as scattering objects.

random distribution of 5 cm diameter spheres is created (Figure 12). All spheres are placed with their tops at the surface of the medium. Since the Rayleigh wave used in the landmine detection system is a surface wave, deeply buried scattering objects would have negligible effects on displacements measured at the surface.

The simple case of time reversal, as described in Section 2.3, is used in the numerical model. Twelve receivers are arranged in a line and are spaced 15 cm apart. A point source is placed at the desired focal location. In the reverse problem, the array of receivers is replaced with an array of independently controlled sources.

3.2.2 Numerical Results

When producing elastic waves in the soil, there are several different ways to excite the array of transducers. This section presents the results of three array excitation methods that will be compared. The primary advantages and disadvantages of each method will also be noted. The results will be presented as pseudo color graphs of the magnitude of the vertical component of the particle velocity at the surface. The pseudo color scale is a 40-dB logarithmic scale from white (0 dB) to black (−40 dB).

3.2.2.1 Uniform Excitation

Uniform excitation drives all sources in the array using identical excitation signals. In the numerical case presented here, all sources are excited with identical differentiated Gaussian pulses. Without scatterers present, a nearly uniform wave front propagates across the surface of the medium. Figure 13 shows two snapshots in time of a uniform excitation wavefront propagating through the elastic medium. The images in Figure 13 depict the wave amplitudes on the surface. Both images are of the same physical area, at different points in time.

The uniform excitation method is simple to create, and requires no a priori knowledge of the physical characteristics of the medium. It also excites each location along the wave front uniformly as long as no scattering objects are present. In the presence of clutter, the wave front may be scattered, reducing the uniformity of the excitation.

When all the sources are excited uniformly, the wave front interacts with the various scattering objects (Figure 12) present in the medium and the result is shown in Figure 14. As the wave propagates through the scattering objects, it is broken up such that no coherent wave arrives at the target location. This case demonstrates that in the presence of high clutter, uniform excitation of the sources provides low signal levels to the target location which will only weakly excite a landmine at such a location. Uniform excitation works well if little clutter is present, providing a uniform

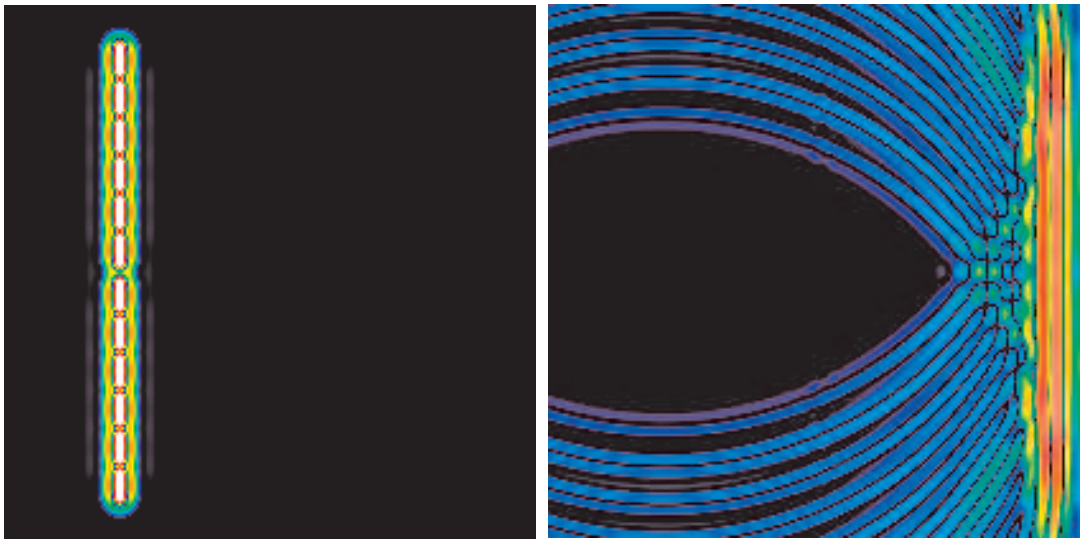

(a) Uniform waves are launched from the 12 sources.

(b) The wave front created by the uniform excitation propagates along the surface.

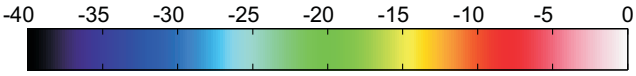

(c) Color - Amplitude Scale

Figure 13: Uniform excitation with no scattering: two snapshots in time.

wave front that excites equal signal levels throughout most of the solution space.

3.2.2.2 Time-Delay Focusing Excitation

The second excitation type uses differentiated Gaussian pulses that are time-delayed such that all pulses arrive at a focus location at the same time. Since the propagation paths from the sources to the focal point differ in length, the pulses can be time delayed such that all the pulses arrive at the focal point at the same time. Figure 15 shows two snapshots in time of a time-delayed excitation wavefront propagating through the elastic medium and focusing at a point in the central region of the medium. While this is a method of effectively focusing energy to a desired point, the calculation of the time-delays for each pulse requires the knowledge of the propagation speed throughout the entire medium.

If low-level clutter or variations in wave speeds are present, time-delay focusing is

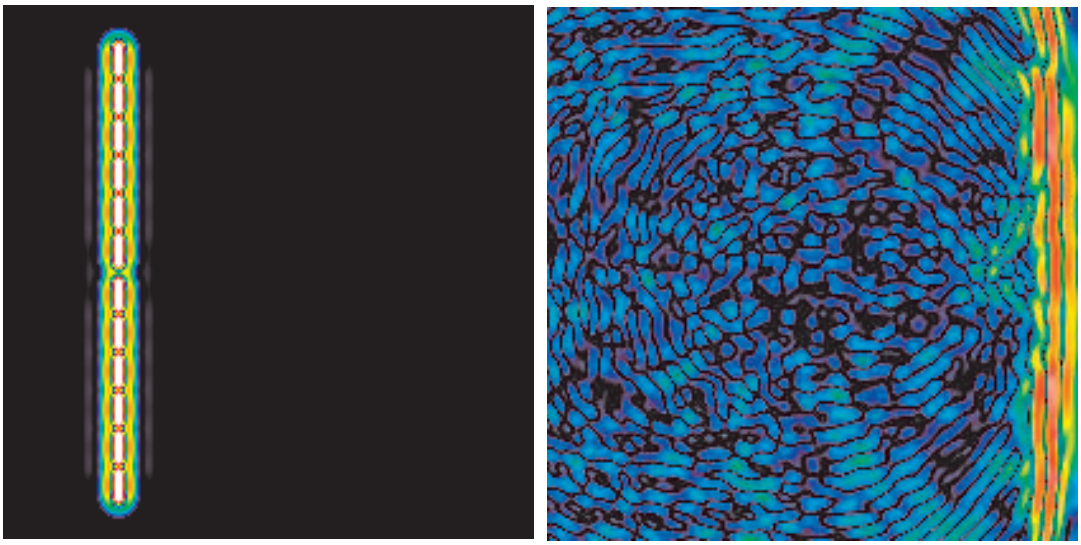

(a) Identical waves are launched from the 12 sources.

(b) The wave front is altered upon arrival at the desired focal point due to scattering objects in the medium.

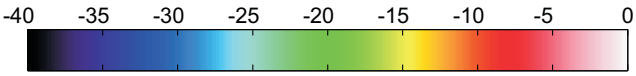

(c) Color - Amplitude Scale

Figure 14: Uniform excitation with scattering: two snapshots in time.

effective at focusing energy to the desired location. In the presence of significant clutter and/or wave speed gradients, waves produced by each of the sources are subject to scattering off multiple objects, causing the waves to be broken up and arrive incoherently at the focus location. Though scattering and speed gradients significantly reduce the effectiveness of the time-delayed differentiated Gaussian excitation, this method shows improvement over uniform excitation with respect to wave front coherence and excitation level at the focus location (Figure 16). The primary weakness of time-delay focusing is that in order to accurately calculate the propagation delays between each source and the focus point, one must know the propagation speed in the medium between the source and the focus point. In the case of a medium where propagation delays cannot be precisely calculated due to varying material properties or wave speed gradients, any assumption of this propagation speed is an approximation at best.

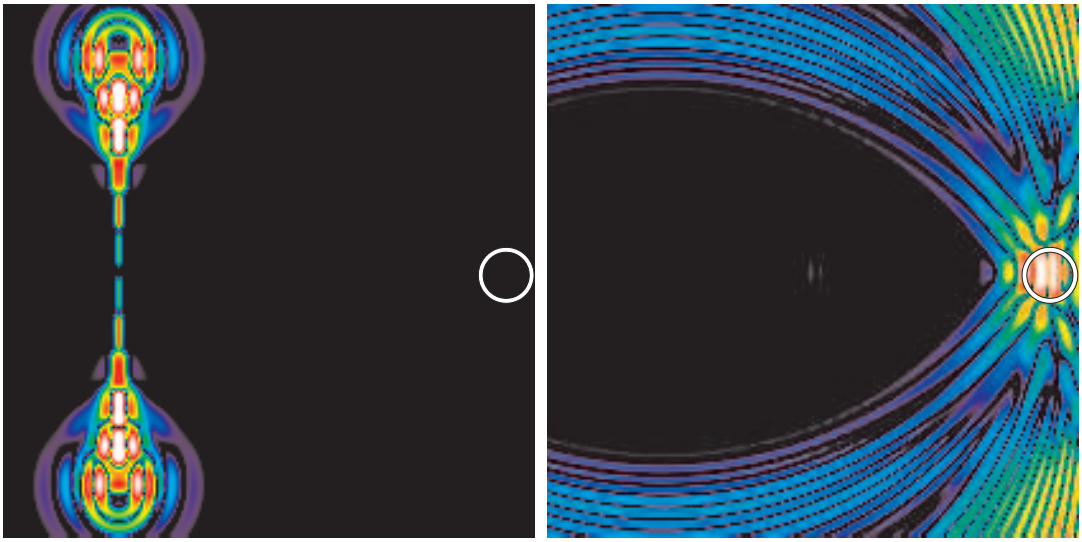

(a) The time-delayed pulses are launched from the 12 sources.

(b) The focused wave fronts arrive at the desired focal point.

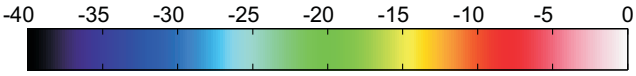

(c) Color - Amplitude Scale

Figure 15: Time-delayed focusing with no scattering: two snapshots in time. The focal point is indicated by a circle.

3.2.2.3 Time-Reversal Focusing Excitation

The third excitation type is time-reversal focusing. For time-reversal, each source is excited individually, and a pulse is propagated from each of the sources, recorded at the focal point and then reversed in time. The time-reversed signals are then transmitted from their corresponding source locations. Figure 17 shows two snapshots in time of a time-reversal excitation propagating through the elastic medium and focusing at a point in the central region of the medium. A particular advantage of time-reversal over time-delayed focusing techniques is that it requires no knowledge of the propagation speed in the medium.

For time-reversal focusing, the time-reversal signals are formed as described in Sec. 2.3. Then the time-reversed signals are transmitted simultaneously from their respective sources. Especially in the presence of clutter, no coherent wave front is

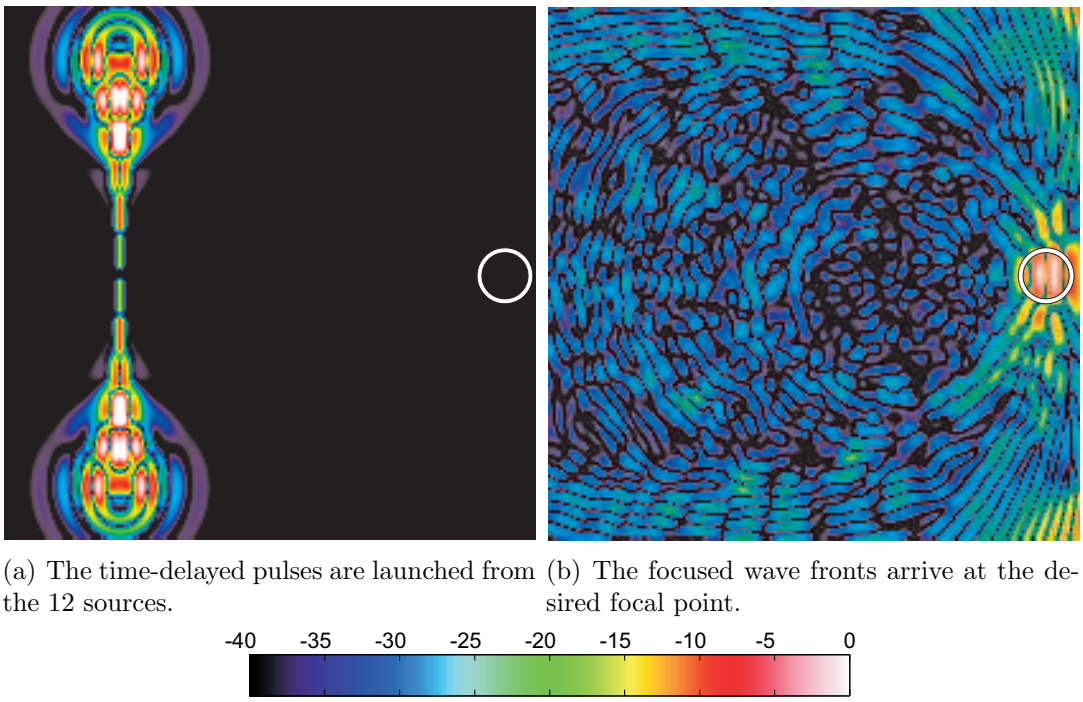

(a) The time-delayed pulses are launched from the 12 sources.

(b) The focused wave fronts arrive at the desired focal point.

(c) Color - Amplitude Scale

Figure 16: Time-delayed focusing with scattering: two snapshots in time. The focal point is indicated by a circle.

produced. Even though time-reversal fails to produce a coherent wavefront propagating through the medium, the waves sum constructively at the focus point in space and time as predicted by time-reversal theory (Section 2.2), producing a large excitation only at that location. Figure 18 demonstrates that in the presence of multiple scattering objects, time reversal allows for effective excitation at the target location.

3.3 Experimental Time-Reversal Focusing

3.3.1 Experimental Method

The experimental results are obtained in a laboratory at the Georgia Institute of Technology (Figure 19)[3, 28]. A large concrete wedge-shaped tank is filled with approximately 50 tons of damp compacted sand. Sand is chosen as the background medium because its seismic properties are similar to many types of soil, and because it is straightforward to recondition disturbed sand. This allows for easy burial and

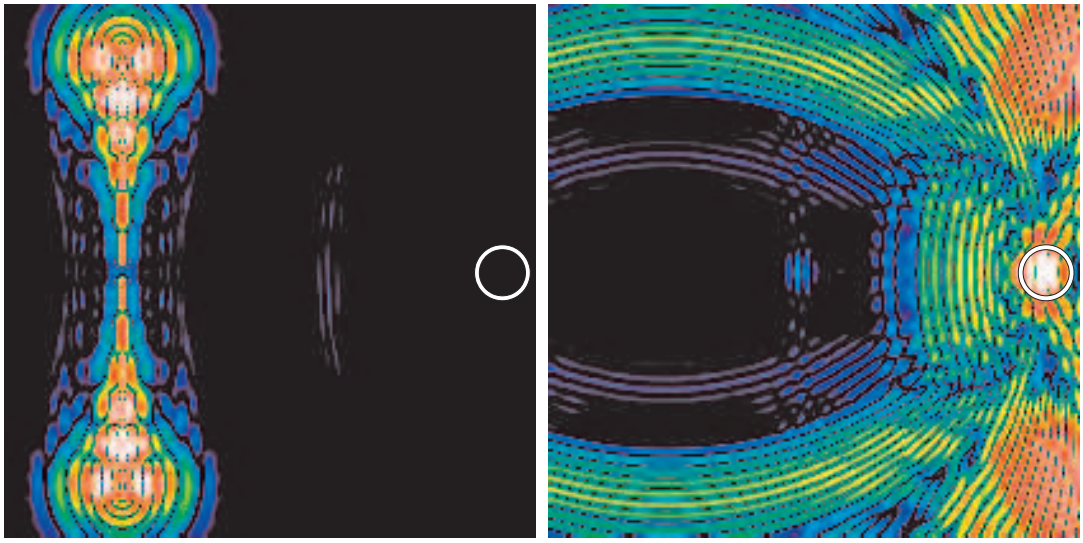

(a) The time-reversed signals are launched from the 12 sources.

(b) Time-reversal focuses at the desired focal point.

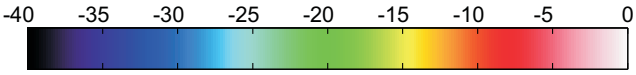

(c) Color - Amplitude Scale

Figure 17: Time-reversal focusing with no scattering: two snapshots in time. The focal point is indicated by a circle.

removal of scattering objects and targets in the tank. The method of data collection in the experimental facility follow the methods described in Section 2.3.

The seismic waves are generated by an array of 12 electrodynamic shakers (Figure 20). A short metal bar foot is attached to each electrodynamic shaker. The shaker and metal foot are placed in contact with the sand and the 12.5 cm × 1.27 cm × 2.54 cm aluminum bar foot couples seismic energy into the sand.

Once the shakers are used to excite elastic waves in the sand tank, a non-contact electromagnetic sensor (radar vibrometer) is used to record the displacement of the surface of the ground. The vibrometer is scanned across the surface of the sand using a computer controlled positioning system. The surface is sampled at 2 cm increments ($\Delta x = \Delta y = 2$ cm) over a 1.2 m × 0.8 m area. The radar has a spot size of approximately 2 cm × 2 cm and records data at each location for 4.096 s at a sampling

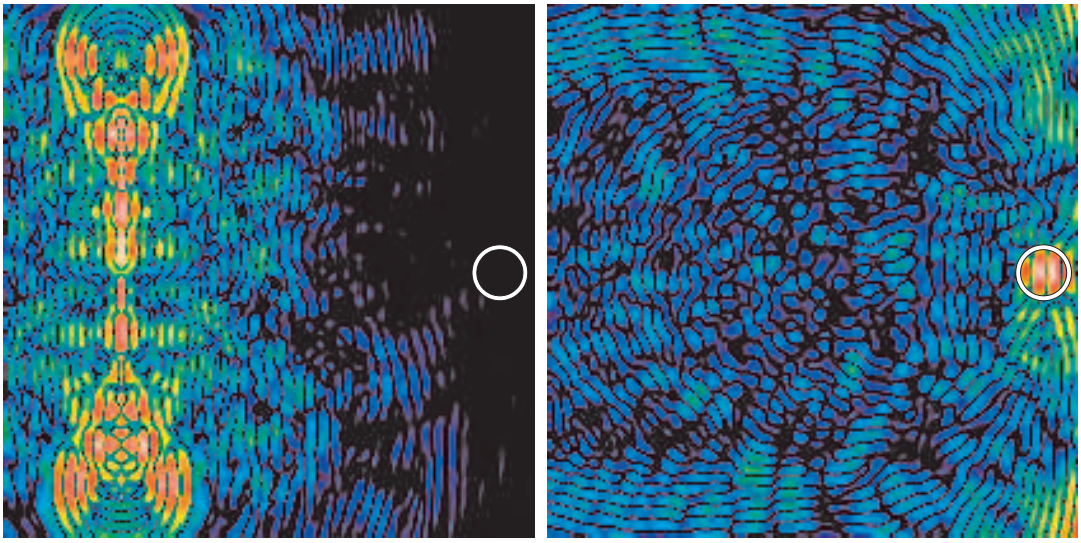

(a) The time-reversed signals are launched from the 12 sources.

(b) Time-reversal focuses at the desired focal point.

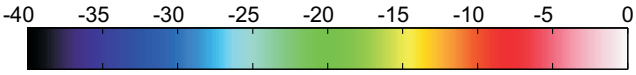

(c) Color - Amplitude Scale

Figure 18: Time-reversal focusing with scattering: two snapshots in time. The focal point is indicated by a circle.

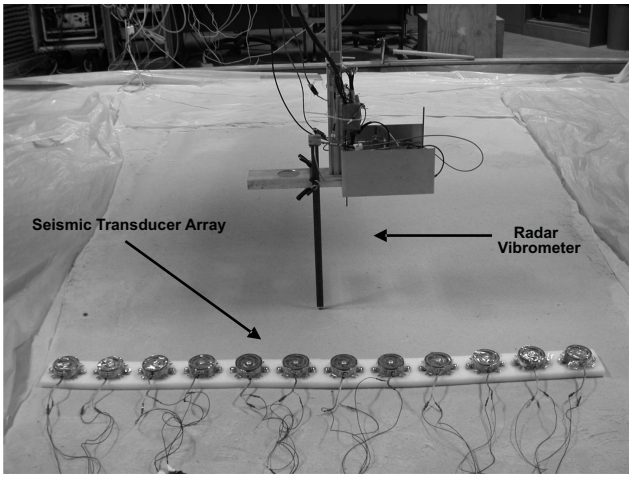

Figure 19: The experimental facility. The seismic transducer array and the antenna are positioned over the sand tank.

rate of 8 kHz. By making many measurements, each at a different location on the surface, the displacement of the entire scan region can be constructed synthetically.

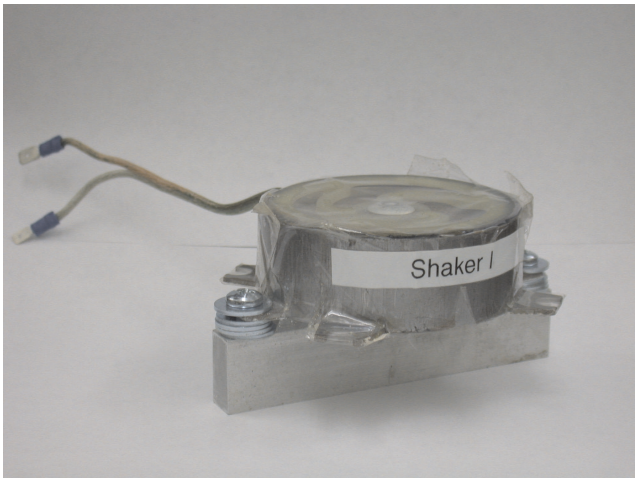

Figure 20: One of the electrodynamic shakers used as an excitation source. The bar foot is attached.

After the entire scan has been completed, a data array of displacement information is available, $U_(x_i, y_j, t_k)$, where

$$\begin{aligned} x_i &= i\Delta x, \qquad i = 0, 1, \ldots, \tfrac{X}{\Delta x} \\ y_j &= j\Delta y, \qquad j = 0, 1, \ldots, \tfrac{Y}{\Delta y} \\ t_k &= k\Delta t, \qquad k = 0, 1, \ldots, \tfrac{T}{\Delta t} \end{aligned} \quad , \tag{38}$$

and where X and Y are the dimensions of the scan region and T is the duration of time for which each measurement is recorded.

The theoretical development of time-reversal focusing assumes that all sources and receivers are infinitesimally small points. In the physical experiment, the sources are distributed due to their use of a foot to couple energy into the ground. Similarly, the receivers are also distributed since the smallest resolvable area is limited by the spot size of the radar. While these distributed elements represent a deviation from the theoretical development of time reversal, empirical observations demonstrate that the effectiveness of time-reversal focusing is not significantly impacted by the use of distributed sources and receivers.

A total of 113 rocks are buried in the sand tank (Figure 21) in order to introduce inhomogeneities into the sand. The rocks are randomly distributed throughout the tank both in location on the surface and burial depth. The burial region extends far beyond the scan region. Rocks are buried to within 0.5 m of the edges of the sand tank. The maximum burial depth of the top of any rock is limited to approximately 20 cm. The size of the rocks varies from 10 cm in diameter to approximately 35 cm in diameter (Figure 22).

Figure 21: The layout of the rocks before being buried below the surface.

In order to effectively illuminate a buried target using time-reversal focusing, the excitation pulse that reaches the target should be both broadband and compact in time. In addition to being useful for time-reversal focusing, a compact pulse allows for better separation of incident pulses and those reflected off a target. This separation is important for affiliated detection techniques such as time-reversal imaging [29, 30].

In order to excite elastic waves in the ground, an excitation signal is formed digitally, passed through a D/A converter, a power amplifier, and into the electro-dynamic shaker. The data will then be measured using the non-contacting ground

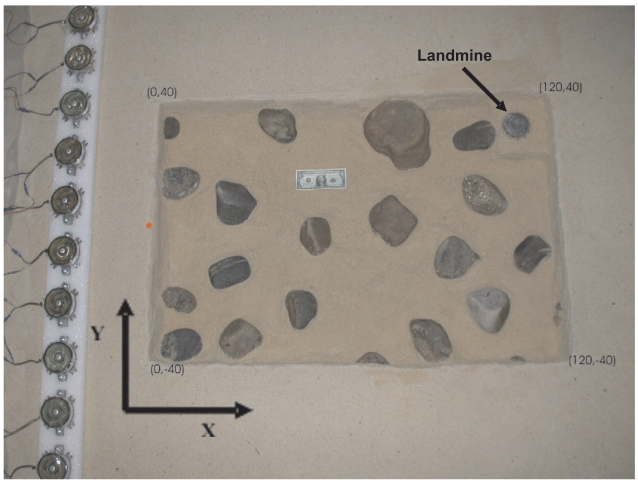

Figure 22: The scan region has been excavated to show the final buried rock distribution. The TS-50 landmine and the dollar bill are for scale.

sensor and recorded by the computer controlled positioning system. This procedure is described by the flowchart in Figure 23.

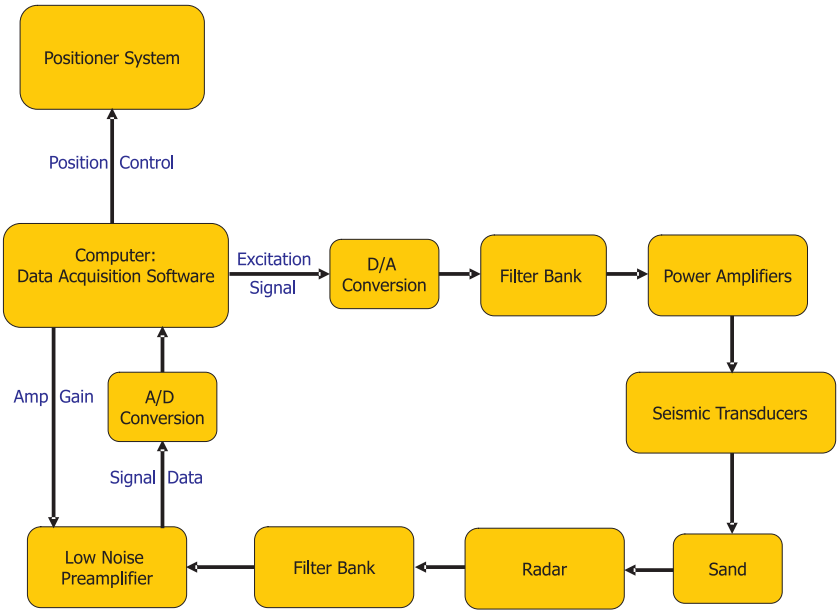

Figure 23: A flow graph showing the interaction of the different components in the data acquisition system.

Once the system excites the elastic wave transducers, the attached foot then couples the transducer motion into the sand, and the excitation signal propagates through the sand and interacts with objects buried in the tank. The transfer function of the electrodynamic shaker and the coupling of the shaker foot to the ground modify the excitation signal such that the signal that arrives at the target location in the medium is significantly different from the electrical signal which is transmitted to the seismic transducer. The other elements in the signal path (A/D, amplifier, etc.) have a negligible effect on modification of the signal. The most dramatic alteration of the original excitation signal is caused by the coupling between the shaker and the ground. In the case of time-reversal focusing, this effect is more pronounced because the signal passes through the system twice, doubling the effect of the shaker-ground coupling.

To achieve the best results from time-reversal focusing, it is important to ensure that the pulse that arrives at the target is broadband and temporally compact. A practical way to do this is to design an inverse filter to restore the original response of the excitation signal. The propagating wave in the sand contains several different wave types, but the one of principal interest in the detection of buried targets is the Rayleigh surface wave. In order to most effectively design a filter that makes the Rayleigh wave temporally compact and broadband, a signal processing technique [31] is used to extract the Rayleigh wave mode from the total propagating wave.

A Wiener filter is designed that conditions the observed Rayleigh wave mode excitation signal resulting in a filtered excitation signal that is very similar to the desired temporally compact, broadband excitation pulse. A post-emphasis filter implementation is chosen because of the slightly non-linear nature of the coupling between the shaker foot and the ground. A pre-emphasis filter would excite large amplitude displacements of the seismic transducer, which would drive the sand into an undesired non-linear response. The recorded signal remains above the noise floor over the entire frequency range of interest, thereby making the post-emphasis filter an acceptable

filter implementation scheme. Figure 24 demonstrates the addition of the Wiener Filter to the data processing procedure.

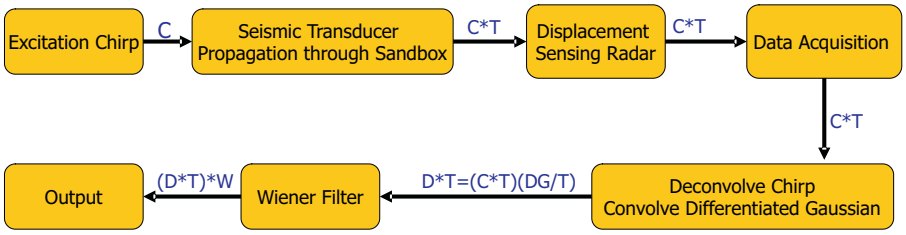

Figure 24: Flow graph showing the effect on the signal of its propagation through the experiment.

The filter coefficients are determined by recording signal outputs in an uncluttered medium, and extracting the Rayleigh wave mode. This information is used to design the Wiener filter using the Stieglitz-McBride method. The Stieglitz-McBride method iteratively minimizes the difference between the desired and designed filter impulse responses for computation of the optimal least-mean-square filter coefficients [32]. The frequency and time-domain responses of the un-filtered excitation signal, the desired signal, and the Wiener-filtered signal are displayed in Figure 25.

3.3.2 Experimental Results

Focusing results for the three excitation methods (uniform excitation, time delay focusing, time-reversal focusing) are first presented for a focus location near the center of the scan region. Subsequently, three additional focusing locations are chosen. These particular locations are deliberately chosen in order to examine the relative effectiveness of time-reversal focusing when it is impeded by scattering, or very near or far from the source array. Time-reversal focusing is also used to illuminate a TS-50 landmine in two of these locations. For this case, the results of time-reversal focusing are compared to the results when the transducer array is uniformly excited.

The first set of results presented in Figure 26 are time snapshot images comparing the effectiveness of the different focusing methods for a location near the center of the

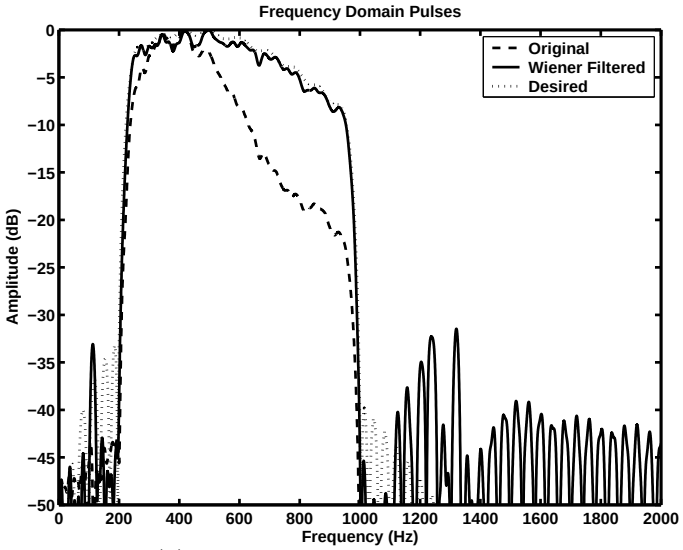

(a) Frequency domain responses

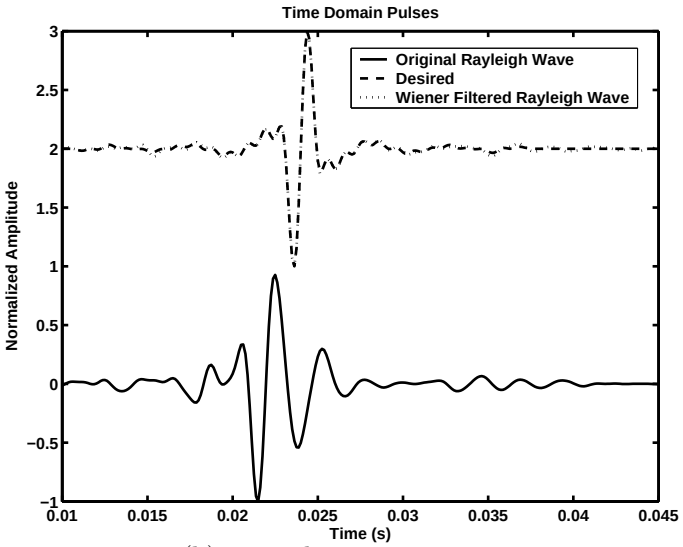

(b) Time domain responses

Figure 25: Wiener filter design

scan region. These images are formed by considering the displacement array, $D(x, y, t)$ in Equation 38 for some particular time, t'. The results are presented as pseudo-color graphs of the magnitude of the vertical component of the particle displacement at the surface. The pseudo-color scale used in the viewgraphs is a 40-dB logarithmic scale from white (0 dB) to black (-40 dB). The images are normalized by the total energy delivered by the excitation signals to the elastic wave sources.

This normalization begins by calculating the relative amounts of energy in each of the complete sets of excitation signals. For each set of K excitation signals of length T, the i^{th} excitation signal can be written as $\epsilon_i(t)$. The energy contained in that entire set of signals is proportional to,

$$E = \sum_{i=1}^{K} \sum_{t=0}^{T} \epsilon_i^2(t). \tag{39}$$

Once the amount of energy transmitted to the sources is known or each set of excitations, the displacement amplitude results are all normalized by the square root of the inverse of the energy normalization factor. This is the factor which allows for direct comparison of the amplitude results, and is written as,

$$norm = \sqrt{\frac{1}{E}}. \tag{40}$$

The first case is uniform excitation of the transducer array (Figure 26a). An excitation pulse is launched from the source array, located to the left of the scan region. As the pulse propagates through the cluttered scan region, the wavefronts are broken up by the scattering objects in the medium. An excitation pulse not modified by scattering would appear as a set of parallel, straight wave fronts propagating away from the sources. Observation of the provided time snapshot for the uniform excitation case demonstrates that the wavefronts are significantly altered by the scattering objects.

For the time-delayed excitation, an attempt is made to focus to a point near the center of the scan region, indicated by the label, *Focus Point* in Figure 26b. The speed of the Rayleigh wave is estimated from the uniform excitation experiment and used to calculate the appropriate time delays. In this case, the time-delayed focusing attempt misses the desired focus point. The most likely reason for this is the propagation velocity gradient across the surface of the tank. If the gradient is strong in the direction normal to the propagation direction, the wave front moves faster on

one side than the other, causing asymmetrical arrival at the focus point. A second factor is the proximity of the desired focal location to a large rock. This rock also alters the propagation speed and path of the pulses. The cumulative effect of these conditions is that the components from each of the sources add coherently, but in the wrong location.

An examination of an attempt to focus on the same location using time-reversal focusing demonstrates significant improvement over the time-delayed focusing case (Figure 26c). The time-reversal focusing method is relatively insensitive to propagation velocity gradients and the presence of inhomogeneities in the medium. This indicates that time-reversal offers a distinct advantage in focusing when the propagation medium contains unknown variations in the propagation speed, and un-catalogued scattering objects.

A second method of presenting the results from Figure 26 is shown in Figure 27. This presentation of the data displays the maximum displacement at each location over the entire time record. This image is formed by creating and displaying the array, $M(x, y)$ where,

$$M(x_i, y_i) = \max_k |D(x_i, y_i, t_k)|. \tag{41}$$

The results are presented as pseudo-color graphs of the magnitude of the vertical component of the particle displacement at the surface. The pseudo-color scale used in the viewgraphs is a 40-dB logarithmic scale from white (0 dB) to black (−40 dB).

The scattering effects of rocks and other objects are visible in the uniform excitation case (Figure 27a). There are also areas of the scan region that are not effectively excited by the pulse, and these will be referred to as shadow regions. An examination of the time-delayed excitation graph (Figure 27b), shows that it focuses energy to a small area near the desired excitation point, but not on top of it. As discussed previously, this is due to propagation velocity gradients in the medium, and the presence

of scattering objects. In a highly cluttered and inhomogeneous environment, time-delayed focusing fails to excite the focus point effectively. This makes time-delayed focusing excitation only marginally useful for detection of near surface targets in the presence of large scale clutter and inhomogeneity.

The time-reversal focusing result (Figure 27c) is qualitatively similar to the time-delayed excitation focusing graph. A notable exception is that the maximum displacement occurs at the desired focus point in the time-reversal case. The reason for this improvement is that the time-reversal method inherently incorporates the effects of scatterers and variations in propagation velocity when calculating the time-reversed excitation pulse. It should also be noted that the displacement at the focus point is much larger than the displacement throughout the rest of the medium. This means that the interaction of the excitation pulse with the scattering objects has been significantly reduced in comparison to the uniform excitation case.

In the results presented above, it is clear that time-reversal focusing yields significant advantages over the other excitation methods in the presence of clutter and variations in wave speed. To further investigate the effectiveness of time-reversal focusing in other circumstances, the time-reversal focusing method is applied to several new locations. These locations are selected by examining the maximum displacement graph for the uniform excitation experiment (Figure 28). Two locations are chosen that are in shadow regions, where very little energy arrives. These locations will be called *Focus Point 1* and *Focus Point 2*. A third point (*Focus Point 3*) is chosen that is far from the source, at $X = 110\,\text{cm}$, $Y = -25\,\text{cm}$. By examining *Focus Point 3*, it is possible to study the improvement afforded by time-reversal when the desired focus point is already effectively illuminated using uniform excitation of the elastic wave sources. All three focus points are noted by the white crosses on Figure 28.

Time-reversal focusing to *Focus Point 1* attempts to focus energy on top of a large rock. The results are shown in Figure 29a. Time-reversal focusing does increase the

excitation level at the desired point, but actually focuses in front of the intended focus point. In *Focus Point 2*, the second shadow-region focus location, similar results are observed in Figure 29b. For both focus points, time-reversal focusing improves the acoustic illumination at the focus point, but the actual focus spot is in front of the desired focus spot.

The results presented in Figure 29a measure a snapshot of displacement at a particular time. In the case of Figure 29a, time-reversal appears to miss the focus point and focus in front of the desired location. If this image were a measure of energy, instead of displacement, the image would be able to account for the greatly increased stiffness of the rock present at the desired focus point. This may demonstrate that time-reversal focusing does in fact focus significant energy to the desired location.

This explanation may account for the absence of significant displacements at the focus point. Further, the observation of a large apparent focal point between the source array and the desired focal point can be explained using a simple model. The model is presented in Figure 30. For the coordinate system assumed in these experiments, consider a rock of an arbitrary thickness in X, but of infinite extent in Y and Z. As the wave propagating from each of the sources arrives at the medium interface, the majority of the energy in the Rayleigh wave will be reflected off the interface between the rock and the sand. This creates a pseudo-focal point, R', in front of the rock-soil interface. In this simple case, R' will be the same distance (δ) away from the interface as the desired focus, R.

In the actual, less simplistic case, where the extent of the rock is finite, a larger portion of the incident wave is unaffected by the abrupt change in material properties. These effects combined with inhomogeneities in the medium cause variations in the strength, size, and location of the pseudo-focal point. These effects are apparent when comparing time-reversal focusing to *Focus Point 1* and *Focus Point 2* in Figure

29a and Figure 29b. In the former, where the scattering rock is larger in the Y-dimension (Figure 28), a more distinct pseudo-focus point is apparent. This indicates that more of the incident waves are partially reflected and re-focus in front of the desired focus location. This effect is diminished for *Focus Point 2* in Figure 29b, where the scattering rock is significantly smaller.

In the final case (Figure 29c), time-reversal focuses almost exactly at the desired location and some improvement in the excitation level is observed in comparison to the uniform excitation case. The small offset of the actual focus point from the desired focus point can be attributed to the phenomenon discussed above and described in Figure 30.

The motivation for pursuing high excitation levels at a specified location is to more effectively illuminate a landmine buried at the focus location. To that end, the effect of time-reversal on illumination of a landmine is presented. Two locations are chosen, one of which is in a shadow region.

For each point, the maximum displacement level over time is used as a basis for performance comparison. For the focus location in a shadow region (Figure 31), time-reversal focusing provides an approximately 18 dB improvement over the uniform excitation case. In addition to raising the relative amplitude of the displacement at the location of the mine, the relative signal levels over the majority of the scan region are reduced significantly, providing better contrast between the landmine and its background.

In the second position (Figure 32), the displacement levels are high enough in the uniform excitation case to effectively illuminate the landmine. While time-reversal focusing does focus energy to the location of the landmine and drop the relative displacement in the background, the increase in the displacement at the location of the resonating landmine is approximately 12 dB.

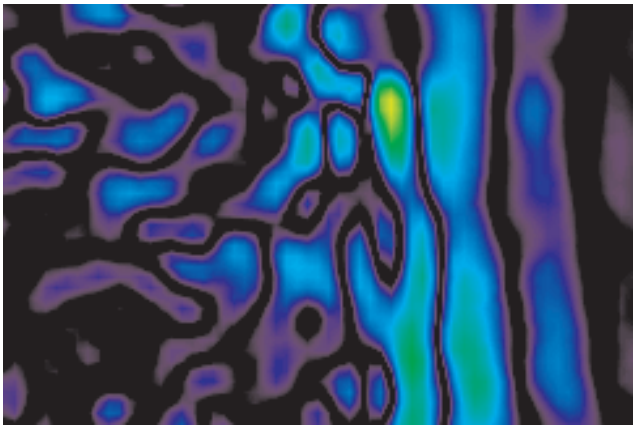

(a) Uniform excitation

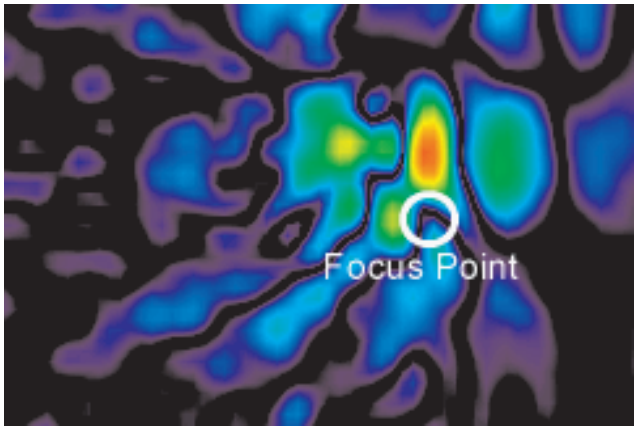

(b) Time-delayed excitation

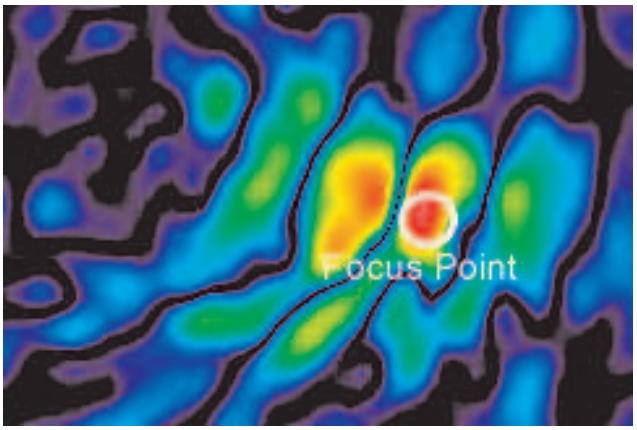

(c) Time-reversed excitation

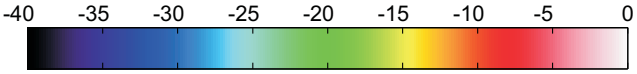

(d) Color - Amplitude Scale

Figure 26: Time-snapshots for Focus Point 1. Images are on a 40 dB pseudo-color scale: 0 dB(white) to −40 dB(black).

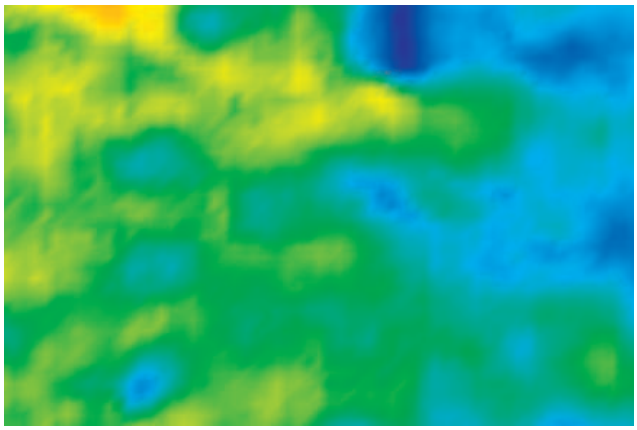

(a) Uniform excitation - maximum displacement

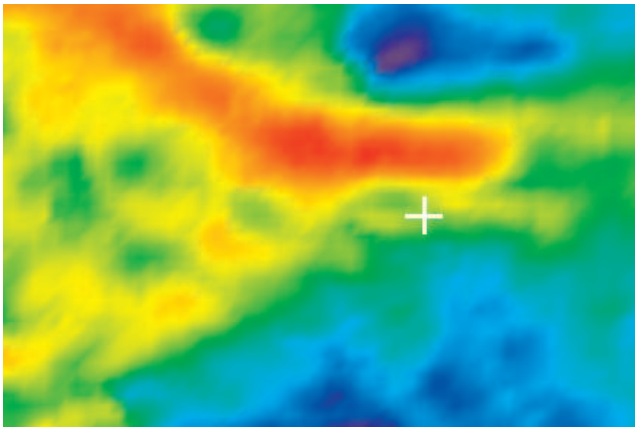

(b) Time-delayed excitation - maximum displacement

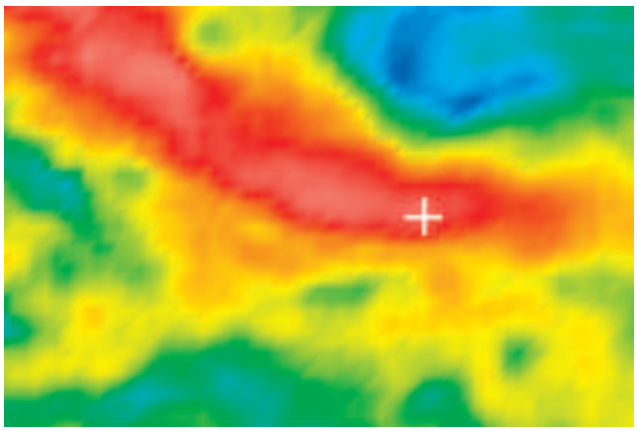

(c) Time-reversed excitation - maximum displacement

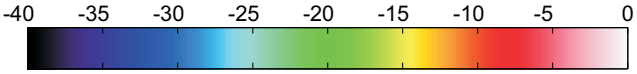

(d) Color - Amplitude Scale

Figure 27: Maximum displacement for Focus Point 1. Images are on a 40 dB pseudo-color scale: 0 dB(white) to −40 dB(black).

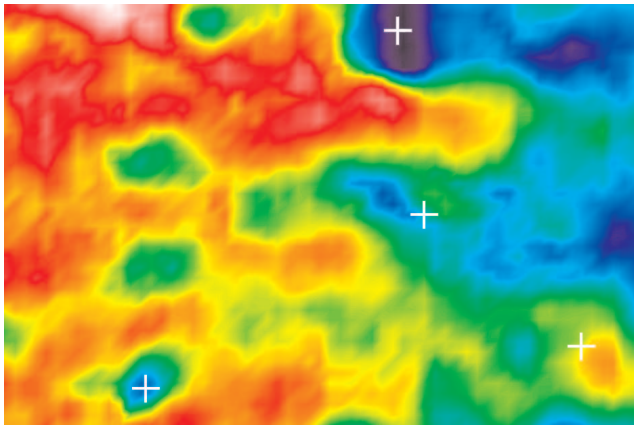

(a) Uniform excitation - maximum displacement. Locations chosen for focusing are indicated by white crosses. The image is presented on a 20 dB pseudo-color scale: 0 dB(white) to −20 dB(black)

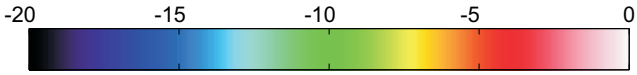

(b) Color - Amplitude Scale

(c) Layout of rocks in experimental setup. Locations chosen for focusing are indicated by white crosses.

Figure 28: Focusing Locations

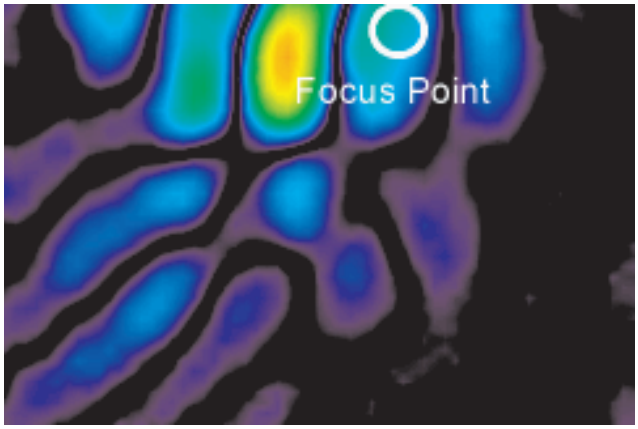

(a) Shadow region: *Focus Point 1*

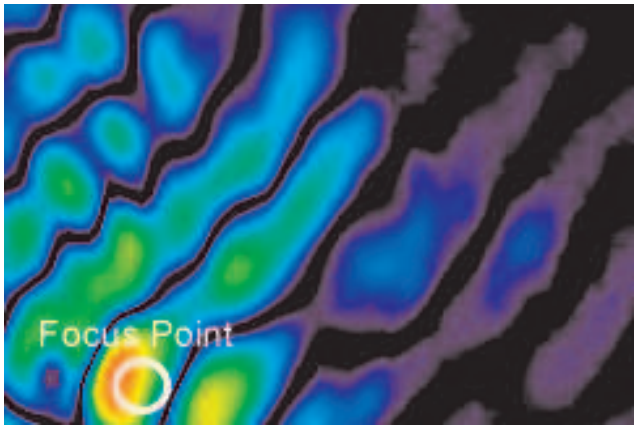

(b) Shadow region: *Focus Point 2*

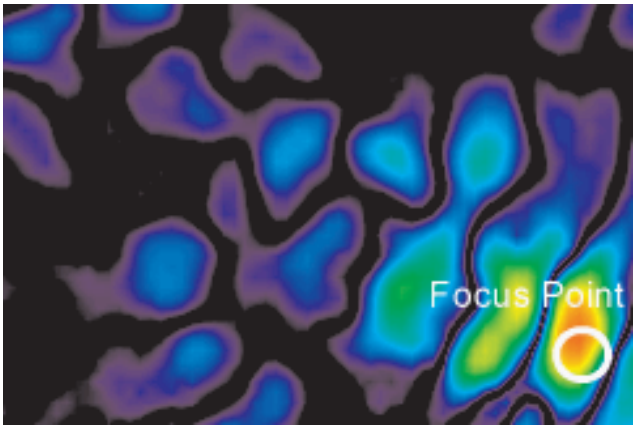

(c) Normal excitation region focus point

Figure 29: Time-Reversal Excitation. The desired focus point is indicated in each image. Images are on a 40 dB pseudo-color scale: 0 dB(white) to −40 dB(black).

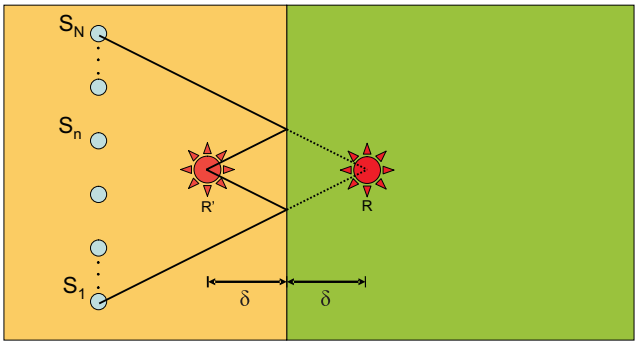

Figure 30: The pseudo-focus point (R') created by an infinite half-space rock.

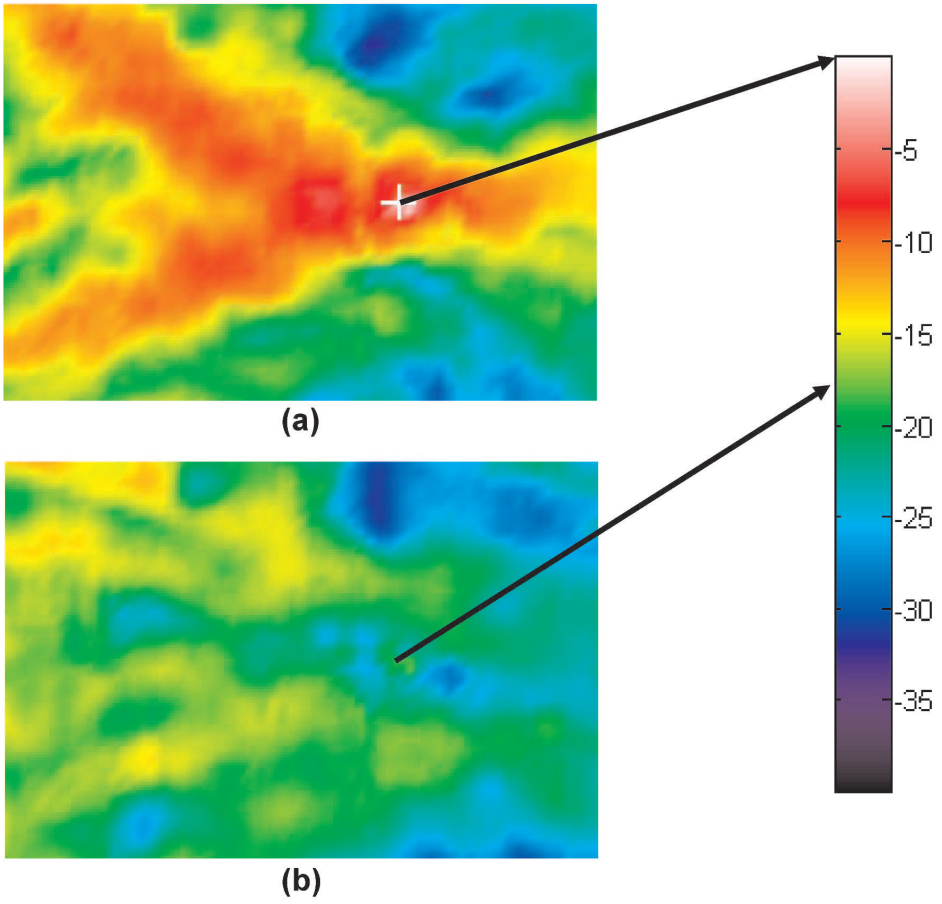

Figure 31: A comparison of the maximum displacement at the location of a buried TS-50 for the (a) time-reversal and (b) uniform excitation cases.

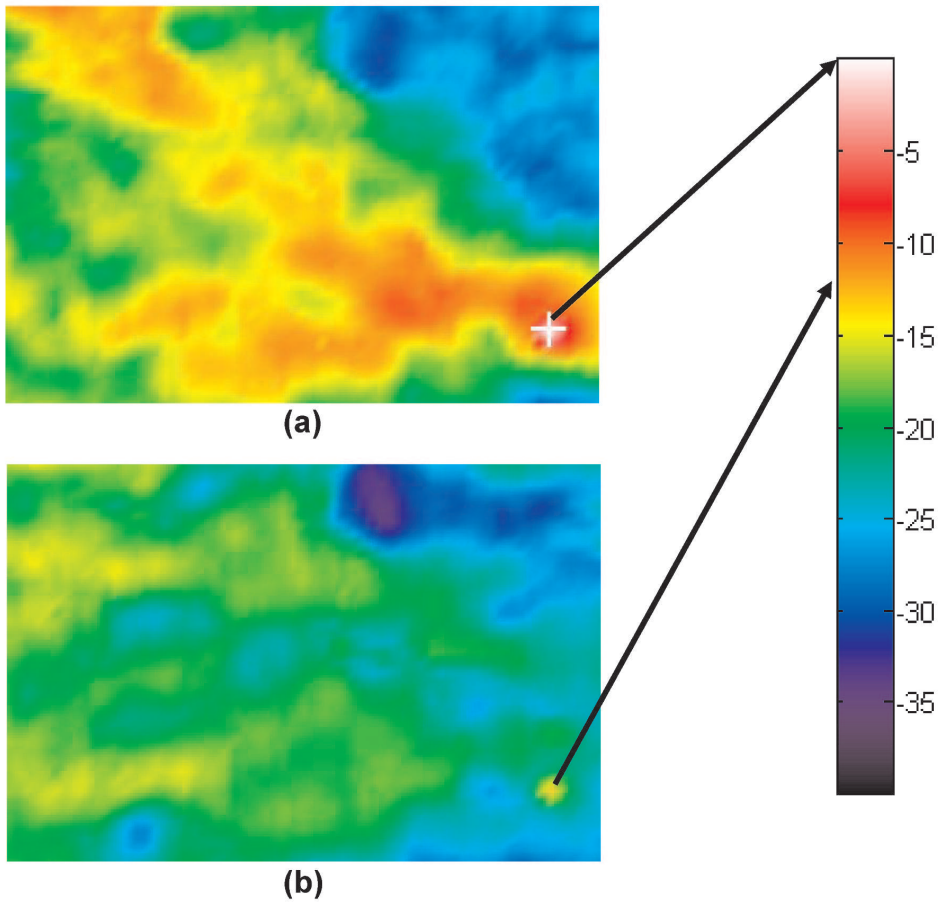

Figure 32: A comparison of the maximum displacement at the location of a buried TS-50 for the (a) time-reversal and (b) uniform excitation cases.

CHAPTER IV

EXPERIMENTAL TIME-REVERSAL FOCUSING IN A HEAVILY SHADOWED REGION

4.1 Motivation

The initial set of time-reversal focusing experiments (Section 3.3) demonstrated that time reversal works well in areas that are difficult to excite using traditional excitation methods. Time-reversal focusing effectiveness was compared to the performance of time-delay focusing techniques in regions shadowed by large rocks and proved to be more effective. The ability of time-reversal focusing to focus in shadowed regions is one of its most useful qualities and is worthy of further study. In the previous studies in Chapter 3, the shadow regions were relatively small in extent and located far enough from the source to subtend only a small portion of the aperture of the source array. In this chapter, time-reversal focusing is examined when a large barrier creates a much more significant shadowed region. The effect of the barrier is so significant that it almost entirely eliminates the initial forward travelling wave (the ballistic wave) excited by the source.

4.2 Experimental Method

The experimental method used for collecting the results is similar to the one described in Section 3.3, with a few significant modifications. The same sand tank, computer controlled data acquisition system and array of 12 electrodynamic shakers are used in these experiments. The two noteworthy differences in the experiment are the sensor used to measure wave propagation and a new averaging method used to improve the signal-to-noise ratio during time-reversal focusing.

4.2.1 Ground-Contacting Sensor Array

The non-contacting radar vibrometer used in the previous set of experiments has been replaced with an array (Figure 33) of specially designed ground contacting accelerometers [33]. These sensors are inexpensive, compact, and couple to the ground well, and lightly enough to be safe for use in landmine detection applications. There are several advantages to this new sensor that motivate the change from the non-contacting radar sensor.

Figure 33: The accelerometer array contains 30 ground contacting accelerometers.

The non-contacting sensor system employed a single measurement antenna that scans the region of interest, taking measurements at individual points. In order to synthetically generate useful data over the entire scan region, the electromagnetic sensor measures data every 2 cm, which for a 1 m^2 area requires 2601 measurement points. A standard size scan region of 1.6 m $\times$ 2 m takes in excess of 12 hours to complete using the electromagnetic sensor. The array used in these experiments consists of 30 accelerometers in a 3 $\times$ 10 array spaced 3.429 cm apart in X and 10.287 cm in Y (Figure 34). The measurements are interlaced along the Y direction to synthetically generate a grid of measurement points with a spacing of 3.429 cm between measurement points in both X and Y (Figure 35). Use of the array for

measurement decreases measurement time for a single scan from over 8 hours to approximately 35 minutes.

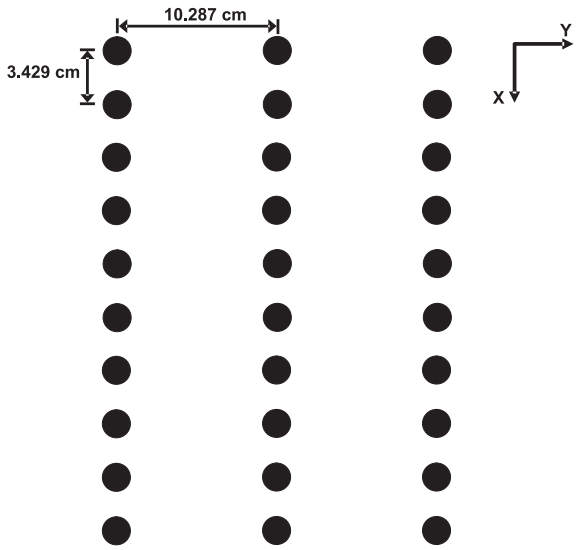

Figure 34: Spacing of the accelerometer array.

In addition to gains in scanning speed, the accelerometer provides significantly improved high frequency response in comparison to the non-contacting sensor. In the frequency domain, a displacement sensor measures the vertical component of the particle displacement, U. The accelerometer senses the vertical component of particle acceleration, which is the second derivative of displacement. Acceleration can be represented in the frequency domain as $\omega^2 U$. Empirical examinations of the frequency response demonstrate that the acceleration measurement provides a high frequency boost similar to the effect of the Wiener filter that was required in measurements employing the electromagnetic sensor (Section 3.3). Use of the new sensor eliminated the need for the Wiener filter.

In Section 3.3, the Wiener filter was created as a post-emphasis filter to avoid introducing non-linearity into the excitation signals. This meant that the frequency

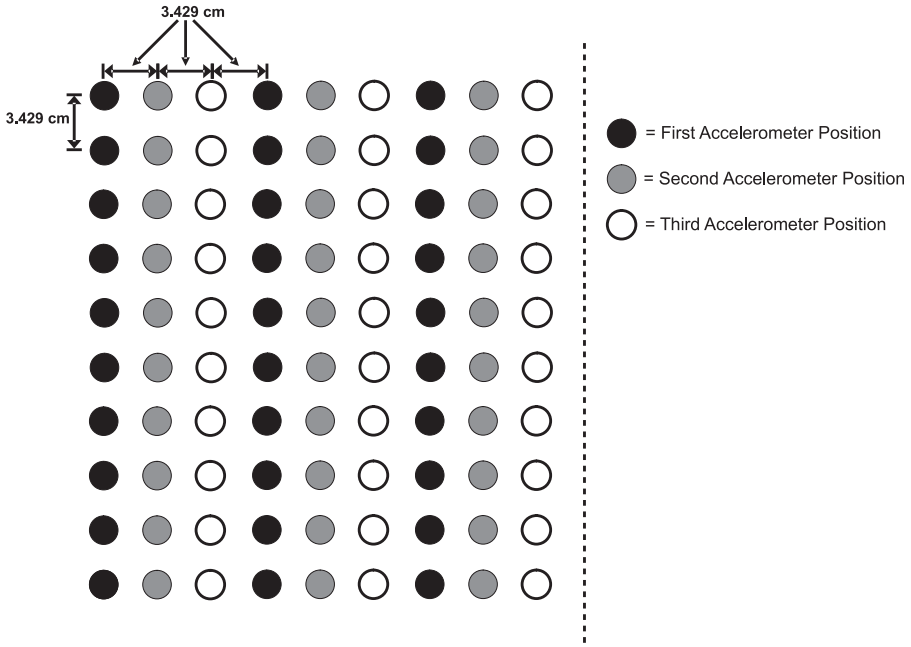

Figure 35: Interlacing scheme for the scan locations of the accelerometer array.

range of the excitation pulses was limited since the Wiener filter could only be applied where it boosted high frequency data that was sufficiently above the noise floor. The inherent high-frequency sensitivity of the accelerometers improves the high-frequency response in such a way that it becomes feasible to examine higher-frequency excitation signals. The high-frequency pulses are important when examining the effects of scattering in time-reversal focusing. Scattering effects are more pronounced as the scattering objects become larger in comparison to the wavelength of the excitation signal.

4.2.2 Time-Reversal Drive Signals: Averaging Method

A second modification to the experimental method is the addition of a special averaging technique in the creation of time-reversal focusing signals. In creating time-reversal drive signals, each seismic transducer is excited individually and the response is recorded at the focus point. This small-amplitude excitation signal is sometimes

close to or below the noise floor for the high frequency components. The small amplitude drive level of each individual shaker is necessary in order to maintain a linear excitation signal. Large amplitude drive levels force the shaker-ground coupling into the non-linear regime [34].

Averaging is employed in order to generate a set of time-reversal focusing drive signals that have a high signal to noise ratio over the entire frequency range of interest. Recall from Section 2.3.2 and Equation 9 that a swept frequency chirp is the excitation fed to the elastic wave transducer. This chirp signal is also used in these experiments to generate the time-reversal drive signals. The chirp excitation, $C(t)$, is sent from a single shaker and recorded at the desired focus point. The resulting signal sent from a single transducer and recorded at the focus point will be,

$$S(t) = C(t) * T(t) + \Phi(t), \tag{42}$$

where the standard Fourier and Inverse Fourier transforms are used to perform the convolution in the frequency domain and return the signal to the time domain [17]. $T(t)$ is the transfer function of the propagation from the shaker to the focus point, and $\Phi(t)$ is the noise that is inherent in the system.

In order to reduce the noise in the system, averaging is employed. The process to record a single signal, $S(t)$, is repeated M times where the i^{th} iteration can be written as,

$$S_i(t) = C(t) * T(t) + \Phi_i(t). \tag{43}$$

Each successive time, the received signal is added to the previous iterations until M signals have been averaged together. For the experiments performed in this chapter, $M = 100$.

$$S_{avg}(t) = \frac{1}{M} \sum_{i=1}^{M} S_i(t). \tag{44}$$

This averaging process significantly reduces the noise level in the received signal, yielding a new averaged drive signal,

$$S_{avg}(t) = C(t) * T(t) + \Phi_{avg}(t) \tag{45}$$

where the standard deviation of the noise signal of $\Phi_{avg}(t)$ decreases as the square root of M, the number of averages. If M is large, $E_{\Phi_{avg}} \ll E_{\Phi_i}$ where E_Φ is noise energy.

After recording and averaging the signals received at the focus point, the composite received signal, S_{avg} (Equation 45, Figure 36a), is transformed to the frequency domain (Figure 36b) and divided by the transfer function of the excitation chirp signal (Figure 36c). This procedure can be described mathematically as,

$$\mathrm{T}(f) = \frac{\mathcal{F}\{S_{avg}(t)\}}{\mathcal{F}\{C(t)\}}, \tag{46}$$

where $\mathcal{F}$ and $\mathcal{F}^{-1}$ are the standard Fourier and inverse Fourier transforms, respectively. This yields a frequency domain transfer function, $\mathrm{T}(f)$, that represents the frequency response of the system (Figure 36d). The frequency response is windowed in the frequency domain to remove extraneous information that lies outside the frequency range of interest. The new transfer function is then transformed back to the time domain to give a time-domain impulse response (Figure 37a),

$$T_F(t) = \mathcal{F}^{-1}\{T(f)W_F(f)\}. \tag{47}$$

The bandpass filter, W_F is defined as,

$$W_F(f) = \begin{cases} 0 & : \quad 0 < f < 99.85\,\mathrm{Hz} \\ 1 & : \quad 100\,Hz \leq f \leq 2\,\mathrm{kHz} \\ 0 & : \quad f > 2\,\mathrm{kHz} \end{cases}. \tag{48}$$

Even though the system may include clutter and other objects that cause scattering, the response to the impulse decays below the noise floor or "rings down" quickly in time. This fast ring down can be observed in Figure 37a: the impulse response is

temporally compact and quickly drops below the noise floor. Once the signal level of the response is sufficiently below the noise floor after $\sim 0.1\,\mathrm{s}$, the remaining portion of the signal adds no additional useful information so this portion of the signal may be discarded. The first 200 ms of the time domain impulse response is kept to ensure ring down significantly below the noise floor, and the rest of the signal is windowed with a rectangular window (Figure 37b). The first 200 ms of the response is then zero-padded to return the length of the signal to 4.096 seconds. This procedure significantly improves the signal-to-noise ratio of the excitation signal. After truncating to 200 ms and zero-padding the signal, $T_{truncated}(t)$, can be written as,

$$T_{truncated} = T_F(t)W_T(t), \tag{49}$$

Where $W_T(t)$ is a window function defined in the time domain as,

$$W_T(t) = \begin{cases} 1 & : \quad 0 \leq t \leq 200\,\mathrm{ms} \\ 0 & : \quad 200\,\mathrm{ms} < t \leq 4.096\,\mathrm{s}. \end{cases} \tag{50}$$

The new "clean" impulse response is then transformed into the frequency domain, multiplied by the frequency domain chirp excitation signal and transformed back to the time domain (Figure 37c), yielding $G(t)$,

$$G(t) = C(t) * T_{truncated}(t). \tag{51}$$

This is the signal that is time-reversed to create the a time-reversal drive signal. This signal conditioning results in a drastically improved signal to noise ratio (SNR) which significantly improves the effectiveness of time-reversal focusing. The procedure is described graphically in Figure 38.

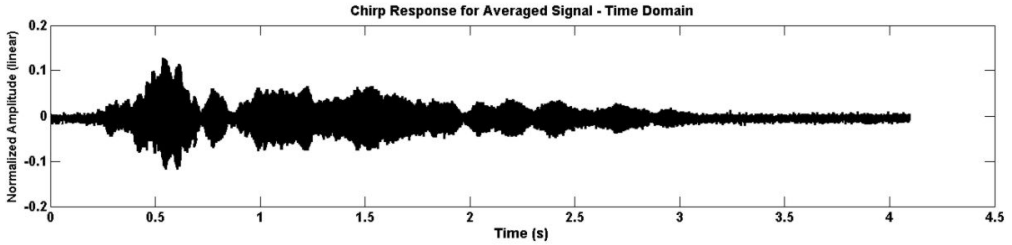

(a)

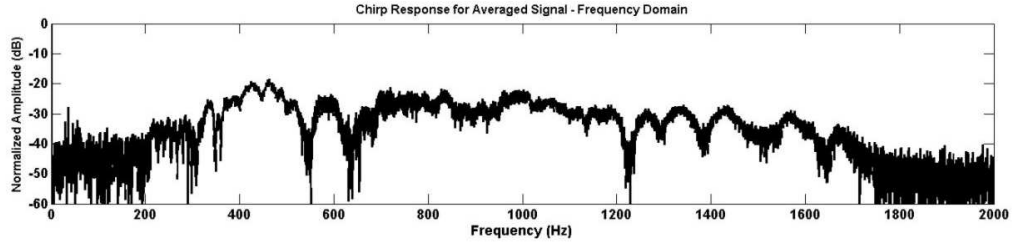

(b)

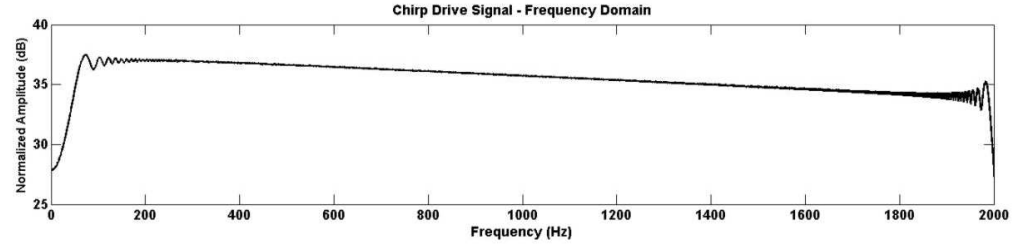

(c)

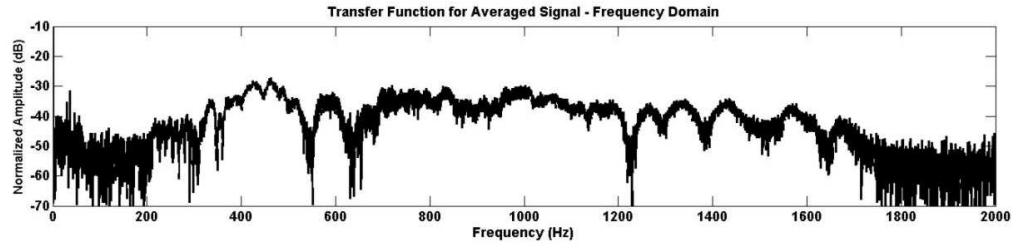

(d)

Figure 36: Representative signals are depicted at several processing steps in the procedure used to create time-reversal drive signals. (a) The averaged received time domain signal. (b) The averaged received signal in the frequency domain. (c) The frequency domain transfer function of the excitation chirp. (d) The Fourier transform of the impulse response of the averaged received signal, i.e. (b) divided by (c).

4.2.3 Blocking the Ballistic Wave

This experiment examines the effects of time-reversal focusing when the ballistic wave is blocked. A barrier was devised that mostly blocks the central portion of the

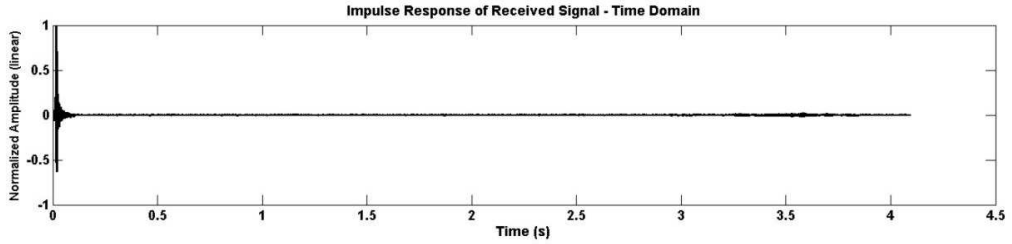

(a)

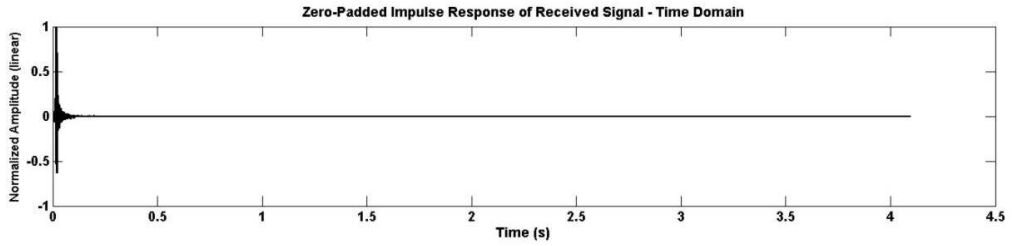

(b)

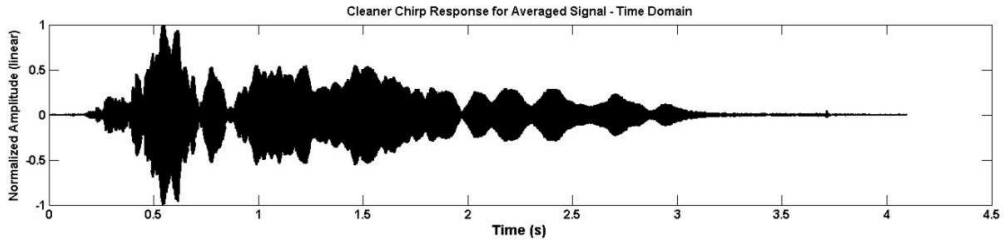

(c)

Figure 37: Representative signals are depicted at several processing steps in the procedure used to create time-reversal drive signals. (a) The time domain impulse response of the averaged received signal. (b) The time domain impulse response of the averaged received signal after truncation to 200 ms and zero-padding to 4.096 s. (c) The time domain "clean" excitation signal after being truncated and convolved with the chirp excitation.

ballistic wave, and focus locations were chosen in the shadowed region behind this barrier. Additional scattering regions on either side of the central barrier ensure that no portion of the incident wave reaches the focus point without passing through a scattering region (Figure 39).

The central barrier consists of a densely packed region of large stones. The stones were buried in a region 85 cm wide by 50 cm long by 33 cm deep (Figure 40). The effects of the central barrier were tested in conjunction with two different sets of

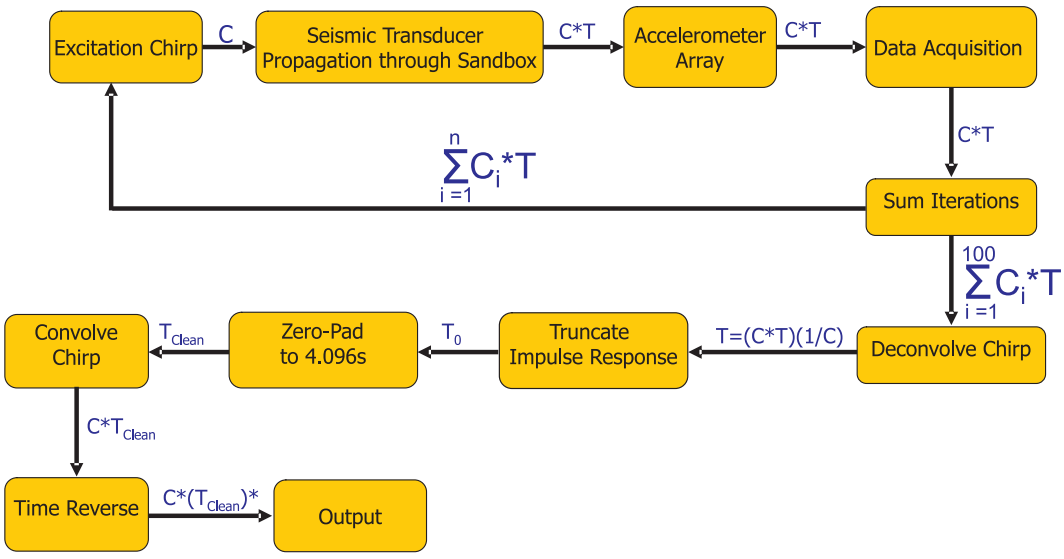

Figure 38: Flowchart showing the data acquisition and processing steps to create time-reversal drive signals.

scattering objects in the peripheral scattering regions.

The first experiment employed equal object densities of medium sized stones that were randomly distributed throughout each peripheral region (14 stones on the right side and 15 stones on the left side). The stones were similar in composition and shape to the ones used to create the central ballistic wave barrier, but were smaller in size (approximately 5 – 7 cm in diameter). The rocks in the peripheral scattering region are buried just below the surface of the sand with the top of the rocks buried 1 – 3 cm below the surface.

A second experiment used 15 concrete cylinders in each peripheral scattering region. The concrete cylinders are approximately 5 cm in diameter and 30 cm long. They are created by filling thin-walled corrugated plastic tubing with standard construction concrete. Corrugated tubing was chosen over smooth-walled tubing as the corrugations provide better contact to the sand, inducing better coupling between the sand and the cylinders.

The cylinders were built by first fitting 30 cm lengths of corrugated plastic into

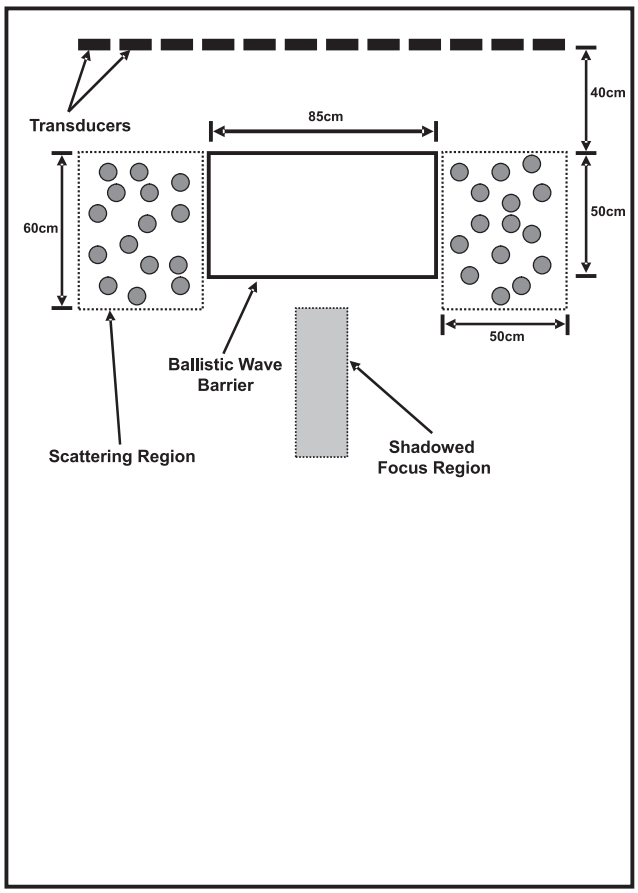

Figure 39: The configuration of the experiment in the sand tank. The ballistic wave barrier is shown in the center, and is surrounded on both sides with regions containing scattering objects. The focus region, located in a shadowed area of the sand tank, is also shown.

rigid PVC forms for casting. The cylindrical forms were then filled with concrete and packed tightly to ensure no air pockets remained inside the forms. After the cylinders were filled, the concrete was cured for 1 week in the PVC forms. The cylinders were removed from the forms and then used as scattering objects. A total of 76 cylinders were built for use as scattering objects (Figure 41).

The cylinders in the peripheral scattering region are each buried individually by digging a vertical hole with an auger that is approximately twice the diameter of the cylinder and then backfilled with sand with the cylinder centered in the hole. The top of the cylinders are buried 1 – 3 cm below the surface of the sand (Figure 43).

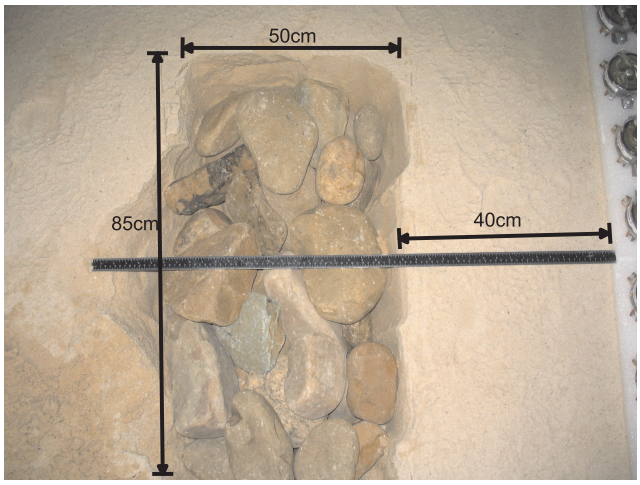

Figure 40: This photograph shows the ballistic wave barrier before being covered with sand. The barrier is comprised of multiple large rocks and effectively blocks the majority of the ballistic energy that arrives from the elastic wave sources.

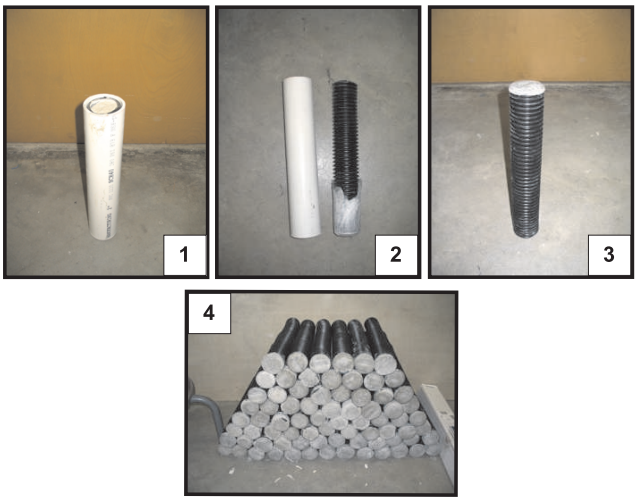

Figure 41: Concrete cylinders in various stages of construction. (1)A completed cylinder inside the rigid PVC form. (2) The cylinder after curing and removal from the PVC form.(3) The completed cylinder. (4) All completed cylinders.

The resulting scattering field combines with the central barrier to effectively block the ballistic wave in the desired shadow region (Figure 44).

Figure 42: The layout of the rock-filled peripheral scattering region. The surface has been excavated to reveal the buried scattering objects. The central ballistic wave barrier is present, but is concealed by sand.

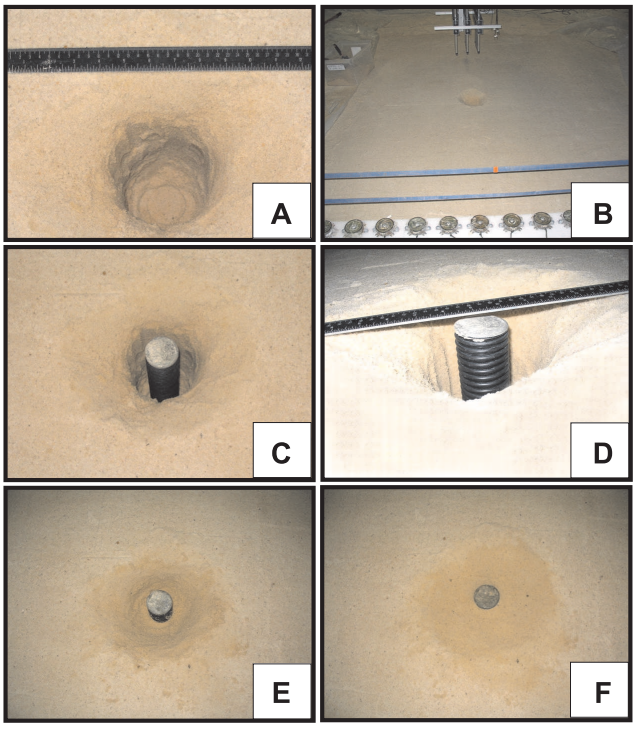

Figure 43: The burial procedure for an individual cylinder in the sand tank. A vertical hole is drilled with an auger (A – B) and a cylinder is placed vertically in the center of the hole approximately 1 – 3 cm below the surface of the sand (C – D). The hole is backfilled to pack the sand flush with the surface of the cylinder (E – F).

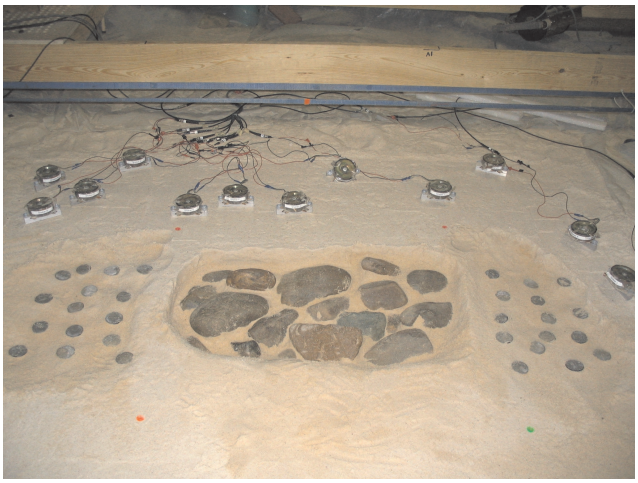

Figure 44: The layout of the cylinder peripheral scattering fields and the central ballistic wave barrier. The surface has been excavated to reveal the buried scattering objects.

4.3 Results: Focusing in a Shadowed Region

The majority of the results will be presented using maximum amplitude plots. However, an examination of time snapshots of the wave propagation for each type of excitation is useful to visualize the impact of blocking the ballistic surface wave. In Figures 45 – 47, time snapshots are presented for each of the three excitation methods described. In addition to the central barrier, rocks are buried in the peripheral scattering regions noted in Figure 39.

The results of the experiments are presented as plots showing the maximum amplitude of the vertical component of the recorded acceleration over the scan region during the entire time record. This image is formed by creating and displaying the array, $M(x, y)$,

$$M(x_i, y_j) = \max_k |A(x_i, y_j, t_k)|. \tag{52}$$

Where A is the acceleration measurement that is analogous to displacement, D, presented in Equation 41 in Section 3.3.2. The results are presented as pseudo-color graphs of the magnitude of the vertical component of the particle acceleration at the

surface. The pseudo-color scale used in the figures is a 40 dB logarithmic scale from white (0 dB) to black (−40 dB).

In order to compare the different focusing methods, the results are normalized with respect to the energy contained in the excitation signals for each of the three excitation methods. The normalization procedure is identical to the one described in Section 3.3.2.

4.3.1 Central Barrier with Rock-Filled Peripheral Scattering Region

A comparison can be made of the performance of three different excitation types: time-reversal focusing, time-delay focusing and uniform excitation. The first experiment presented in Table 4 attempts to focus energy to a shadowed point located at X=80, Y=0 in the sand tank. For the uniform excitation case, the maximum amplitude plots in Figure 48a demonstrate that the central barrier effectively blocks the ballistic wave. Some energy does propagate through the peripheral scattering regions, but this energy is disorganized and does not reach the shadowed region behind the central barrier with any significant energy or coherence.

Time-delay focusing performs even more poorly than uniform excitation at reaching the shadowed region in the presence of the barrier and scattering objects (Figures 48a and 49a). Signals from each of the transducers are time-delayed assuming that the propagation speed through the medium is a constant 94.8 m/s and assuming the normal propagation speed of a surface (Rayleigh) wave through sand as measured in the experimental facility (Figure 11). The propagation speed estimate is formed by assessing the wave propagation speed in uncluttered sand. While it is known that the assumption of a constant propagation speed is inaccurate in the presence of the central barrier, this is an acceptable way to compare the effectiveness of focusing methods. Precise in-situ measurements describing the medium properties at all locations are

almost never available in actual implementations of focusing systems such as in land-mine detection or ultrasound measurements in living tissues or in non-destructive testing applications.

The experiment is repeated for a second shadow-region focusing location at X=100, Y=0 in the sand tank. The results of this experiment are presented in Figures 50 and 51, and demonstrate similar behavior to the first experiment. The results of both experiments confirm that time-reversal focusing performs significantly better than time-delayed focusing and uniform excitation. Time-reversal focusing effectively directs energy to the desired focus point with significant accuracy (Figures 48 – 51). Table 4 summarizes the results.

4.3.2 Central Barrier with Cylinder-Filled Peripheral Scattering Region

This experiment is performed in a manner identical to the case of the rock-filled peripheral scattering region. The cylinder-filled peripheral regions exhibit similar trends to the rock-filled peripheral regions (Figures 52 – 55). The experiment demonstrates that time-reversal focusing is effective with various types of scattering objects present in the medium.

This conclusion is further strengthened by the presence of the central barrier. If the scattering field made of up cylinders or rocks filled the entire scan region, and no central barrier were present, the ballistic wave contribution would dominate the response recorded at the focusing point. In such an experiment, any variation in performance caused by different scattering objects would be much less apparent.

4.3.3 A Comparison of Time-Reversal Focusing with Respect to Scattering Object Geometry

The lack of a ballistic wave allows for close examination of the effects of various types of scattering objects in time-reversal focusing. In some time-reversal focusing experiments, the focusing spot size has been found to be affected by the presence and

Experiment	Focus Point	6dB Width	Peak Amplitude (dB)
Uniform Excitation: Rocks	X=80, Y=0	N/A	−12.88 dB
Time-Delay: Rocks	X=80, Y=0	19.8 cm	−12.1 dB
Time-Reversal: Rocks	X=80, Y=0	5.3 cm	−3.16 dB
Uniform Excitation: Cylinders	X=80, Y=0	N/A	−19.3 dB
Time-Delay: Cylinders	X=80, Y=0	— [a]	−16.65 dB
Time-Reversal: Cylinders	X=80, Y=0	5.6 cm	−3.87 dB
Uniform Excitation: Rocks	X=100, Y=0	N/A	−19.31 dB
Time-Delay: Rocks	X=100, Y=0	8 cm [b]	−15.23 dB
Time-Reversal: Rocks	X=100, Y=0	6.6 cm	−4.36 dB
Uniform Excitation: Cylinders	X=100, Y=0	N/A	−19.01 dB
Time-Delay: Cylinders	X=100, Y=0	17.5 cm	−16.62 dB
Time-Reversal: Cylinders	X=100, Y=0	6.7 cm	−4.0 dB

Table 4: 6 dB focusing spot width and peak amplitude at the focus spot for 3 types of excitation signal and 2 configurations of scattering objects at 2 different locations. [a]The wave fronts did not focus sufficiently to measure a coherent beamwidth. [b] The actual signal does not have 6 dB of contrast at the focus point. Based on the existing data, the 6 dB width is estimated assuming a Gaussian shape for the focus width.

type of scattering objects [35, 36]. While it is difficult to predict the effect of the scattering object geometry on focusing spot size [37], it is easily observed empirically.

A comparison is made between three experimental configurations. In all three cases, the central barrier is present. In the first experiment, no scattering objects are placed in the peripheral regions. In the second experiment, the rock configuration is used in the peripheral regions. In the third experiment, the cylinders are placed in the peripheral regions.

The experiments are conducted for time-reversal focusing to two different focusing points (X=80,Y=0) and (X=100,Y=0). The maximum amplitude plots (Figures 56, 57) serve as the basis to determine the focus spot size and the maximum amplitude at the focus spot. The spot size is measured as the cross-range width of the 6 dB local maximum at the focus point. As with the maximum amplitude plots, the data is normalized to the energy present in the excitation signals. Table 5 summarizes the results.

While the data does show some variation in spot size and maximum amplitude at the focus point, the variations are small enough to be within the measurement error of the accelerometer array. The primary source of error is the 3.429 cm spacing between array elements. Such spacing means a real amplitude maximum could occur between these measurement points and that an actual spot width could vary by as much as the spacing between two accelerometers. No consistent trends are evident in the data with respect to focusing spot size or maximum amplitude in relation to the focusing location or the type of scattering objects used. The relationship between scattering object geometry and time-reversal focusing will be examined further in Chapter 7.

Experiment	**6dB Width**	**Maximum Amplitude (dB)**
(X=80,Y=0)[Clean]	6 cm	−4.92 dB
(X=80,Y=0)[Rocks]	5.3 cm	−3.16 dB
(X=80,Y=0)[Cylinders]	5.6 cm	−3.87 dB
(X=100,Y=0)[Clean]	5.3 cm	−3.04 dB
(X=100,Y=0)[Rocks]	6.6 cm	−4.36 dB
(X=100,Y=0)[Cylinders]	6.7 cm	−4.0 dB

Table 5: 6dB focusing spot width and maximum amplitude at the focus spot for time-reversal focusing using threee configurations of scattering objects at two different locations.

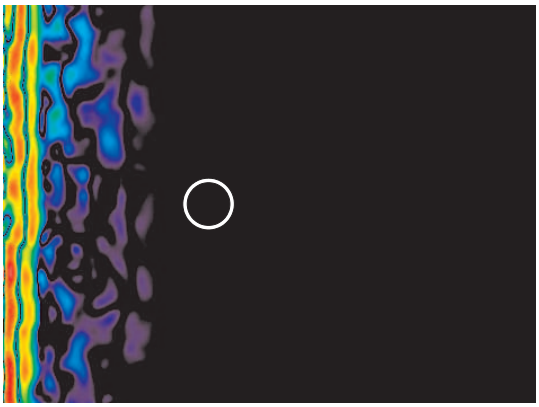

(a) The unperturbed wavefront arrives at the edge of the field of observation.

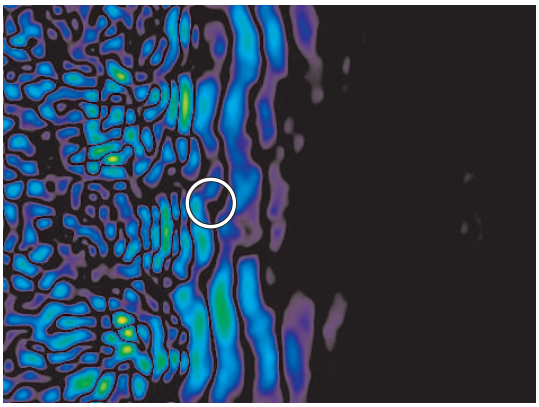

(b) Passing through the ballistic wave barrier, the wavefront is significantly scattered and attenuated.

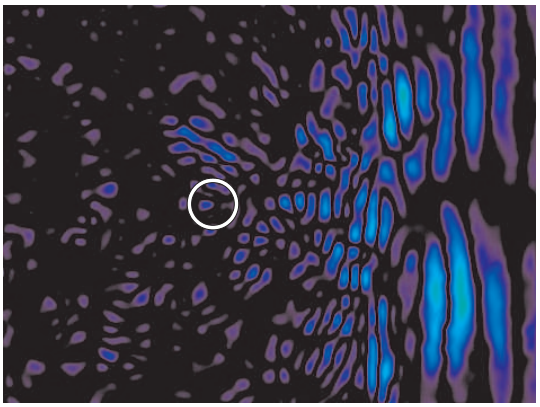

(c) The waves pass the focus point without delivering significant energy to its location.

Figure 45: Time snapshots for the ballistic wave barrier and rocks in the peripheral scattering regions. The source array is excited with uniform excitation using a 900 Hz differentiated Gaussian pulse. The white circle denotes the desired focus location. Images are on a 40 dB pseudo-color scale: 0 dB(white) to −40 dB(black).

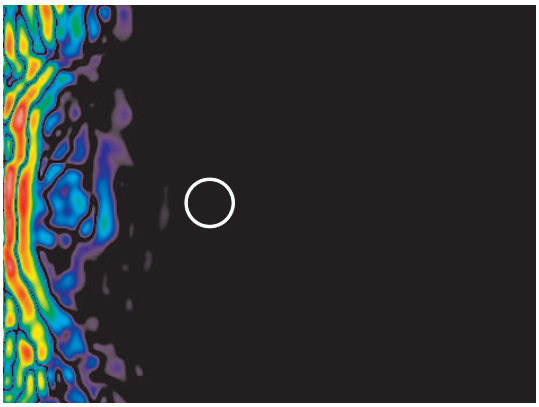

(a) The pre-focused wavefront arrives at the edge of the field of observation.

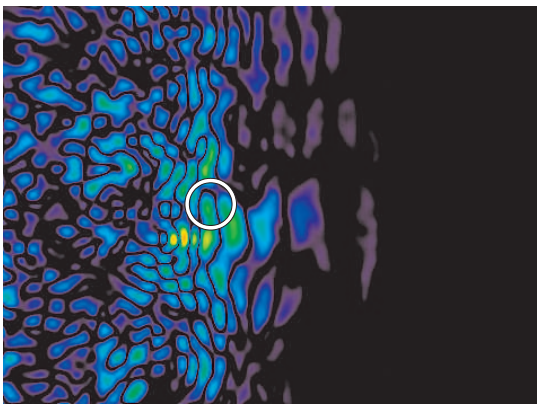

(b) Passing through the ballistic wave barrier, the wavefront is significantly scattered and attenuated. Some focusing occurs, but in the wrong location.

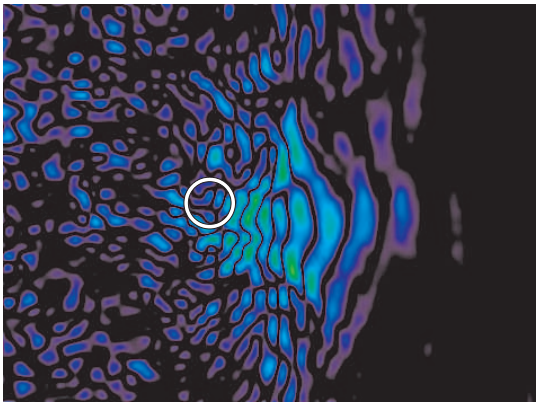

(c) The waves pass the focus point without delivering significant energy to its location.

Figure 46: Time snapshots for the ballistic wave barrier and rocks in the peripheral scattering regions. The source array is excited with time-delayed excitation using a 900 Hz differentiated Gaussian pulse. The white circle denotes the desired focus location. Images are on a 40 dB pseudo-color scale: 0 dB(white) to −40 dB(black).

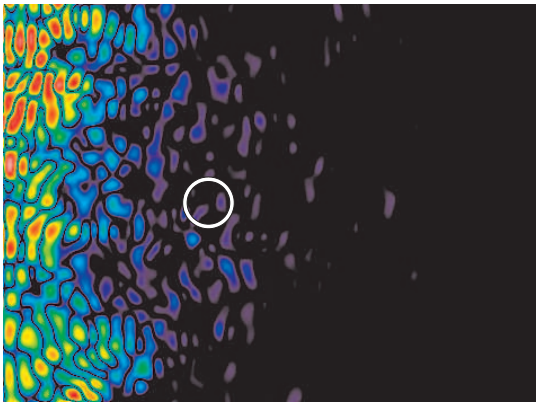

(a) The time-reversal signals arrive at the edge of the field of observation.

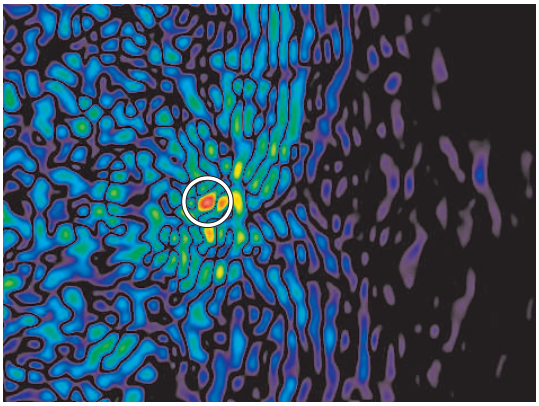

(b) Passing through the ballistic wave barrier, the wavefront focuses tightly on the desired focus location.

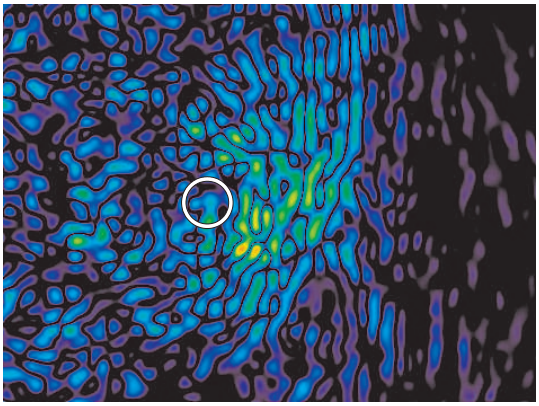

(c) The waves pass the focus point after delivering significant energy to its location.

Figure 47: Time snapshots for the ballistic wave barrier and rocks in the peripheral scattering regions. The source array is excited with time-reversal excitation using a 900 Hz differentiated Gaussian pulse. The white circle denotes the desired focus location. Images are on a 40 dB pseudo-color scale: 0 dB(white) to −40 dB(black).

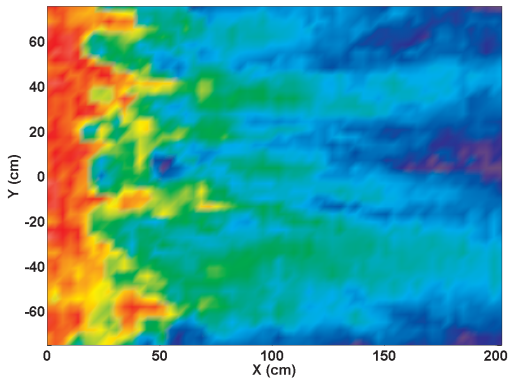

(a) Uniform excitation

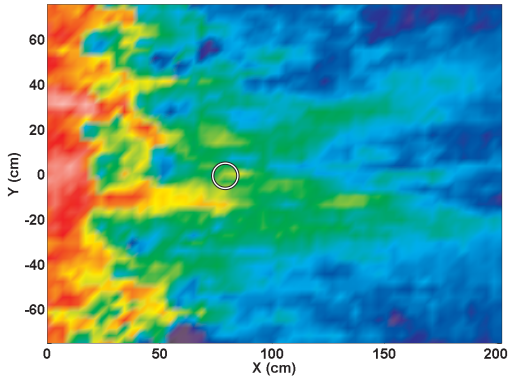

(b) Time-delayed excitation

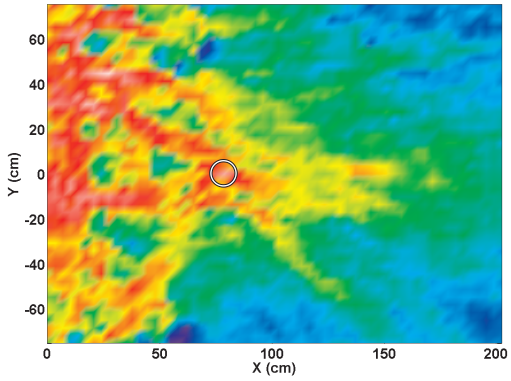

(c) Time-reversed excitation

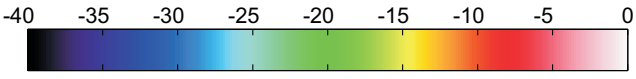

(d) Color - Amplitude Scale

Figure 48: Maximum amplitude plots for the case of a focus point at X=80, Y=0. The central barrier is in place, and rocks are used in the peripheral scattering region. The white circle denotes the desired focus location. Images are on a 40 dB pseudo-color scale: 0 dB(white) to −40 dB(black).

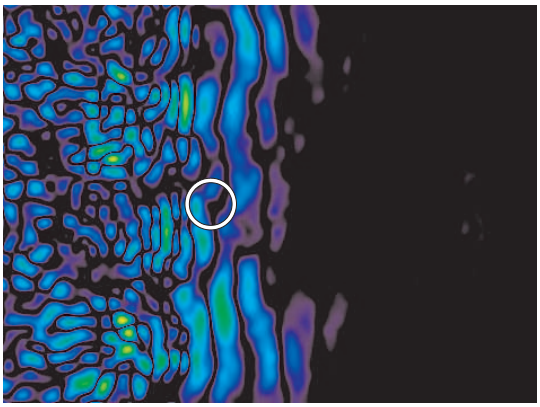

(a) Uniform excitation

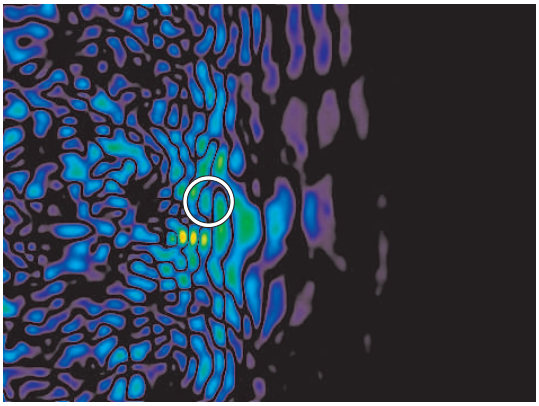

(b) Time-delayed excitation

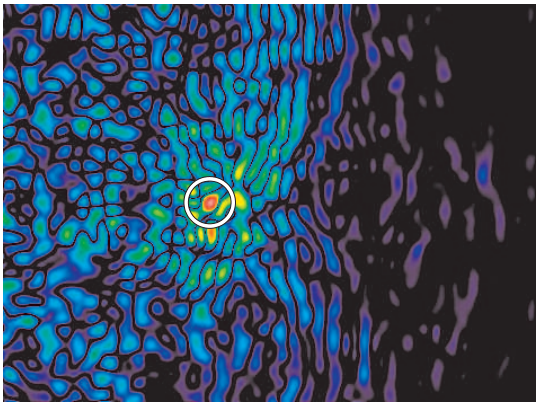

(c) Time-reversed excitation

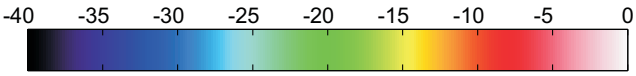

(d) Color - Amplitude Scale

Figure 49: Time shapshots at the focus time for the case of a focus point at X=80, Y=0. The central barrier is in place, and rocks are used in the peripheral scattering region. The white circle denotes the desired focus location. Images are on a 40 dB pseudo-color scale: 0 dB(white) to −40 dB(black).

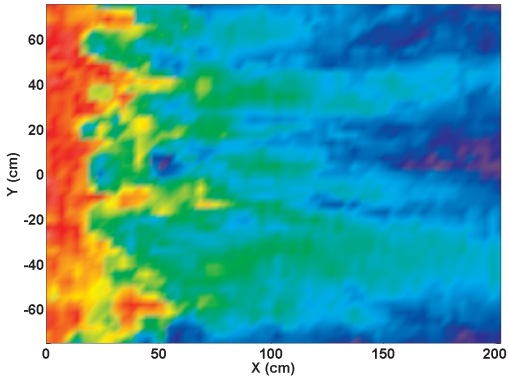

(a) Uniform excitation

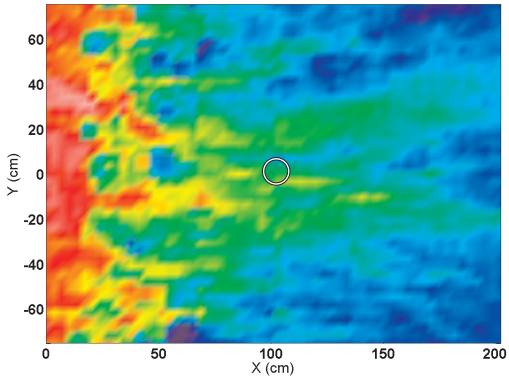

(b) Time-delayed excitation

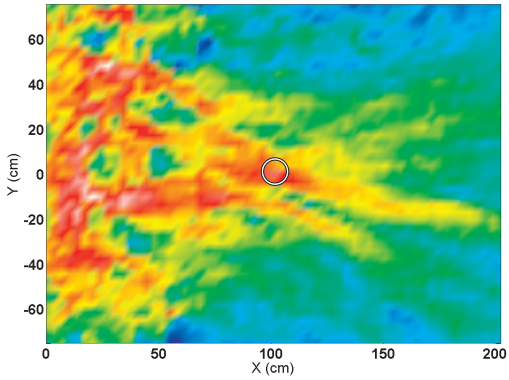

(c) Time-reversed excitation

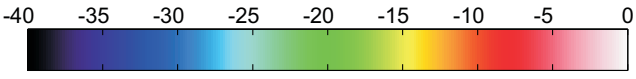

(d) Color - Amplitude Scale

Figure 50: Maximum amplitude plots for the case of a focus point at X=100, Y=0. The central barrier is in place, and rocks are used in the peripheral scattering region. The white circle denotes the desired focus location. Images are on a 40 dB pseudo-color scale: 0 dB(white) to −40 dB(black).

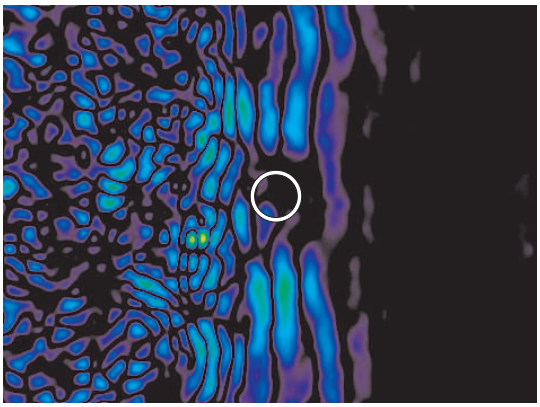

(a) Uniform excitation

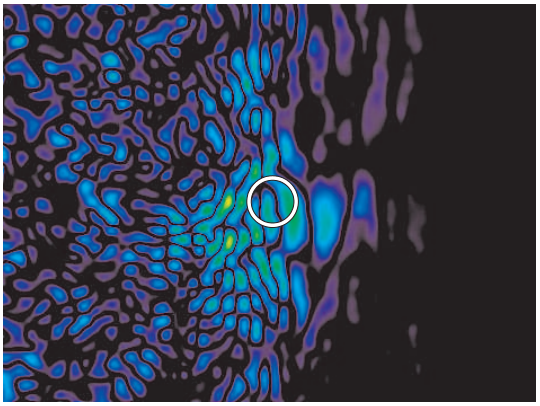

(b) Time-delayed excitation

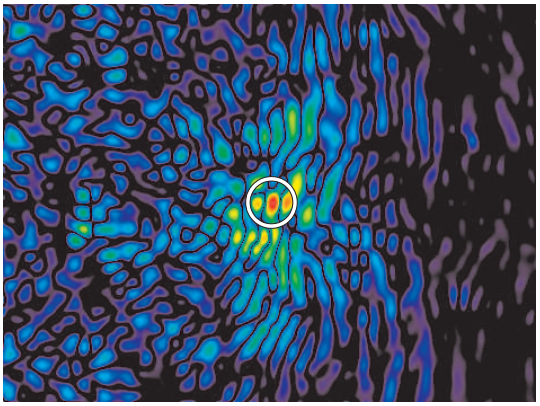

(c) Time-reversed excitation

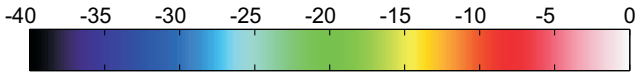

(d) Color - Amplitude Scale

Figure 51: Time shapshots at the focus time for the case of a focus point at X=100, Y=0. The central barrier is in place, and rocks are used in the peripheral scattering region. The white circle denotes the desired focus location. Images are on a 40 dB pseudo-color scale: 0 dB(white) to −40 dB(black).

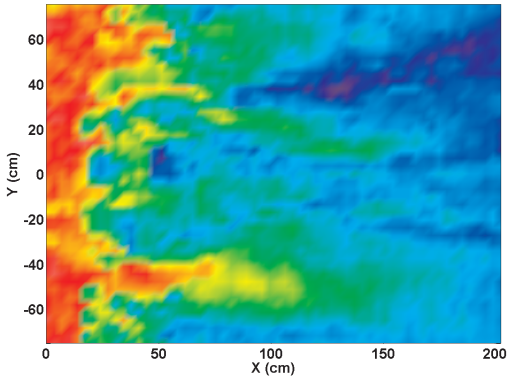

(a) Uniform excitation

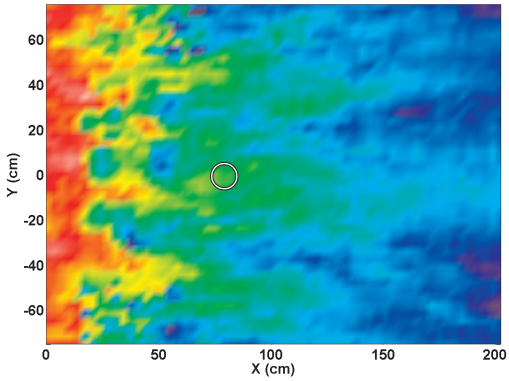

(b) Time-delayed excitation

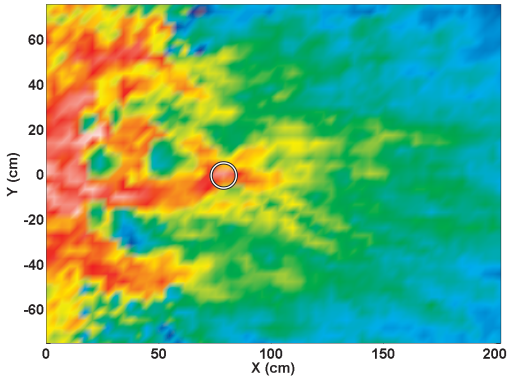

(c) Time-reversed excitation

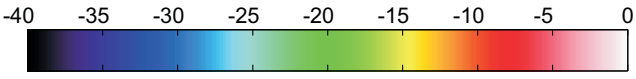

(d) Color - Amplitude Scale

Figure 52: Maximum amplitude plots for the case of a focus point at X=80, Y=0. The central barrier is in place, and concrete cylinders are used in the peripheral scattering region. The white circle denotes the desired focus location. Images are on a 40 dB pseudo-color scale: 0 dB(white) to −40 dB(black).

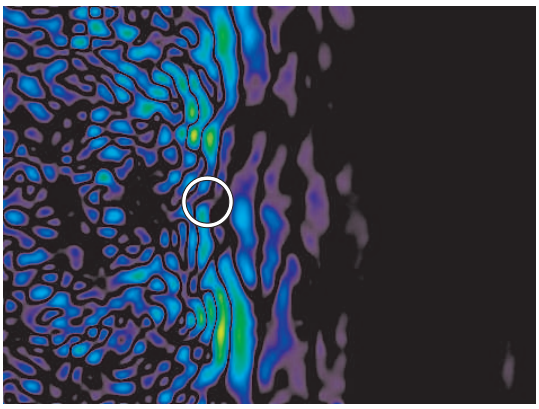

(a) Uniform excitation

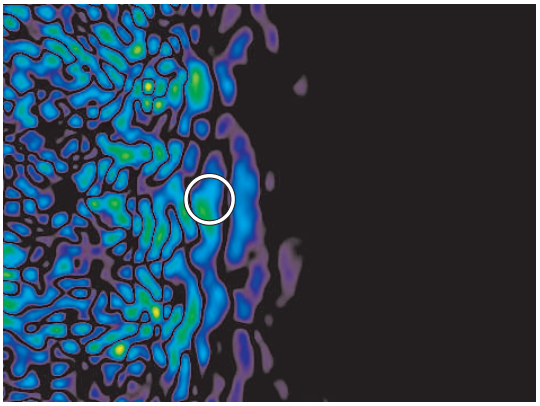

(b) Time-delayed excitation

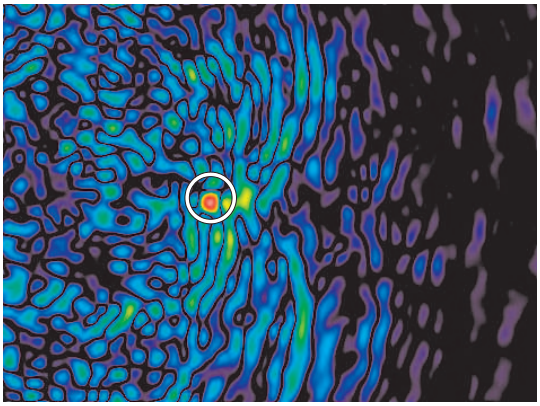

(c) Time-reversed excitation

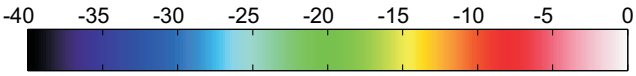

(d) Color - Amplitude Scale

Figure 53: Time shapshots at the focus time for the case of a focus point at X=80, Y=0. The central barrier is in place, and concrete cylinders are used in the peripheral scattering region. The white circle denotes the desired focus location. Images are on a 40 dB pseudo-color scale: 0 dB(white) to −40 dB(black).

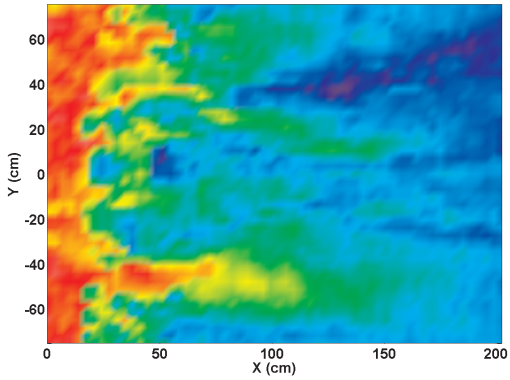

(a) Uniform excitation

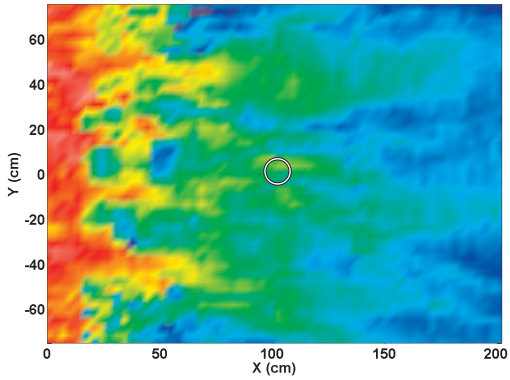

(b) Time-delayed excitation

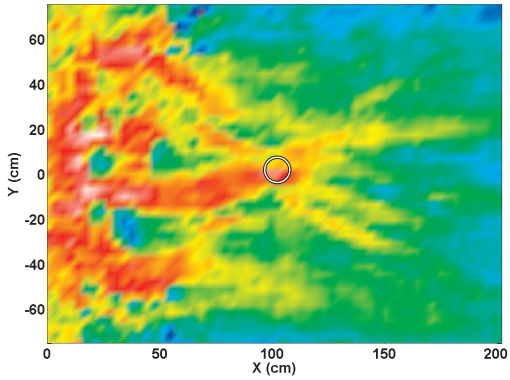

(c) Time-reversed excitation

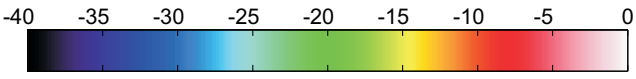

(d) Color - Amplitude Scale

Figure 54: Maximum amplitude plots for the case of a focus point at X=100, Y=0. The central barrier is in place, and concrete cylinders are used in the peripheral scattering region. The white circle denotes the desired focus location. Images are on a 40 dB pseudo-color scale: 0 dB(white) to −40 dB(black).

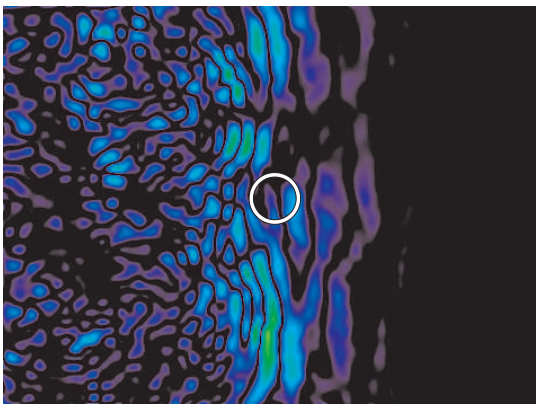

(a) Uniform excitation

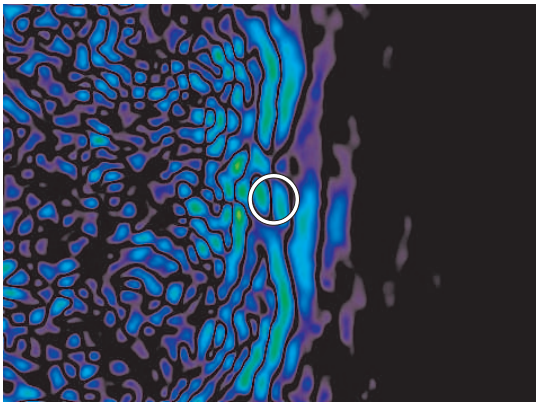

(b) Time-delayed excitation

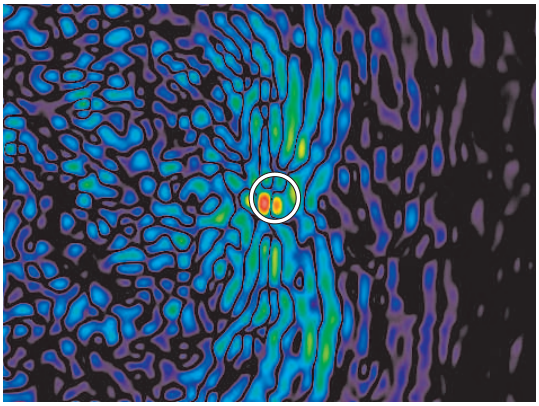

(c) Time-reversed excitation

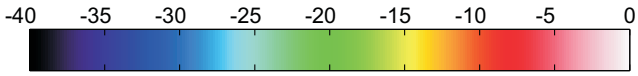

(d) Color - Amplitude Scale

Figure 55: Time shapshots at the focus time for the case of a focus point at X=100, Y=0. The central barrier is in place, and concrete cylinders are used in the peripheral scattering region. The white circle denotes the desired focus location. Images are on a 40 dB pseudo-color scale: 0 dB(white) to −40 dB(black).

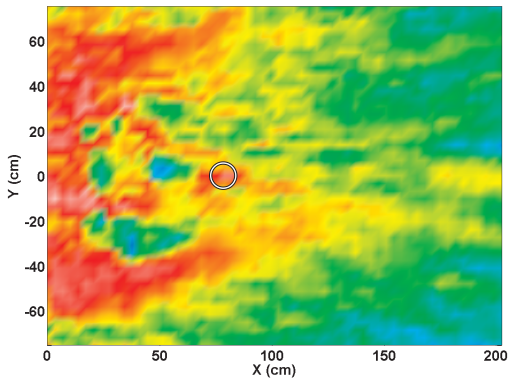

(a) Time reversal: no peripheral scattering

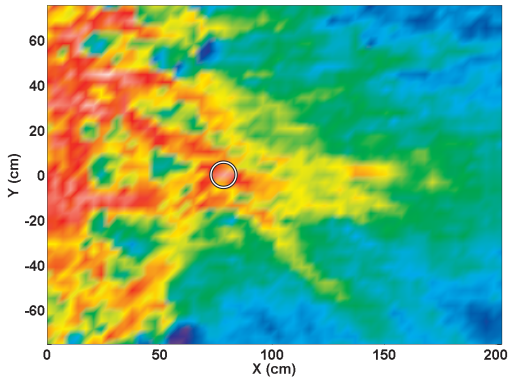

(b) Time reversal: rocks in peripheral regions

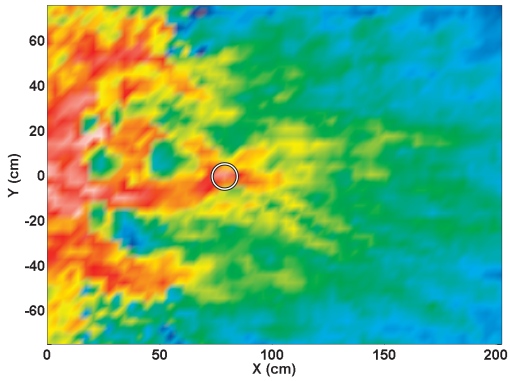

(c) Time reversal: cylinders in peripheral regions

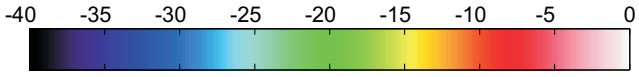

(d) Color - Amplitude Scale

Figure 56: Maximum amplitude plots for the case of a focus point at X=80, Y=0. The central barrier is in place, and the type of scattering objects used in the peripheral scattering region (or absence thereof) is noted in the caption. The white circle denotes the desired focus location. Images are on a 40 dB pseudo-color scale: 0 dB(white) to −40 dB(black).

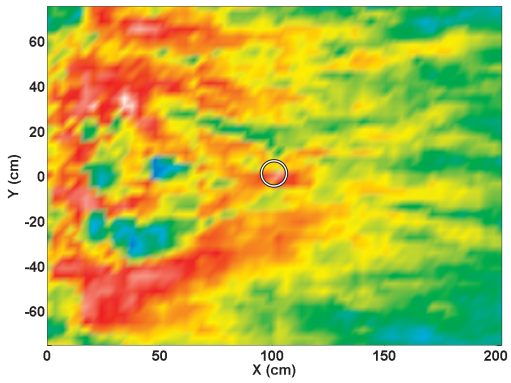

(a) Time reversal: no peripheral scattering

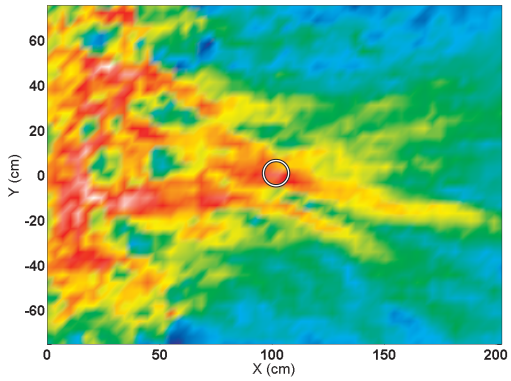

(b) Time reversal: Rocks in peripheral regions

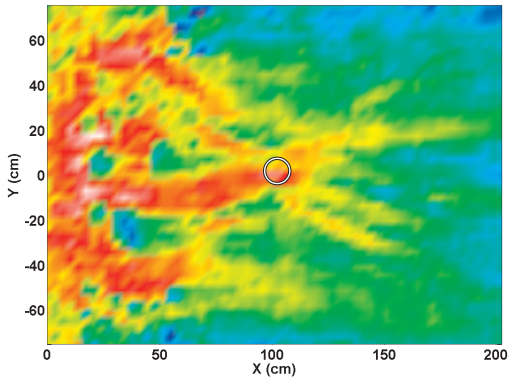

(c) Time reversal: Rocks in peripheral regions

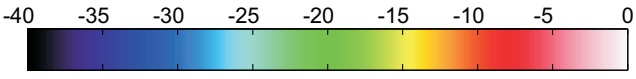

(d) Color - Amplitude Scale

Figure 57: Maximum amplitude plots for the case of a focus point at X=100, Y=0. The central barrier is in place, and the type of scattering objects used in the peripheral scattering region (or absence thereof) is noted in the caption. The white circle denotes the desired focus location. Images are on a 40 dB pseudo-color scale: 0 dB(white) to −40 dB(black).

CHAPTER V

TIME REVERSAL WITH AN ASYMMETRIC SURFACE LAYER

5.1 Motivation

Previous chapters have presented the results of time-reversal focusing for discrete scattering objects, such as fields of cylinders or rocks. The effectiveness of time-reversal focusing has also been evaluated in the presence of a large shadow region created by a central barrier. Another common physical obstacle in buried object detection is the presence of a large asymmetric surface layer such as a roadbed, compacted soil layer, or large vehicle tracks.

In these types of obstacles, and in the experiments presented in this chapter, the surface layer may only extend a shallow depth into the ground. In such a case, the obstacle does not block propagation of a ballistic wave. Depending on the depth and material properties of the surface layer, it may be possible for an incident wave to propagate through or underneath the layer. Depending on the material properties and geometry of the surface layer, a wavefront's direction of propagation could be altered by the surface layer.

Alteration of a wavefront's direction of propagation could detract from the ability to focus energy to a specific location using traditional focusing techniques. In instances where time-delay and uniform excitation have failed to provide high excitation levels, time-reversal focusing has been effective in focusing energy to some desired location. In previous experiments, there have been multiple scattering objects affecting wave propagation through a region. This chapter will evaluate the effectiveness of time-reversal focusing in the presence of a surface layer that changes the direction

of the propagating waves, but does not continually scatter or block the propagating wavefront.

5.2 Experimental Method

5.2.1 Experimental Setup

The setup used in these experiments employs the same experimental facility and setup described in Section 3.3, except that only six elastic wave transducers are used to excite the wave. The reason for this is that the wavefront cannot be as wide as the observation area if we are to effectively alter the propagation path with the surface layer.

A second deviation from the experimental setup described in Section 3.3 is the use of the ground-contacting sensor array described in Section 4.2. The process used to create the time-reversal drive signals is the one described in Section 3.3. Many of the previous experiments examined the effectiveness of time-reversal focusing at location free of any physical target. Here, a TS-50 landmine is buried at the focus location.

5.2.2 Surface Layer

In order for the surface layer to significantly change the direction of a propagating wave, two conditions should exist. First, the propagation speed through the surface layer should be significantly different from the propagation speed in the soil. Second, the surface layer should be asymmetrical or oriented such that propagating waves either enter, or exit the barrier at some oblique angle.

Initial experiments attempted to form a waveguide-type surface layer that would be used to steer the wave away from the focus location. This layer was made by allowing the surface layer of sand in the experimental facility to dry while maintaining high moisture levels in a central channel. This channel was also compacted in an effort to increase the wave propagation efficiency and speed through this layer. This method proved to be largely ineffective because there were minimal changes in the sand cause

by changes in the moisture level.

In order to create a larger difference in wave propagation speeds, a new method created a surface layer using a layer of small stones 6 – 8 cm deep as shown in Figure 59a. The stones were randomly shaped and range in size from 1 cm to 6 cm in all dimensions. The space between the randomly distributed stones was filled with sand and the entire surface layer was made level to the surrounding medium, and with a smooth transition from the surface layer into the sand. The shape of the surface layer was made asymmetrical with respect to the propagation direction of the surface waves as shown in Figure 58.

Additional surface layers were created using 3/4 inch plywood as a surface layer (Figure 59b-d). The plywood layer was created using a wedge-shaped piece of 3/4 inch plywood cut into a 4ft. by 6 ft. wedge. The plywood wedge was tested in three configurations. The next surface layer employed a single sheet plywood wedge that was buried flush to the surface of the sand(Figure 59b), but was not covered by a layer of sand (Figure 60). Another surface layer configuration used two identical 4 ft. by 6 ft. by 3/4 inch plywood wedges. These wedges were buried flush to the surface in an identical configuration as the single-layer setup. The difference was that the new plywood layer was 1.5 inches thick. In a final plywood configuration, two sheets of plywood were buried flush to the surface, but with a thin layer (2 cm) of sand between the two sheets. The sheet of plywood on the surface was level to the surface of the surrounding sand.

5.3 Results: Focusing Through an Asymmetric Surface Layer

A comparison can be made of the performance of the three different excitation types: time-reversal focusing, time-delay focusing and uniform excitation. This examination is performed for four types of asymmetric surface layers. While the majority of the results will be presented using maximum amplitude plots, an examination of time

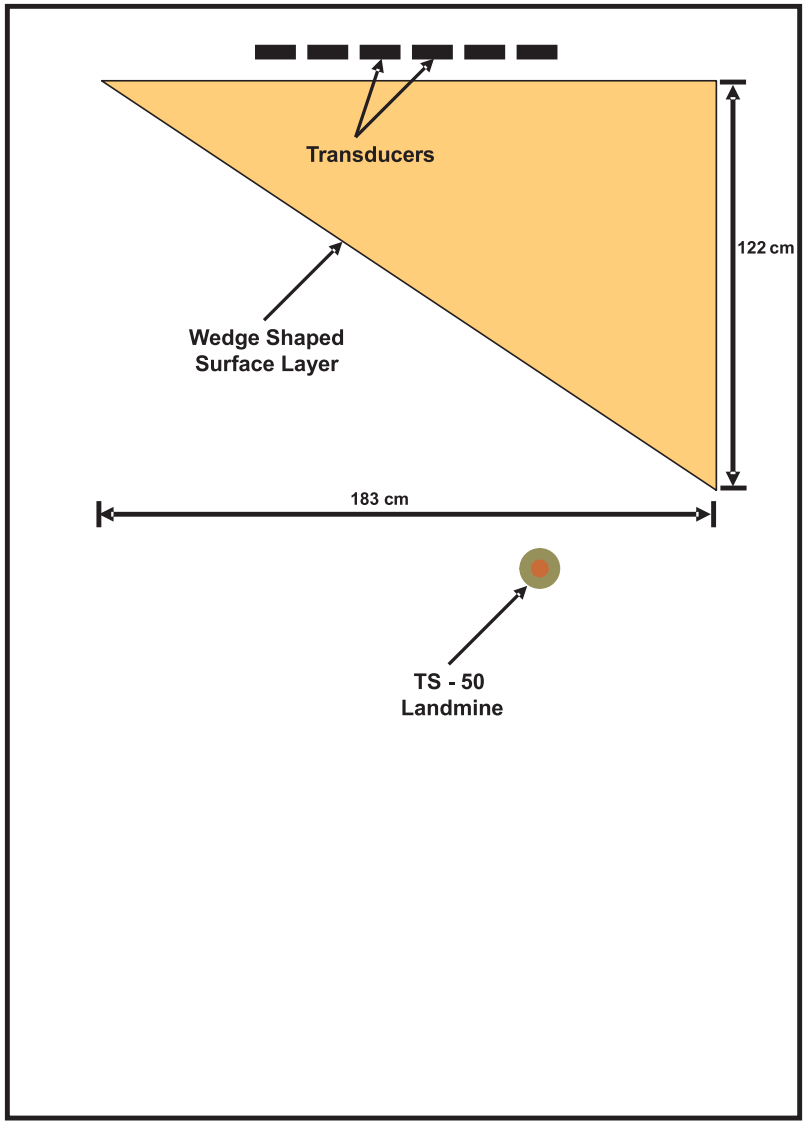

Figure 58: The experimental configuration for experiments using an asymmetric surface layer with a TS - 50 landmine at the focusing point.

snapshots of wave propagation for each type of excitation is useful to visualize the effects of a surface layer on surface wave propagation. In Figures 61 - 63, time snapshots are presented for each of the three excitation methods described. The surface layer for this set of images is the multi-layer plywood and sand surface layer.

The majority of the results from the experiments are presented as plots showing the maximum amplitude of the vertical component of the recorded acceleration over

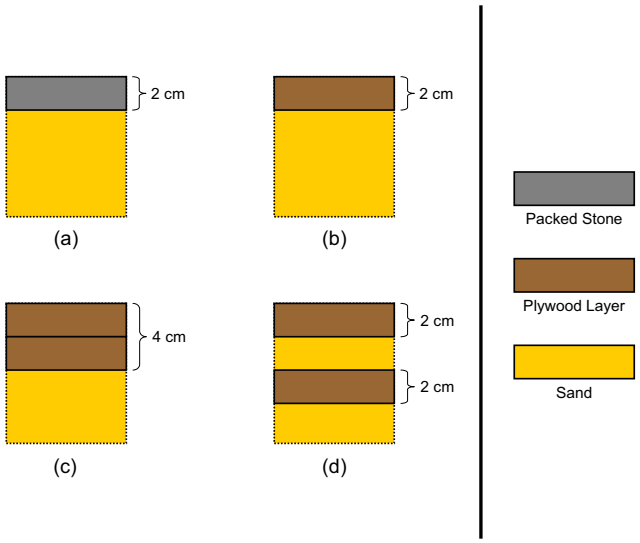

Figure 59: The X-Z plane cross-section of each of the four surface layer configurations used in the experiments: (a) packed stone surface layer, (b) single sheet plywood surface layer, (c) double sheet plywood surface layer, (d) multi-layer plywood and sand surface layer

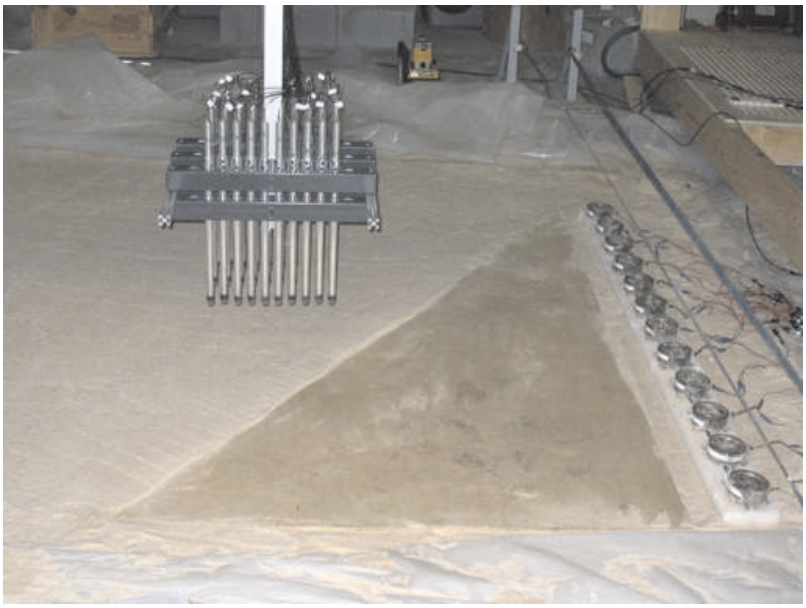

Figure 60: The experimental configuration for experiments using the plywood surface layers. The plywood wedge-shaped surface layer is buried flush with the surface of the sand.

the scan region during the entire time record. These images are formed by creating and displaying the array, $M(x, y)$, as previously described in Equation 52 in Section 4.3. The results are presented as pseudo-color graphs of the magnitude of the vertical component of the particle acceleration at the surface. The pseudo-color scale used in the viewgraphs is a 40 dB logarithmic scale from white (0 dB) to black (−40 dB).

5.3.1 Case A: Packed Stone Surface Layer

The exact propagation speed of the packed stone surface layer is difficult to determine but from empirical observations, the propagation speed appears to be only slightly faster than the surrounding sand medium. For this reason, a large percentage of the propagating energy passes through the surface layer region relatively unaffected by the presence of the surface layer. The propagating wave changes direction very little, and a large pulse reaches the location of the buried landmine using time-delay focusing (Figures 64 and 65). It should still be noted that time-reversal focusing provides a gain of approximately 8 dB over the time-delay focusing case, and provides a local peak excitation level of approximately 15 dB of contrast above the peak excitation level of the background.

5.3.2 Case B: Single Sheet Plywood Surface Layer

Plywood provides a propagation speed which is significantly faster than the surrounding medium (sand). Because of this much higher propagation speed in the plywood, the wedge shape of the plywood layer causes the surface-bound wave to turn. A second wave front travels under the surface layer, coming back to the surface of the sand on the other side of the surface layer. As can be seen in Figure 67, this wave arrives at the landmine location later in time. As its speed is less affected by the plywood wedge on the surface, the change in its propagation direction is almost imperceptible.

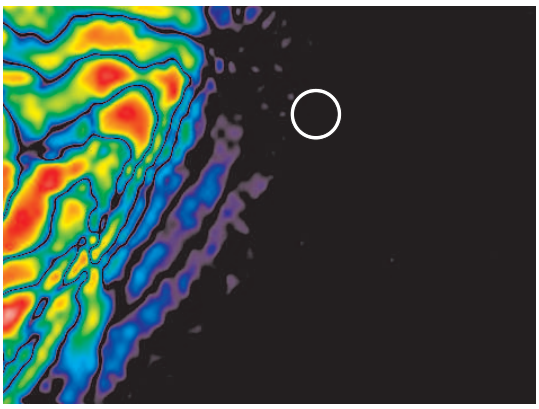

(a) The wavefront exits the surface layer.

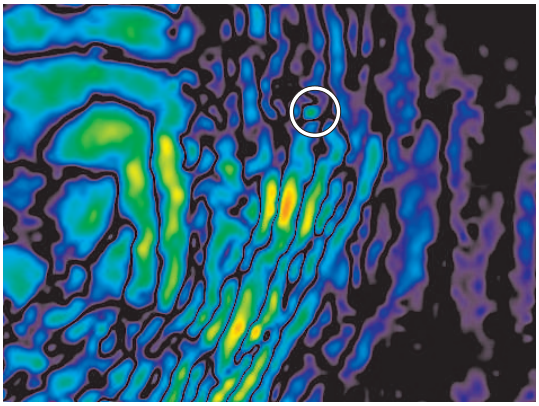

(b) The primary wavefront arrives at the landmine.

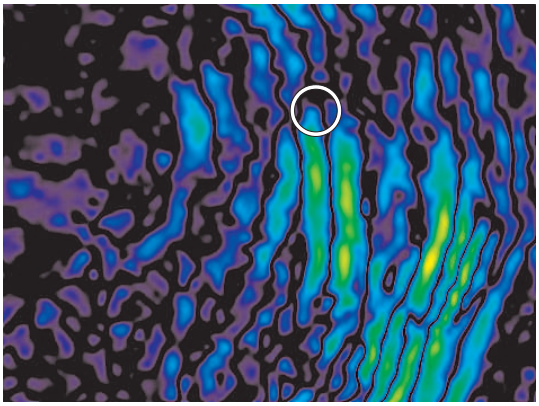

(c) The waves pass the landmine without delivering significant energy to its location.

Figure 61: Time snapshots for the multi-layer plywood and sand surface layer and *uniform excitation* of the source array. The white circle denotes the desired focus location, and the location of a buried TS - 50 land mine. Images are on a 40 dB pseudo-color scale: 0 dB(white) to −40 dB(black).

While the direction change of the second wavefront is very small, the initial wavefront is turned away from the landmine location. This initial wave contains a substantial portion of the excitation energy. Because of this, the maximum amplitude at the landmine location using time-delay focusing is adversely affected. Time-reversal focusing shows a 7 dB improvement in peak excitation amplitude over time-delayed focusing and a peak signal level of approximately 10 dB over the background level (Figure 66).

5.3.3 Case C: Double Sheet Plywood Surface Layer

The performance of the double sheet plywood surface layer is similar to that of the single sheet layer. Because the double sheet plywood layer is twice as thick, more energy should be captured in the surface layer, causing the relative amplitude of the turned wave to be larger in comparison to the second un-turned wave. This is in fact what happens, as can be seen from comparing the uniform excitation cases between the single (Figure 66a) and double (Figure 68a) sheet plywood surface layers.

Even though this additional energy is bound to the surface by increasing the thickness of the surface layer, time-delayed focusing performance improves in this case when compared to the single-sheet surface layer. Time-reversal focusing still shows a 3 dB improvement in peak excitation amplitude over time-delayed focusing and a peak signal level of approximately 8 dB over the background level (Figure 68). For the double sheet plywood surface layer, time-delay focusing provides a better contrast against the background than time-reversal focusing by 2 dB. This variance of 2 dB in focusing height is a small change that could be the result of resonant behavior of the landmine at the focus point, or the interaction of the excited waves with the edge of the surface layer. While sufficient peak amplitude above the background level is desirable, a small difference in peak amplitude contrast with the background level is less significant than the improvement of time-reversal focusing over time-delay

focusing in delivering a high peak excitation to the focus point. Examining Figures 68 and 69, and the results in Table 6, it is evident that time-reversal focusing is more effective than time-delay focusing for this experimental configuration and the metrics stated above.

5.3.4 Case D: Multi-Layer Plywood and Sand Surface Layer

The multi-layer plywood and sand surface performs similarly to the double sheet plywood surface layer except that a significant portion of the energy never reaches the surface. This may be caused by an effect of the layered structure of the wedge-shaped surface layer. Much of the energy is turned away from the landmine location by the wedge shape. This turning effect is apparent in Figure 71b. This causes time-delayed focusing attempts to work poorly.

Time-reversal focusing shows an 8 dB improvement in peak excitation amplitude over time-delayed focusing and a peak signal level of approximately 10 dB over the background level (Figure 70).

5.4 Conclusions

The effectiveness of elastic wave time-reversal focusing was examined in the presence of an asymmetric surface layer. The purpose of the surface layer was to change the propagation direction of the propagating elastic waves in order to steer them away from the location of a buried landmine. The effectiveness of time-reversal focusing in exciting a resonance in the buried landmine was compared to uniform excitation and time-delay focusing techniques. In all cases, time-reversal focusing demonstrated significant improvements over classical focusing techniques in excitation levels at the desired focus point. Table 6 summarizes the results.

Surface Layer Type	**Uniform Excitation**	**Time-Delay Excitation**	**Time-Reversal Excitation**
Packed Stone	-20 dB	-8 dB	0 dB
	Δ8 dB	Δ12 dB	Δ10 dB
Plywood Single Layer	-20 dB	-14 dB	-7 dB
	Δ7 dB	Δ5 dB	Δ10 dB
Plywood Double Layer	-20 dB	-10 dB	-7 dB
	Δ10 dB	Δ10 dB	Δ8 dB
Plywood & Sand Multi-Layer	-28 dB	-18 dB	-10 dB
	Δ5 dB	Δ7 dB	Δ10 dB

Table 6: The peak amplitude (dB) and the background contrast (Δ dB) at the focus point for each excitation type and surface layer configuration.

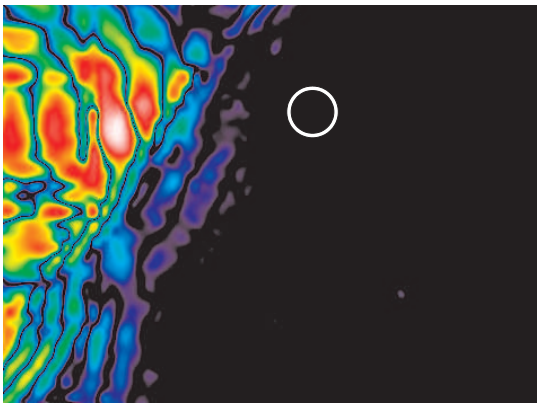

(a) The wavefront exits the surface layer.

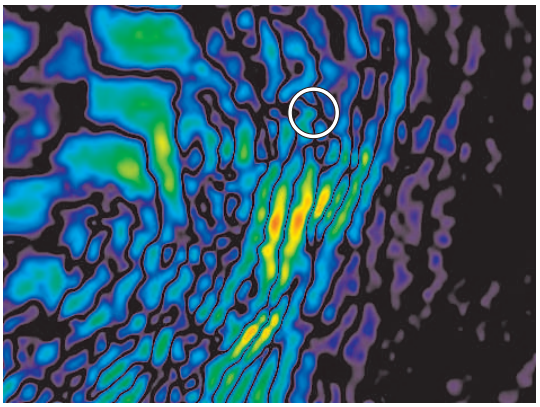

(b) The primary wavefront arrives at the landmine.

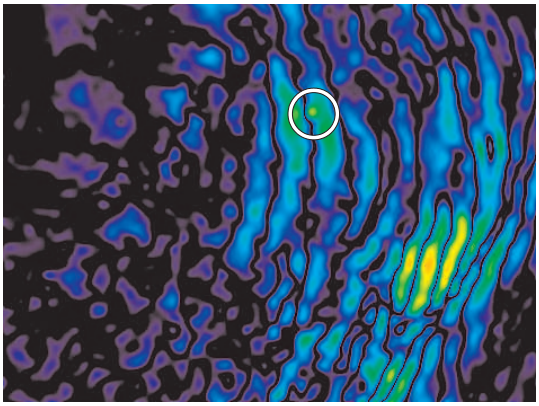

(c) A smaller secondary wavefront that passed *under* the surface layer focus at the location of the landmine.

Figure 62: Time snapshots for the multi-layer plywood and sand surface layer and *time-delay excitation* of the source array. The white circle denotes the desired focus location, and the location of a buried TS - 50 land mine. Images are on a 40 dB pseudo-color scale: 0 dB(white) to −40 dB(black).

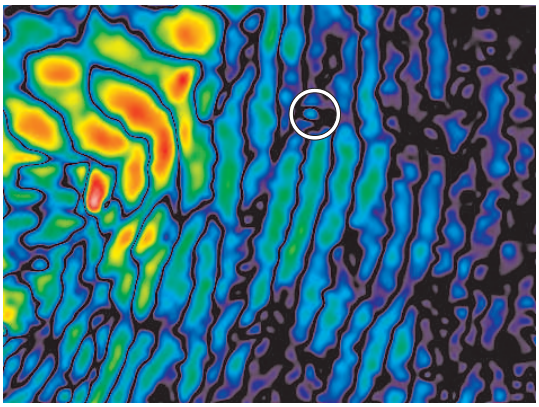

(a) The wavefront exits the surface layer.

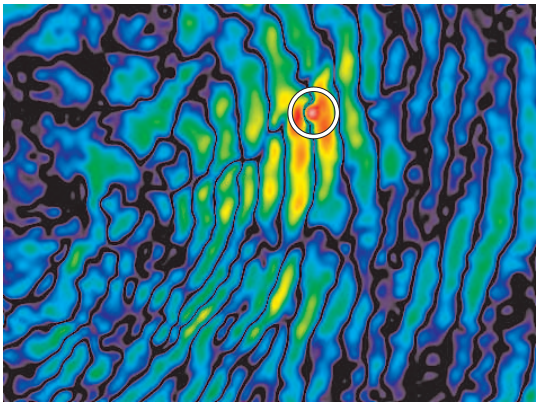

(b) Time-reversal focusing effectively delivers significant energy to the location of the landmine.

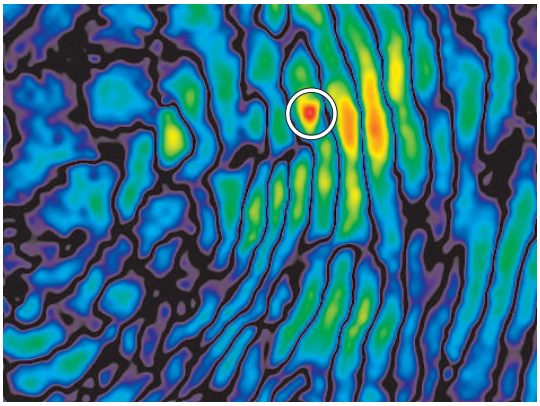

(c) The landmine continues to resonate after the time-reversal focusing wavefront has passed the location of the landmine.

Figure 63: Time snapshots for the multi-layer plywood and sand surface layer and *time-reversal excitation* of the source array. The white circle denotes the desired focus location, and the location of a buried TS - 50 land mine. Images are on a 40 dB pseudo-color scale: 0 dB(white) to −40 dB(black).

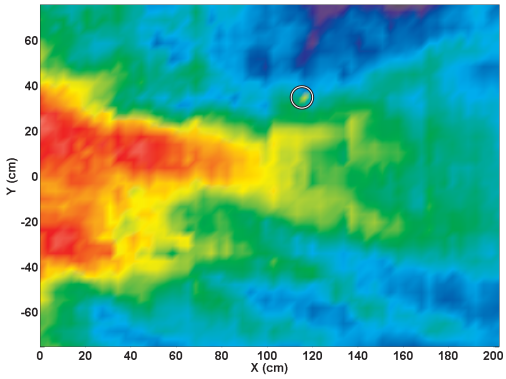

(a) Uniform excitation

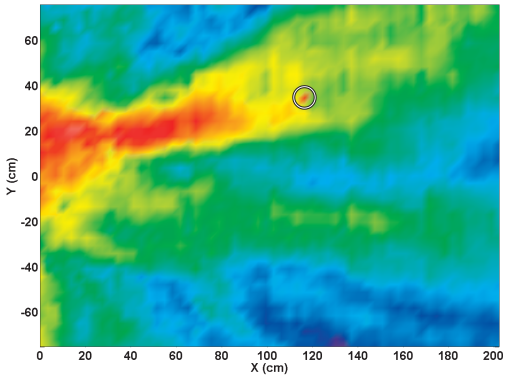

(b) Time-delayed excitation

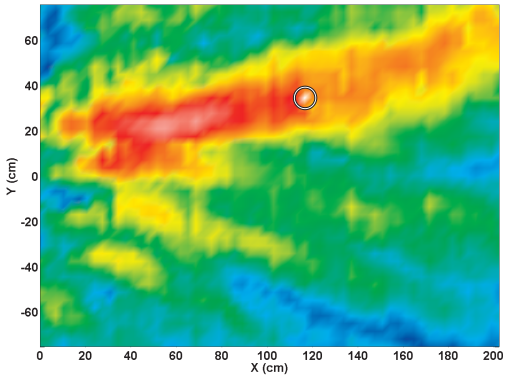

(c) Time-reversed excitation

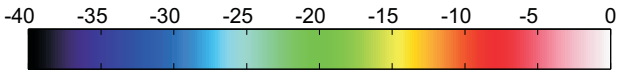

(d) Color - Amplitude Scale

Figure 64: Case A: Maximum amplitude plots for the packed stone surface layer. The circle denotes the desired focus location, and the location of a buried TS - 50 land mine. Images are on a 40 dB pseudo-color scale: 0 dB(white) to −40 dB(black).

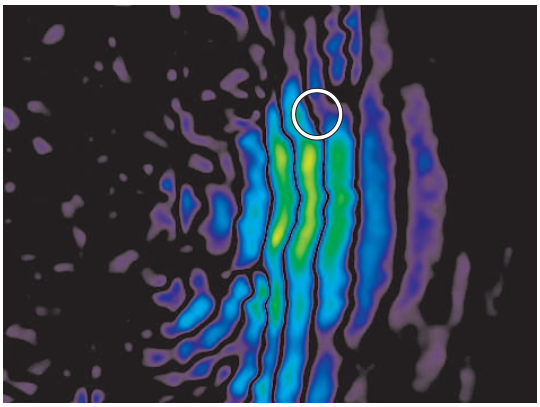

(a) Uniform excitation

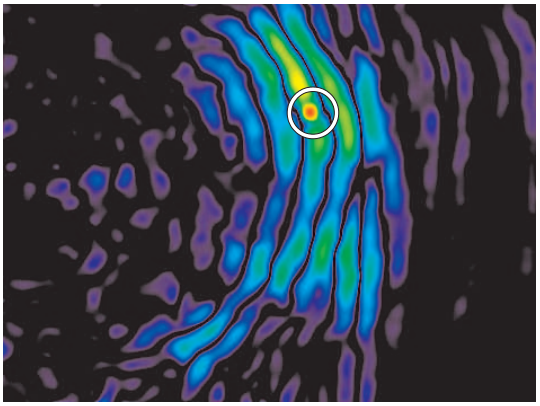

(b) Time-delayed excitation

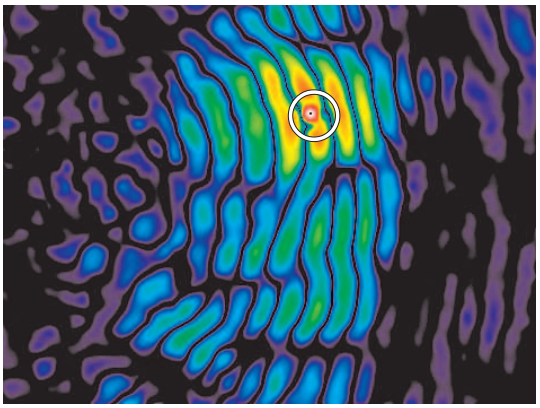

(c) Time-reversed excitation

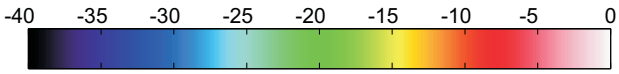

(d) Color - Amplitude Scale

Figure 65: Case A: Time shapshots at the focus time for the packed stone surface layer. The white circle denotes the desired focus location, and the location of a buried TS - 50 land mine. Images are on a 40 dB pseudo-color scale: 0 dB(white) to −40 dB(black).

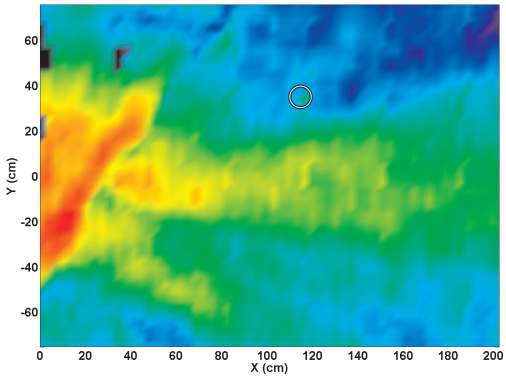

(a) Uniform excitation

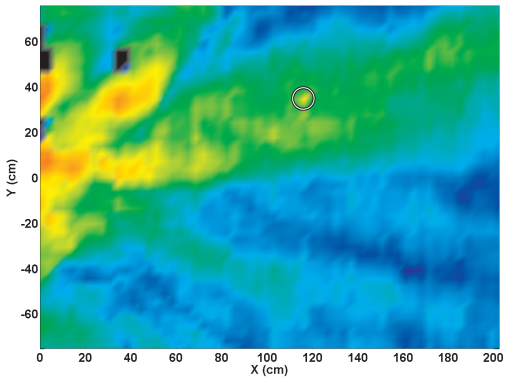

(b) Time-delayed excitation

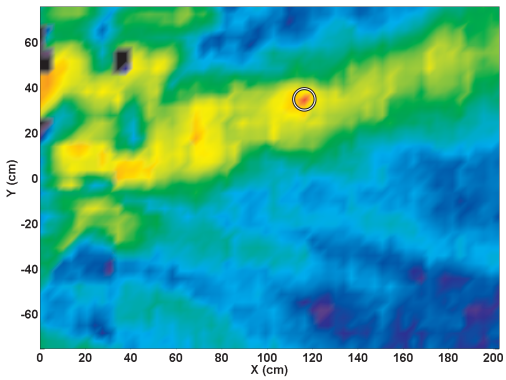

(c) Time-reversed excitation

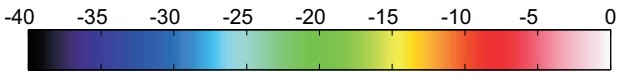

(d) Color - Amplitude Scale

Figure 66: Case B: Maximum amplitude plots for the single sheet plywood surface layer. The circle denotes the desired focus location, and the location of a buried TS - 50 land mine. Images are on a 40 dB pseudo-color scale: 0 dB(white) to −40 dB(black).

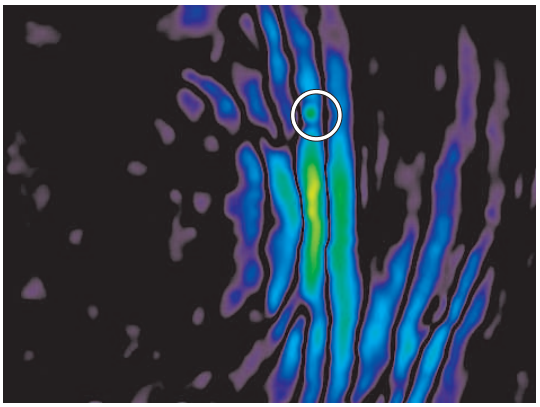

(a) Uniform excitation

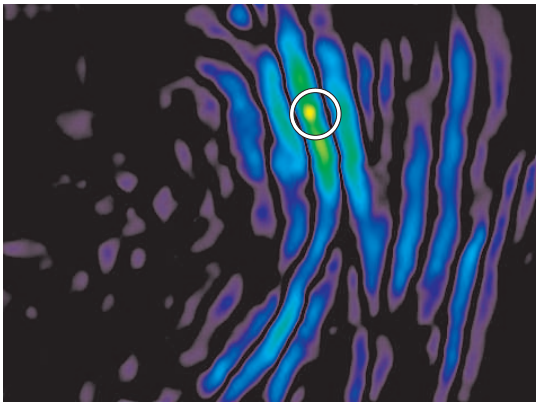

(b) Time-delayed excitation

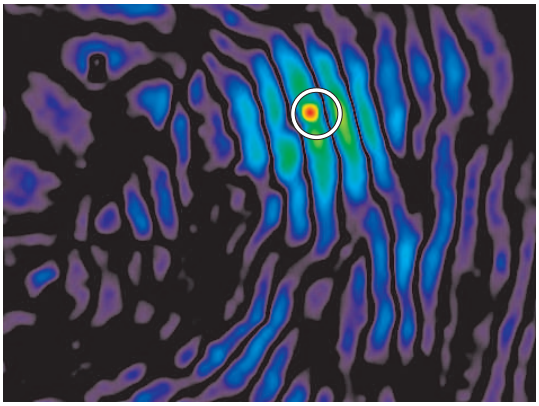

(c) Time-reversed excitation

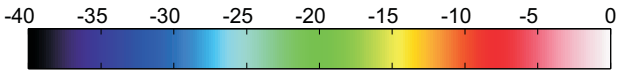

(d) Color - Amplitude Scale

Figure 67: Case B: Time shapshots at the focus time for the single sheet plywood surface layer. The white circle denotes the desired focus location, and the location of a buried TS - 50 land mine. Images are on a 40 dB pseudo-color scale: 0 dB(white) to −40 dB(black).

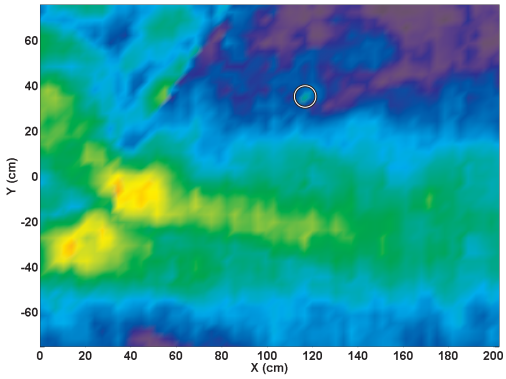

(a) Uniform excitation

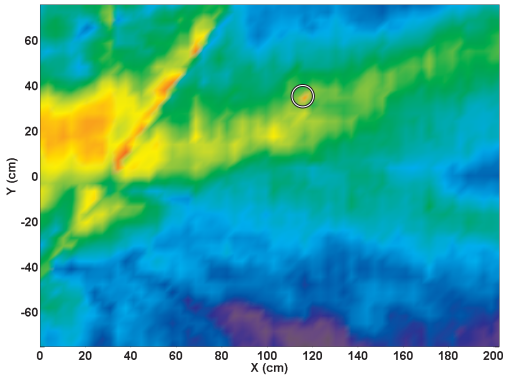

(b) Time-delayed excitation

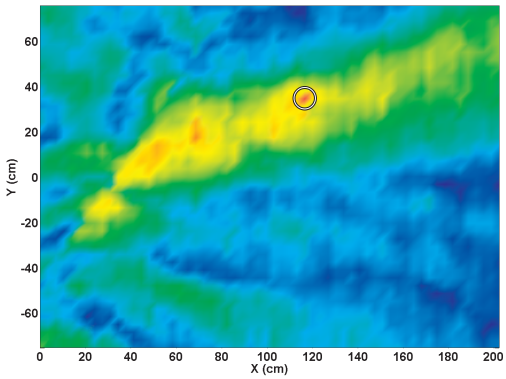

(c) Time-reversed excitation

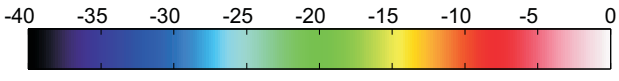

(d) Color - Amplitude Scale

Figure 68: Case C: Maximum amplitude plots for the double sheet plywood surface layer. The circle denotes the desired focus location, and the location of a buried TS - 50 land mine. Images are on a 40 dB pseudo-color scale: 0 dB(white) to −40 dB(black).

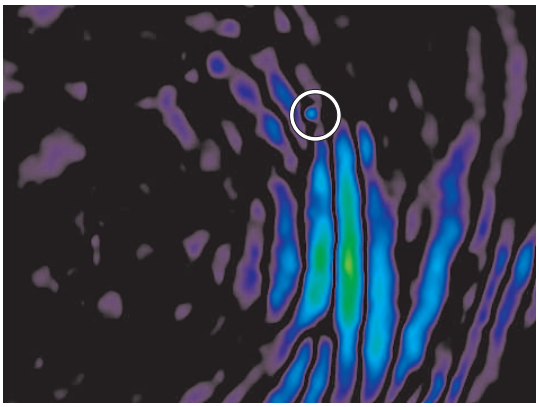

(a) Uniform excitation

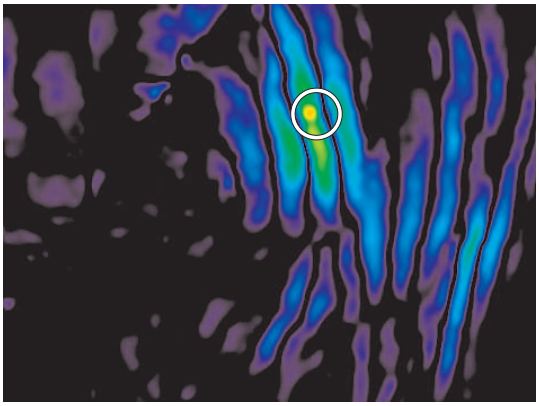

(b) Time-delayed excitation

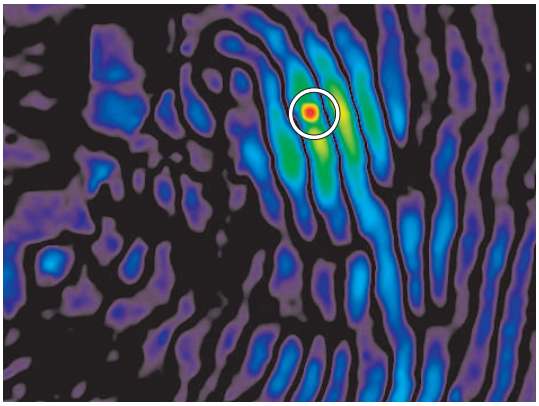

(c) Time-reversed excitation

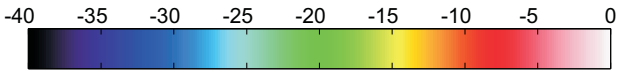

(d) Color - Amplitude Scale

Figure 69: Case C: Time shapshots at the focus time for the double sheet plywood surface layer. The white circle denotes the desired focus location, and the location of a buried TS - 50 land mine. Images are on a 40 dB pseudo-color scale: 0 dB(white) to −40 dB(black).

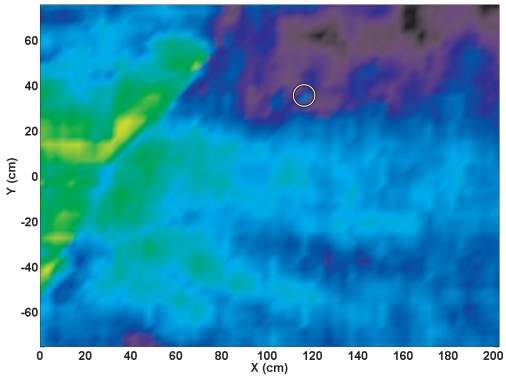

(a) Uniform excitation

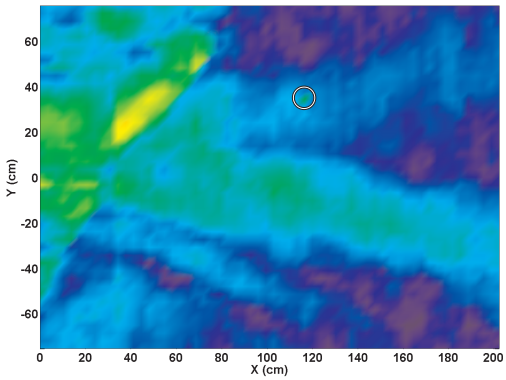

(b) Time-delayed excitation

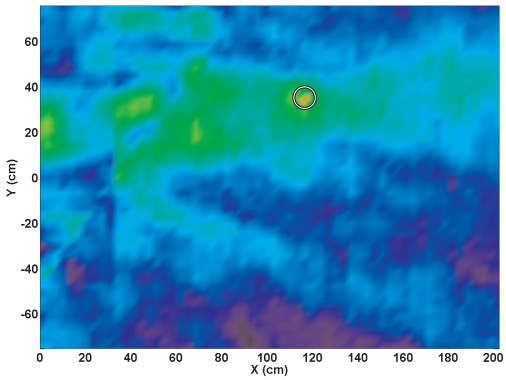

(c) Time-reversed excitation

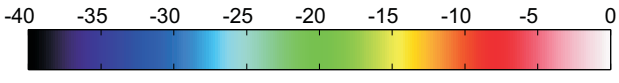

(d) Color - Amplitude Scale

Figure 70: Case D: Maximum amplitude plots for the multi-layer plywood and sand surface layer. The circle denotes the desired focus location, and the location of a buried TS - 50 land mine. Images are on a 40 dB pseudo-color scale: 0 dB(white) to -40 dB(black).

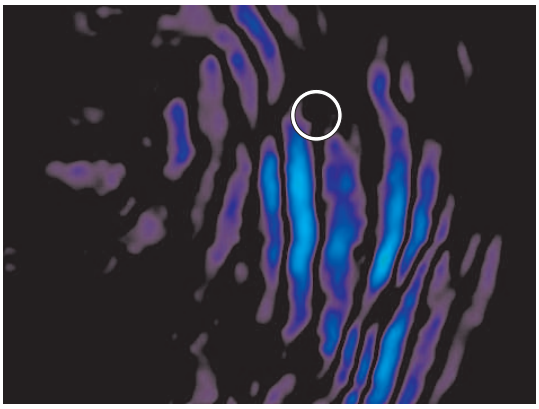

(a) Uniform excitation

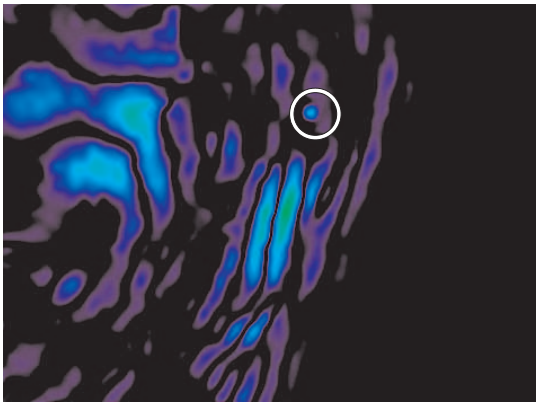

(b) Time-delayed excitation

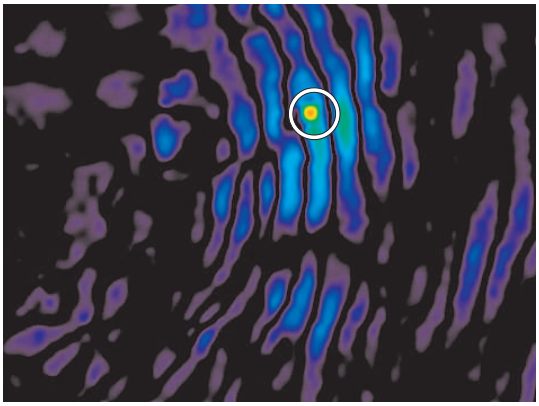

(c) Time-reversed excitation

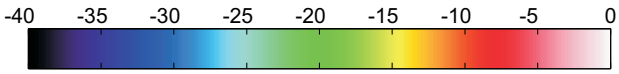

(d) Color - Amplitude Scale

Figure 71: Case D: Time shapshots at the focus time for the multi-layer plywood and sand surface layer. The white circle denotes the desired focus location, and the location of a buried TS - 50 land mine. Images are on a 40 dB pseudo-color scale: 0 dB(white) to −40 dB(black).

CHAPTER VI

TIME-REVERSAL FOCUSING WITH A NON-UNIFORM EXCITATION ARRAY

6.1 Motivation

Time-reversal focusing is commonly performed using transducer array configurations in which the transducers are all regularly spaced across some region. The results from experiments described in previous chapters have demonstrated the effectiveness of time-reversal focusing in these configurations, but time-reversal theory imposes no requirements of regular spacing between transducer array elements. In fact, time-reversal theory indicates that there should be no additional performance loss due to the irregular spacing or location of the sources.

There are many instances, particularly in buried object detection scenarios, when it may be advantageous to employ the use of a non-uniformly spaced array, such as the problem of buried landmine detection. Consider the problem of a mobile buried object detection system such as a landmine detection system. For a traditional configuration, the transducer array must be mounted in some way that maintains the desired spacing between the array elements. Such a configuration may work well in some terrain, but some situations surface debris, trees, large rocks, or other barriers limit the ability to utilize a static array configuration. Non-uniform arrays also provide the ability to overcome "shadow" regions by moving sources such that the straight-line wave propagation path to a focus point is not obscured by any buried clutter or obstacle.

In these cases, a fully configurable excitation array could be employed. Such an array may use individual mobile sensors to create a non-uniform array of transducers

(Figure 72). The purpose of this chapter is to examine the effectiveness of time-reversal focusing in comparison to other excitation methods, when a non-uniform transducer array is used as the excitation source.

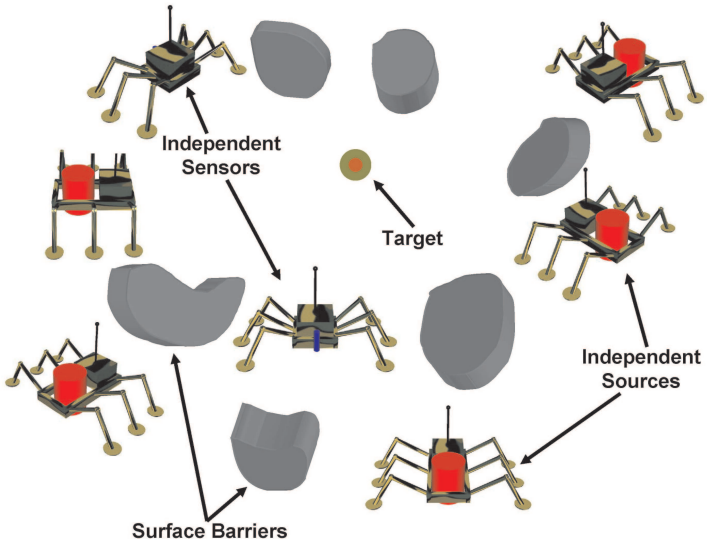

Figure 72: A possible implementation of individual mobile sensors in a non-uniform array. Here, surface obstructions necessitate a transducer array in which each element may be independently be positioned.

6.2 Experimental Method

The experimental setup utilizes the ground-contacting sensor array (Section 4.2.1) to collect data, using the data collection procedure described in Section 4.2, including the previously described averaging method for obtaining the time-reversal drive signals. In order to introduce inhomogeneity into the process, a large central barrier is located in the sand tank, with two smaller regions on each side containing concrete cylinders (Figure 73). The central barrier and concrete cylinders are created using the same procedure described in Section 4.2.3 and Figure 39.

The array of 12 elastic wave transducers is randomly distributed along a region on one end of the sand tank. The transducers are all located outside of the scan region

and the array configuration is asymmetrical in both the X and Y directions on the surface of the sand (Table 7). Two different focus points are chosen, both of which are heavily shadowed by the presence of the central barrier and the cylinder-filled scattering regions (Figure 74).

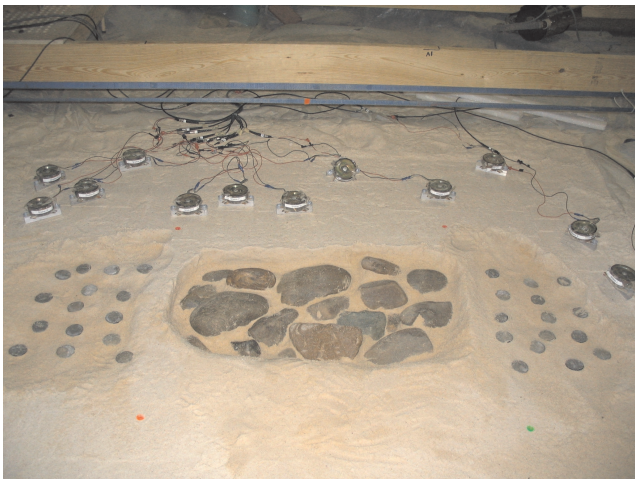

Figure 73: The layout of the non-uniform transducer array with the cylinder-filled peripheral scattering regions and the central ballistic wave barrier. The surface has been excavated to reveal the buried scattering objects.

6.3 Results: Focusing with a Non-Uniform Excitation Array

The results of the experiments are presented as plots showing the maximum amplitude of the vertical component of the recorded acceleration over the scan region during the entire time record and as time snapshots of the vertical component of the particle acceleration. These maximum amplitude images are formed by creating and displaying the array, $M(x, y)$, as previously described in Equation 52 in Section 4.3. For both types of images, the results are presented as pseudo-color graphs of the magnitude of the vertical component of the particle acceleration at the surface. The pseudo-color scale used in the viewgraphs is a 40 dB logarithmic scale from white (0 dB) to black (-40 dB).

Transducer	**X (cm)**	**Y (cm)**
1	−34	−93
2	−11	−92
3	−21.5	−78
4	−45	−64
5	−11	−41
6	−16	−24
7	−11	−4
8	−37	16
9	−17	49
10	−37.5	76
11	12.5	94
12	36.5	104.5

Table 7: The locations of the 12 elastic wave transducers that comprise the non-uniform excitation array. The coordinates are with respect to the scan region in the sand tank.

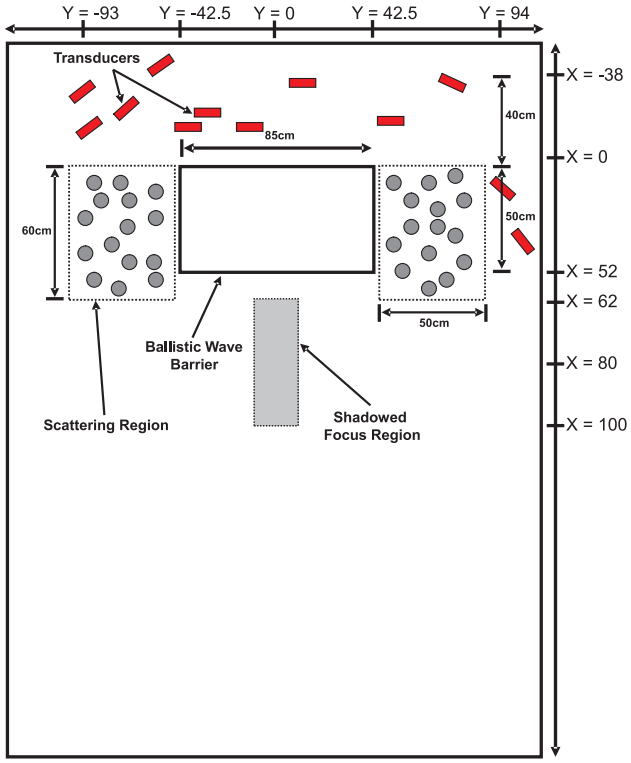

Figure 74: The experimental setup for the non-uniform array of elastic wave transducers. The central wave barrier as well as the peripheral cylinder-filled scattering regions are labelled.

Focusing effectiveness of the non-uniform array is evaluated by comparing the 6 dB cross-range focusing spot size at the focus point for the three types of excitation. The peak excitation level at the focus point is also recorded and compared for each of the focusing types. All the experimental results in this section are normalized by the energy in the excitation signals, and then referenced to the same 40 dB scale so that the results between different experiments may be compared directly.

The experimental results show that for both focus points, time-reversal focusing provides drastically better focusing than time-delay focusing techniques. Peak amplitudes are significantly higher, and the narrower 6 dB widths indicate tighter focusing at the desired spot. When using a non-uniform array, time reversal has a distinct advantage in that it heavily weights the excitation along the least obstructed path.

Focus Point	Excitation Type	6 dB Width (cm)	Peak Amplitude (dB)
X = 80, Y = 0	Uniform	N/A	−21 dB
X = 80, Y = 0	Time-Delay	17.8 cm	−19.5 dB
X = 80, Y = 0	Time-Reversal	10.1 cm	−6.5 dB
X = 100, Y = 0	Uniform	N/A	−21 dB
X = 100, Y = 0	Time-Delay	Unresolvable[a]	−22.53 dB
X = 100, Y = 0	Time-Reversal	8.2 cm	−8.06 dB

Table 8: A comparison of focusing results for three different excitation methods. All results are normalized to the same 0 dB level. The 6 dB cross range spot size and the peak amplitude at the focus spot are both presented.
[a]Energy does arrive at the focus point, but no coherent focus spot is observable, therefore no spot size is computed.

Both the time-snapshot and maximum placement images clearly illustrate this effect. Figures 75 – 79 are time snapshots of early and late time for each excitation type.

These time snapshots offer the opportunity to qualitatively compare wave propagation through the medium. Note the strong wavefront approaching from the top left in the time-reversal cases (Figures 77 and 79) which appears to be taking advantage of the unobstructed path between a source and the focus point. All data is normalized relative to the energy in the excitation signals using the method described in Section 3.3.2, and presented on the same 40 dB scale.

Figures 80 and 81 compare the maximum amplitude for each of the excitation figures. The time snapshots demonstrated the effectiveness of time-reversal focusing in selectively using clutter-minimized paths for delivering energy to the focus point. Figures 80c and 81c further illustrate the impact of this effect on the maximum amplitude excited using time-reversal focusing. The high intensity path from the least obstructed sources (Transducers 11 and 12) provides most of the excitation energy. In contrast, the energy is equally distributed between the sources for time-delay excitation and uniform excitation.

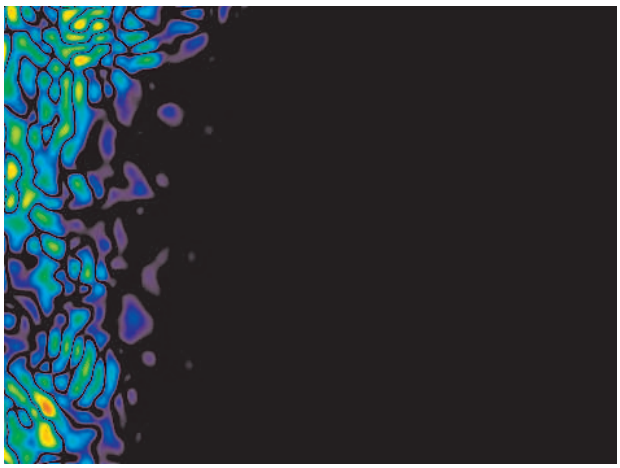

(a) Uniform excitation - early time

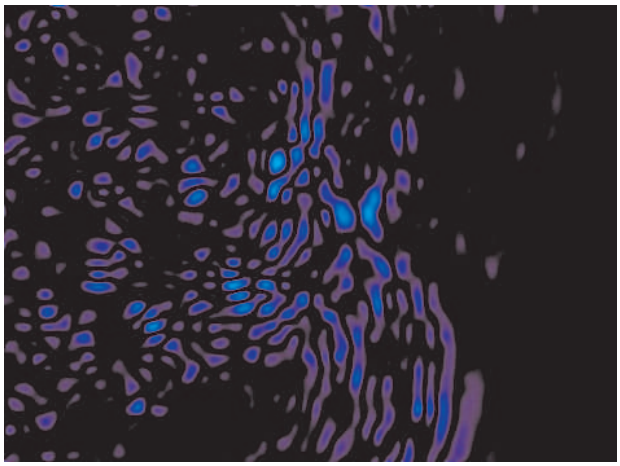

(b) Uniform excitation - late time

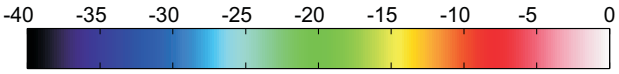

(c) Color - Amplitude Scale

Figure 75: Time snapshots of wave propagation for the non-uniform transducer array using uniform excitation of all the sources. Images are on a 40 dB pseudo-color scale: 0 dB(white) to −40 dB(black).

These experimental results confirm that time-reversal focusing is not adversely affected by the use of a non-uniformly distributed transducer array. Further, time-reversal focusing provides significant advantages over classical focusing techniques when a non-uniform excitation array is used in conjunction with a clutter-filled

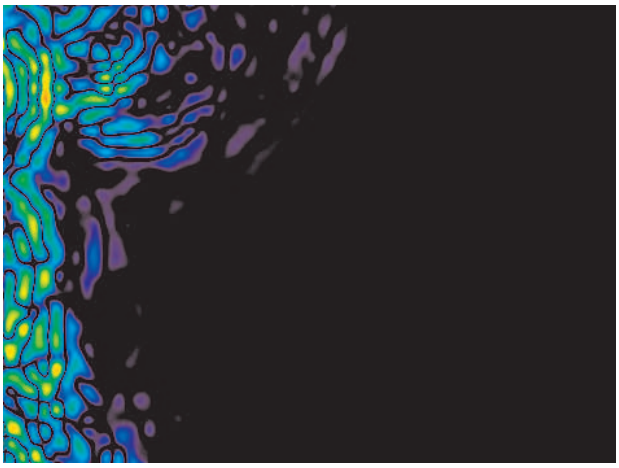

(a) Time-delay excitation - early Time

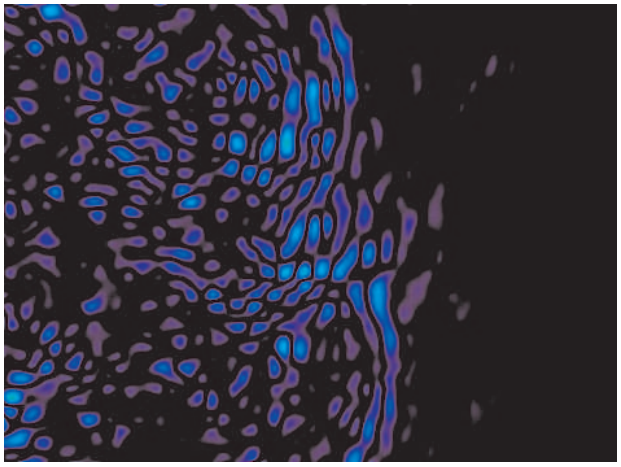

(b) Time-delay excitation - late Time

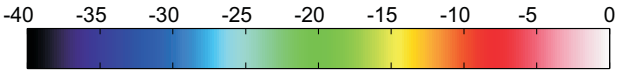

(c) Color - Amplitude Scale

Figure 76: Time snapshots of wave propagation for the non-uniform transducer array using time-delay excitation of all the sources with a focus point of X=80, Y=0. Images are on a 40 dB pseudo-color scale: 0 dB(white) to −40 dB(black).

medium. The improvements are even more pronounced when scattering objects preferentially obstruct the excitation pulse from some of the sources in the array.

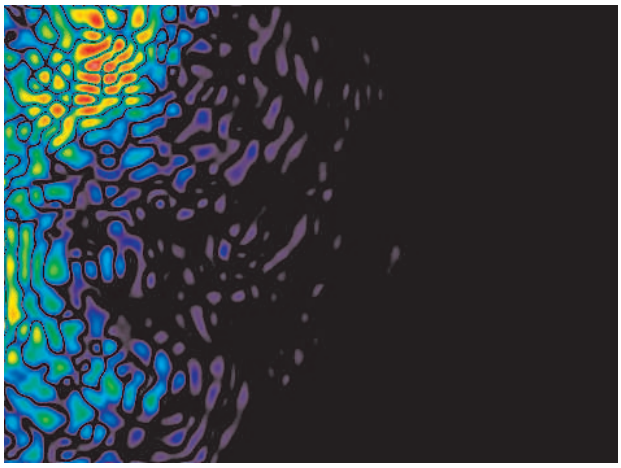

(a) Time-reversal excitation - early time

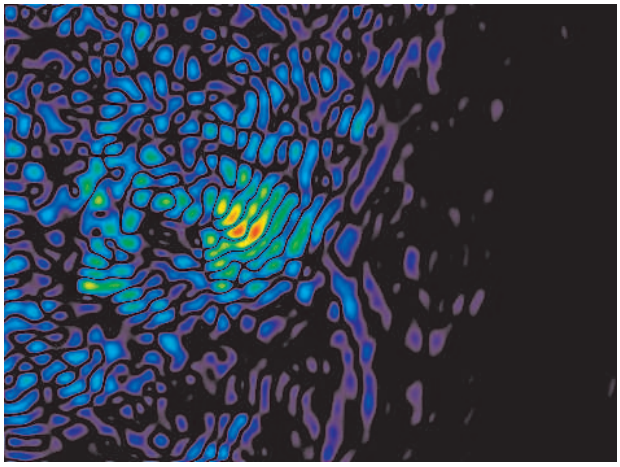

(b) Time-reversal excitation - late time

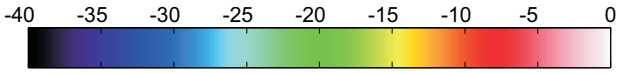

(c) Color - Amplitude Scale

Figure 77: Time snapshots of wave propagation for the non-uniform transducer array using time-reversal excitation of all the sources with a focus point of X=80, Y=0. Images are on a 40 dB pseudo-color scale: 0 dB(white) to −40 dB(black).

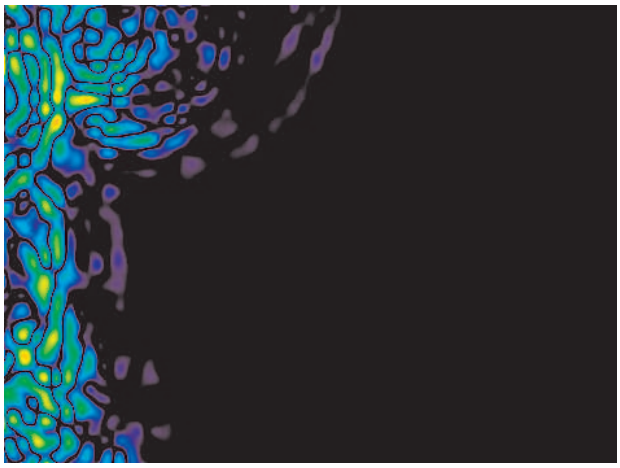

(a) Time-delay excitation - early time

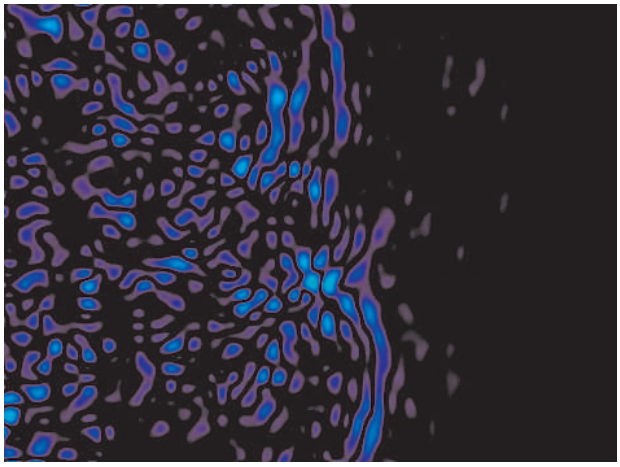

(b) Time-delay excitation - late time

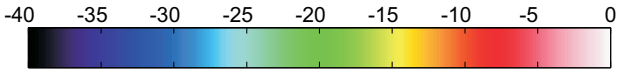

(c) Color - Amplitude Scale

Figure 78: Time snapshots of wave propagation for the non-uniform transducer array using time-delay excitation of all the sources with a focus point of X=100, Y=0. Images are on a 40 dB pseudo-color scale: 0 dB(white) to −40 dB(black).

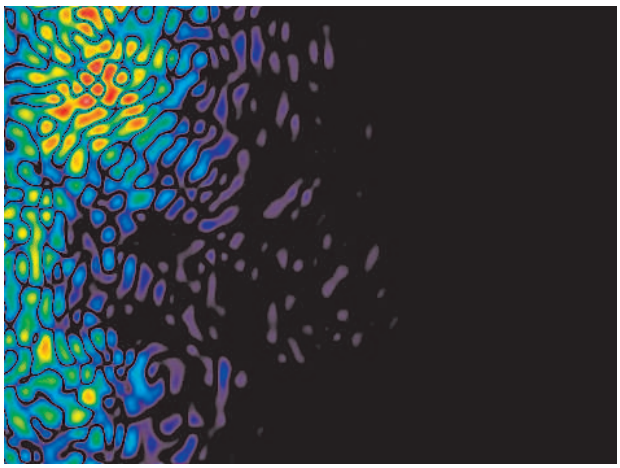

(a) Time-reversal excitation - early time

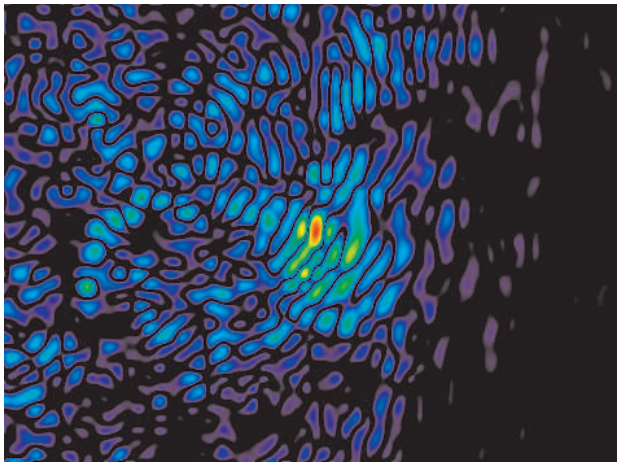

(b) Time-reversal excitation - late time

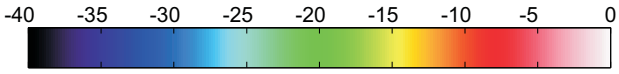

(c) Color - Amplitude Scale

Figure 79: Time snapshots of wave propagation for the non-uniform transducer array using time-reversal excitation of all the sources with a focus point of X=100, Y=0. Images are on a 40 dB pseudo-color scale: 0 dB(white) to −40 dB(black).

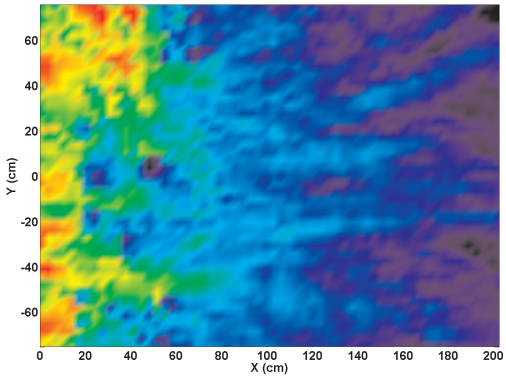

(a) Uniform excitation

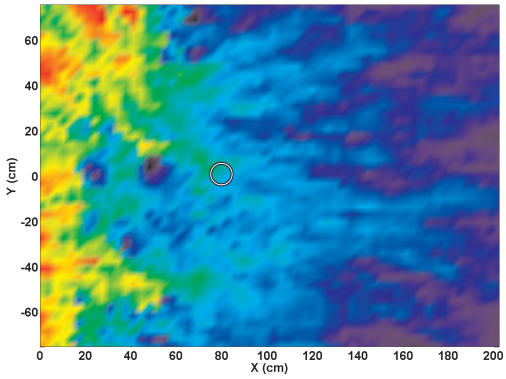

(b) Time-delayed excitation

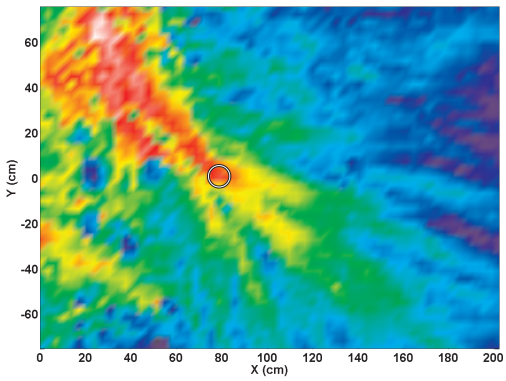

(c) Time-reversed excitation

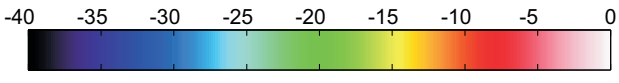

(d) Color - Amplitude Scale

Figure 80: Maximum amplitude plots for the non-uniform transducer array and a desired focus point of X=80, Y=0. The circle denotes the desired focus location, and the location of a buried TS - 50 land mine. Images are on a 40 dB pseudo-color scale: 0 dB(white) to −40 dB(black).

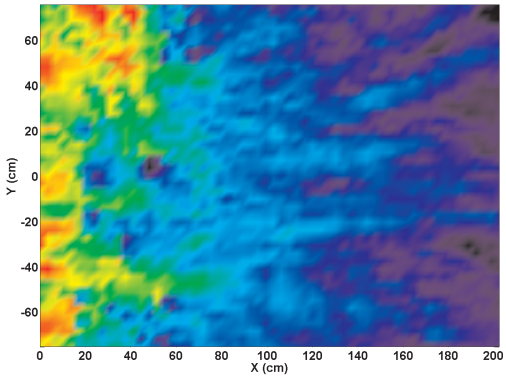

(a) Uniform excitation

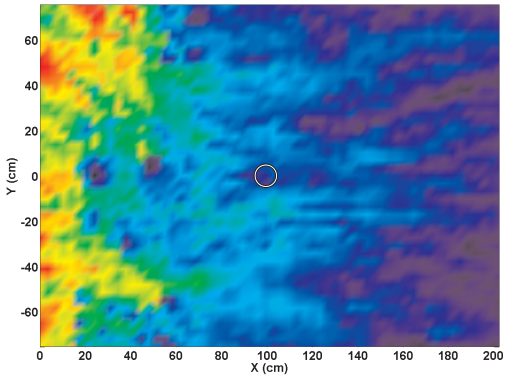

(b) Time-delayed excitation

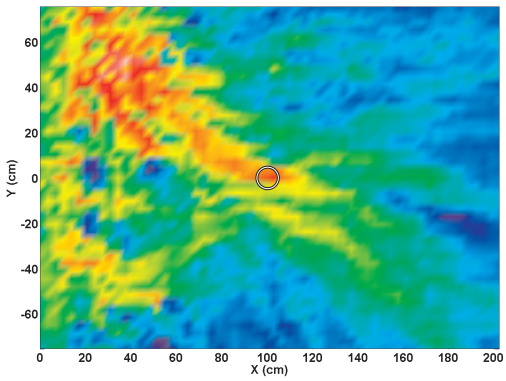

(c) Time-reversed excitation

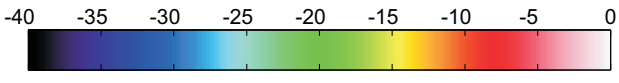

(d) Color - Amplitude Scale

Figure 81: Maximum amplitude plots for the non-uniform transducer array and a desired focus point of X=100, Y=0. The circle denotes the desired focus location, and the location of a buried TS - 50 land mine. Images are on a 40 dB pseudo-color scale: 0 dB(white) to −40 dB(black).

CHAPTER VII

GEOMETRY DEPENDENT SCATTERING EFFECTS

Earlier chapters have examined the performance of time-reversal focusing in a variety of environments. Initial investigations (Section 3.2) examined time-reversal focusing in a clutter-free environment, while Sections 4.3, 5.3 and 6.3 examine time-reversal focusing in the presence of various configurations of scattering objects. The aforementioned experiments demonstrate that as a method to focus energy to a particular location in the presence of numerous scattering objects, time-reversal focusing yields significant improvements in surface displacements at a focus point when compared to other excitation methods.

While the superior performance of time-reversal focusing in comparison to other excitation methods has been demonstrated, the author's previous examinations observed no convincing evidence of the super-resolution phenomenon which has been observed in other examinations of time-reversal focusing [2] and is predicted by theoretical examinations of super-resolution [12, 11]. In this chapter, the performance of time-reversal focusing with respect to focusing resolution will be examined in detail. In particular, the effect of the quantity, shape and size of scattering objects will be investigated.

Investigations of time-reversal focusing in inhomogeneous media have shown that it is an effective method for focusing energy to a desired location. In many cases, scattering objects improve the focusing resolution over situations where no scattering objects are present [2]. An important question to answer is how these focusing effects are altered by the characteristics of the scattering objects: their size, shape, and the field density of the scattering objects. While such an investigation could be performed experimentally, it may be difficult to isolate the effects of any one of these changes

when subject to experimental measurement error, noise, or the non-linearities inherent in the medium (Section 1.2). For this reason, the 3-D finite-difference time-domain model has been chosen as an effective means of investigating these effects.

7.1 Scattering Objects: Effects of Object Field Density

The effect of the field density of scattering objects in the medium is examined first. A numerical space is generated with dimensions similar to the experimental facility. The space is 210 cm × 210 cm × 50 cm deep, and is filled with layered sand that approximates the profile of the characteristics that are seen in the experimental facility. This is the profile that was introduced in Figure 11 in Section 3.2. The scattering objects chosen for this investigation are concrete cylinders that have a 2.5 cm radius and are 30 cm long. Cylinders are chosen as the scattering objects because they are easy to create physically as well in the numerical model. Because of their extended length in comparison to spheres, cylinders tend to more effectively scatter surface waves than similarly sized spherical scattering objects. They are positioned vertically in the sand tank and are randomly distributed in an area of the sand tank that is 70 cm × 150 cm on the surface of the experimental area. Figure 82 shows the model configuration.

In order to examine the effects of increasing the scattering object density on time-reversal focusing, the number of scattering cylinders inside the 70 cm × 150 cm space is varied. All the cylinders are positioned such that they are flush with the surface and each is randomly located in the scattering region, as shown in Figure 82. Time-reversal focusing is performed for each set of cylinders. The results are then normalized by the amount of energy in the time-reversal drive signals, using the normalization method described previously in Section 3.3.2. The first key parameter that is measured is the 6 dB time-reversal focusing cross-range spot size. This spot size is generated from the maximum displacement data, which is computed by the

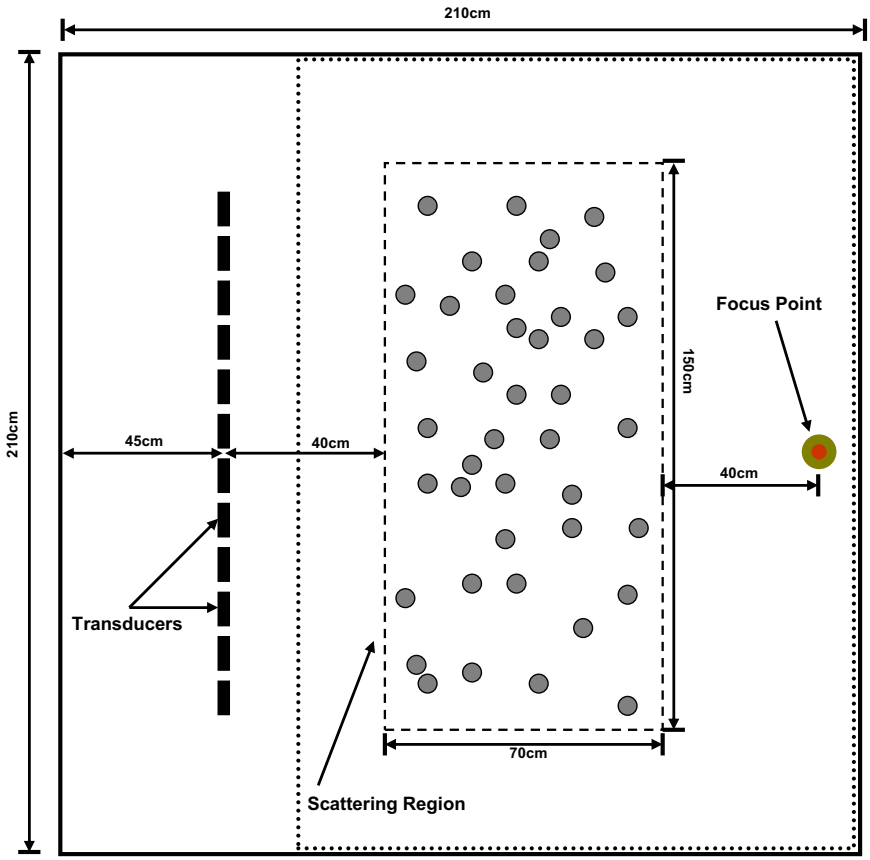

Figure 82: The configuration of the FDTD model for examining the impact of object field density on time-reversal focusing. The entire space is modelled, but results will only be displayed for the portion inside the dotted enclosure.

method also described in Section 3.3.2. The second parameter is the peak amplitude that is recorded at the focus point. In order to generate the data over a wide range of scattering object field densities, several different concentrations of cylinders are used. The results for each number of scattering cylinders are presented in Table 9.

First examining the 6 dB width, a clear trend is evident. As the number of scattering objects increases, the 6 dB width of the focus point decreases. This is not, however, a linear trend. Most of the improvement in focusing resolution is gained with the addition of the first 25 - 50 cylinders. Doubling the number of cylinders

Number of Cylinders	% Area	6 dB Width	Peak Amplitude (dB)
Clean	0 %	11.9 cm	-5.32 dB
25 Cylinders	4.68 %	4.1 cm	-15.02 dB
50 Cylinders	9.35 %	3.4 cm	-19.11 dB
70 Cylinders	13.09 %	3.3 cm	-18.70 dB
100 Cylinders	18.70 %	3.1 cm	-23.93 dB
120 Cylinders	22.44 %	3.0 cm	-26.32 dB

Table 9: Time-reversal focusing results for varying numbers of cylinders in the scattering region. The percentage area in the scattering region covered by cylinders, the 6 dB cross-range (X axis) focus spot size and peak amplitude at the focus point are presented.

from 50 to 100 improves focusing by less than 9 %. This indicates diminishing improvements in focusing resolution as more scattering objects are added. A qualitative visual comparison of spot size is presented by examining the peak displacement in the region immediately surrounding the focus point for each concentration of cylinders. Figure 83 presents this data using peak amplitude pseudo-color images. In these images only a portion of the scan region is shown in order to zoom in on the focus spot. It is worth noting that time-reversal focusing performs poorly when no scattering objects are present. The focus point is poorly resolved and the peak amplitude is not delivered at the true focus point. This is likely the result of using geometrically extended bar-like sources instead of point sources, which add an additional directivity component which could slightly alter the location of the focus point.

From the images in Figure 83, it is evident that additional cylinders cause focusing width to improve, but with diminishing returns. To better quantify this effect, Figure 84 shows both the measured data, and a projected behavior as the number of cylinders continues to increase.

Earlier studies have described the drivers of improved time-reversal focusing resolution [2, 12, 4]. The effect of additional scattering objects is that they increase the mean path length between sources and the focus point. This causes the aperture of the excitation array to appear larger which leads to better focusing resolution. The

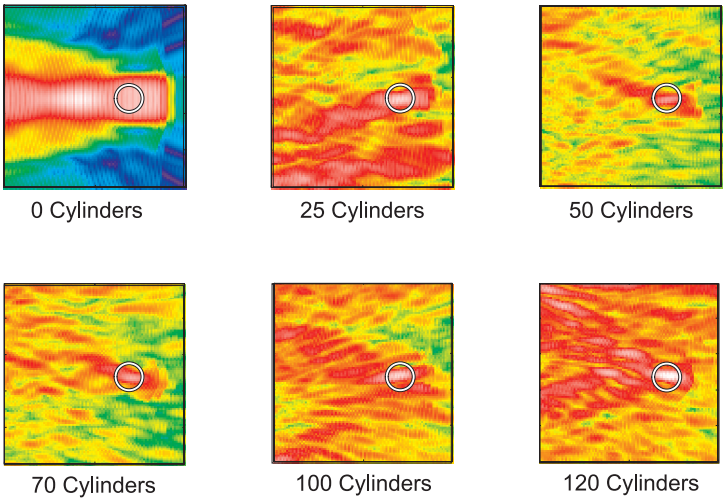

Figure 83: The 6 dB focusing spot size vs. the number of scattering objects is depicted using maximum amplitude plots in the region around the focus point. The results are all self-normalized to maximize dynamic contrast in each image. The focus point is clearly visible in each image and is marked by a circle. All results are on a 40 dB pseudo-color scale from 0 dB (white) to −40 dB (black).

data presented in Figure 84 demonstrates that improvement of the effective aperture approaches a limit as the density of the scattering objects increases.

This result is consistent with our understanding of focusing resolution limits. Multiple scattering effects overcome the aperture limit by widening the effective aperture. Even so, focusing will continue to be limited by the physical diffraction limit which is proportional to smallest wavelength of any frequency component in the excitation signal [5]. It is not possible to calculate an exact diffraction limit for a pulse such as a differentiated Gaussian pulse, but a reasonable assumption is that most significant contributions will be at or below 150% of the center frequency. For the 900 Hz center frequency data presented in this chapter, the approximate diffraction limit is one half wavelength at 1350 Hz. This equates to a diffraction limit of approximately 3.33 cm based on a Rayleigh surface wave propagation speed of 90 m/s.

While there is a diffraction-based limit for spot size, as a general trend, focusing resolution improves as additional scattering is added to the model. This by itself seems to imply that adding scattering enhances the ability of a system to direct energy to a focus point. This is only partially true. A more accurate statement is that scattering enhances the ability of the system to direct to a focus point a higher percentage of the energy *that is available for focusing*. This means that while focusing may be tighter, the absolute peak amplitude at the focus point will decrease as the density of scattering objects is increased. This trend is clearly evident in Figure 85. As the number of cylinders in the scattering region increases, the peak amplitude at the focus point decreases.

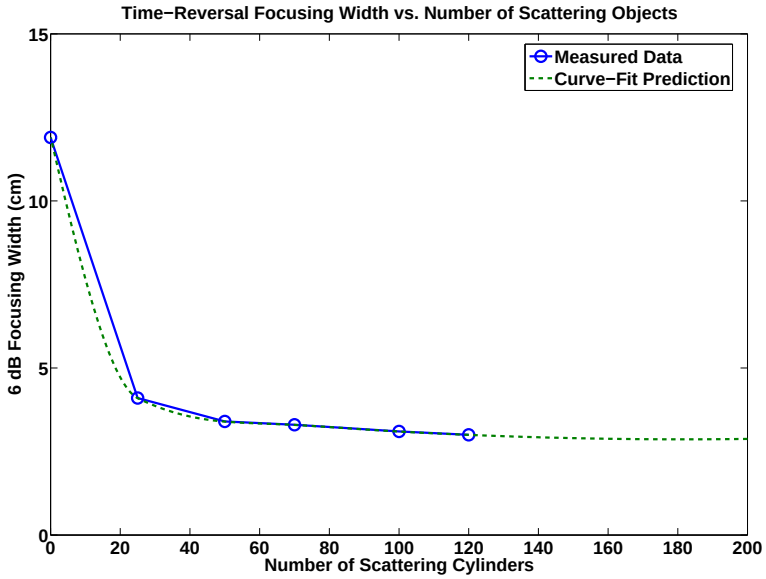

Figure 84: The 6 dB focusing spot size vs. the number of scattering objects.

7.1.1 Scattered Energy

There are two primary reasons for the decreasing trend in available energy for focusing as the scattering object field density increases. First, as the number of scattering objects increases, less energy is able to propagate through the field of scattering objects

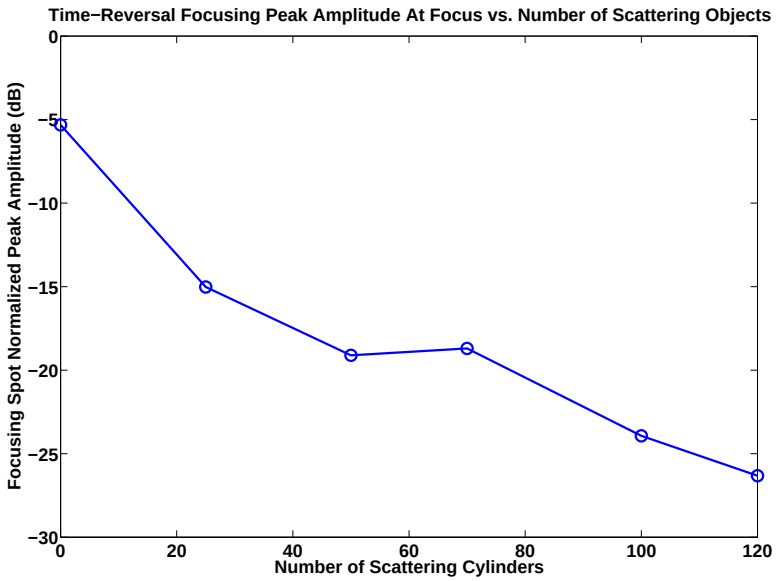

Figure 85: The peak amplitude at the focusing point vs. the number of scattering objects.

from the sources to the focus point. Figure 86 shows the peak displacement amplitude due to the time-reversal focusing signals at any given spot in the different densities of scattering cylinders. It is evident that as the density of scatterers increases, less of the excitation energy reaches the focus point.

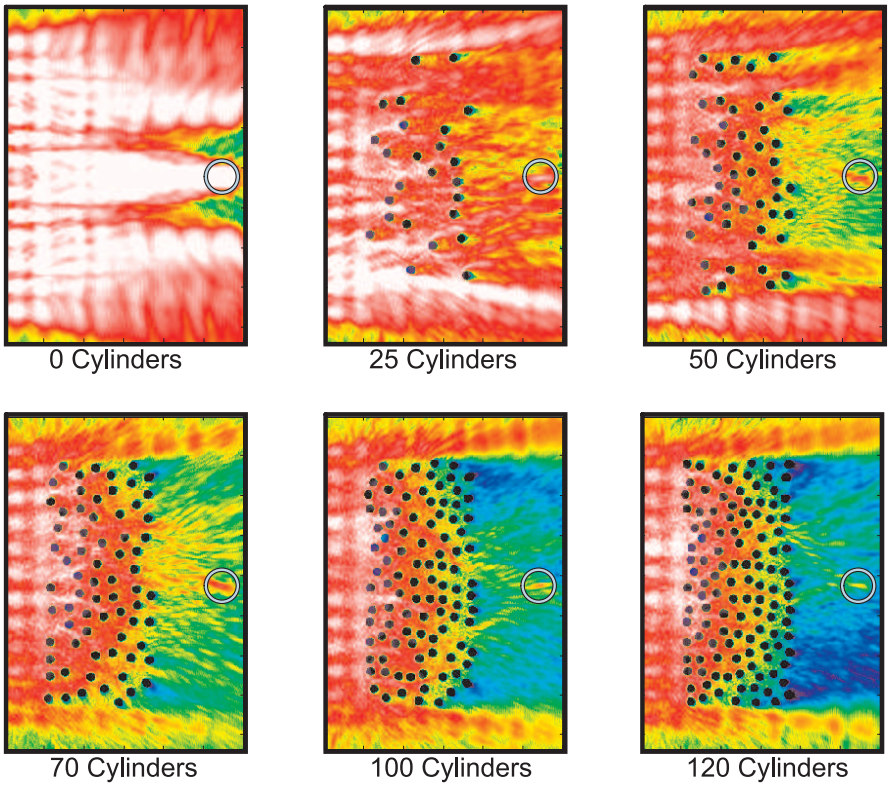

Figure 86: Maximum amplitude plots are presented for time-reversal focusing with different densities of scattering cylinders within the scattering region. The region containing the sources is not displayed. The focus point is denoted by the circle in the center - right of each image. All results are on the same 40 dB pseudo-color scale from 0 dB (white) to −40 dB (black).

This effect is not complex, but it has significant implications when the system is an experiment that includes noise. Time-reversal drive signals have to be generated, which requires an additional pass through the scattering medium. When noise is present, if sufficient scattering is present that the signal or any of its frequency components are near the noise floor, a significant portion of the energy that is injected by the time-reversal focusing signals will be noise. This may have an adverse effect on focusing. The specific effects of noise on focusing will be investigated further in Section 8.3.

7.1.2 Mode Conversion

A second effect that can cause a decrease in the energy available for time-reversal focusing is mode conversion of surface waves. In elastic wave time-reversal focusing, only waves that are present at the surface can be recorded. This is the reason that surface waves, primarily the Rayleigh surface wave, provide the majority of the energy for time-reversal focusing. When scattering objects are present, some of the energy in the Rayleigh wave may be lost to the phenomenon of mode-conversion.

When a propagating Rayleigh wave encounters a scattering object, some of the energy stored in the incident Rayleigh wave is converted into other wave types. These other wave types may not be bound to the surface, causing energy to propagate down into the soil. When large numbers of scatterers are present in the medium, the incident Rayleigh wave will be reflected multiple times. In a lossless environment with no mode conversion, the effect of this scattering would be longer mean path lengths for waves travelling from the source to the receiver, inducing super-resolution. In an elastic medium where mode conversion does occur, each subsequent interaction with a scattering object may cause more energy to be scattered downward. This results in less energy in the Rayleigh wave, and ultimately less energy available for time-reversal focusing.

This effect is best illustrated by the observation of the scattering from a single object. Figure 87 shows a time-snapshot of waves reflected from a single 2.5 cm radius cylinder. These snapshots show the intensity of reflected waves only as the response to a differentiated Gaussian pulse excited by a point source. The snapshot, and particularly the X-Z crossection, demonstrates that a significant portion of the surface wave energy reflected off the cylinder is converted to waves no longer bound to the surface. Figure 87 demonstrates the tendency for some energy to be mode converted, and Figure 85 demonstrates that there is a loss of energy available for time-reversal focusing as the density of scattering object field increases. However,

these observations are not sufficient to conclude that mode conversion has a significant effect on the amount of energy available for time-reversal focusing.

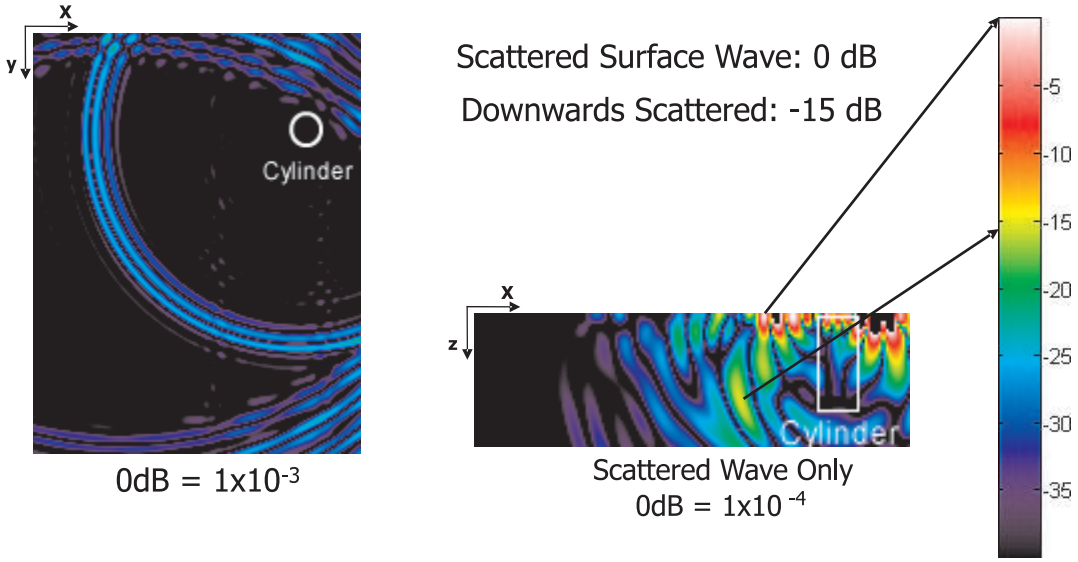

Figure 87: Snapshots of scattering and mode conversion from a single cylinder. The X-Y section is a surface time-snapshot, while the X-Z section is a vertical plane through the solution space. The sources are the 12 bar-foot sources located as depicted in Figure 82.

In order to isolate the effect of mode conversion on the energy available for time-reversal focusing, the Poynting vector energy calculator is used. This feature of the FDTD modelling software is described in detail in Section 2.4.2. The density of a field of scattering objects is varied and the energy that exits the solution space in a region within 20 cm of the surface will be compared to the energy that exits more than 20 cm beneath the surface, and through the bottom. The surface region vs. non-surface region are approximate measures of the energy contained in the surface wave. While this is not an entirely accurate measure of the surface wave energy, it is a reasonable surrogate since the intensity of the surface wave falls off exponentially with depth. A depth of 20 cm represents approximately two Rayleigh wavelengths at the excitation's center frequency of 900 Hz. Figure 88 depicts the regions in which the surface and non-surface wave energy is calculated.

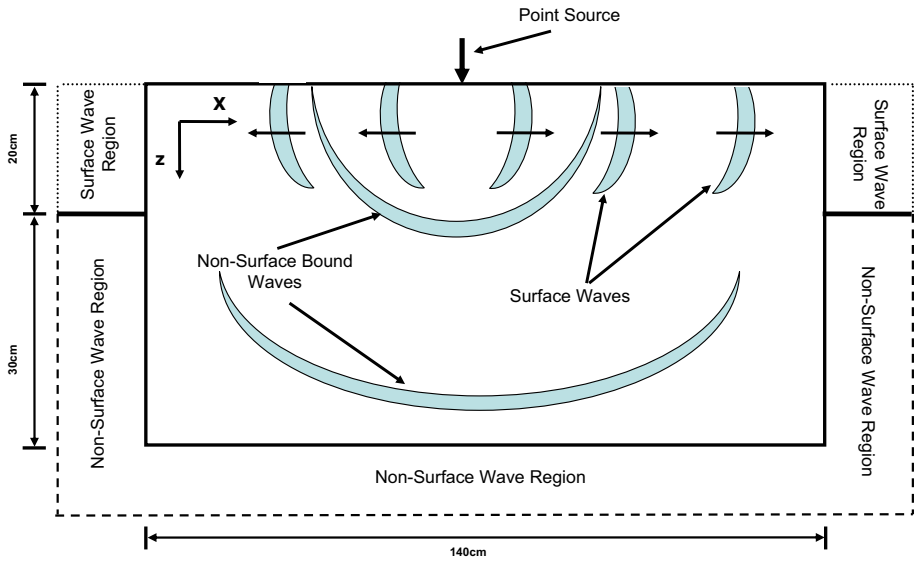

Figure 88: The Poynting vector calculator is used to determine the amount of energy exiting the FDTD simulation space in a region near the surface and a region far from the surface. This division of energy is an approximation for the energy contained in the surface-bound waves vs. the non-surface-bound waves.

There is critical difference between this numerical simulation and the previous simulations examining the impact of scattering object density. In order to isolate the effects of mode conversion, the source is a point source placed in the *center* of the scattering field instead of on one side of it. In the simulations presented earlier in this section in Table 9, energy propagated *through* a region of scattering objects. This means that a significant amount of the energy that is incident on the scattering field is reflected and does not propagate through to the other side, as was demonstrated by Figure 86. Placement of the point source in the center of the scattering region guarantees that energy that arrives at the edge of the solution space has propagated through the scattering field. Figure 89 shows the varying cylinder concentrations

for the simulations from 20 cylinders to 120 cylinders. The location of the point excitation source is also noted. In addition to the different cylinder densities, a numerical simulation was also performed where there were no scattering objects were included (zero cylinders).

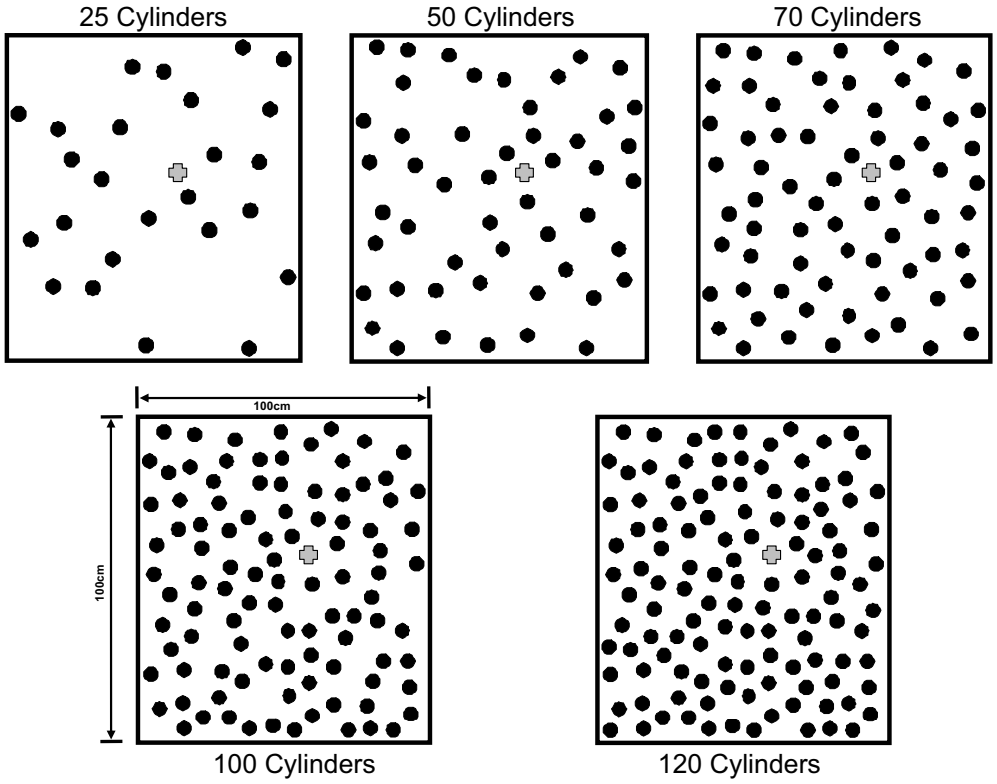

Figure 89: The layout of scattering cylinders for different densities within the scattering region used to calculate the amount of energy retain in the surface wave. The location of the point source is noted by the cross located in the middle of the scattering objects.

The results of the numerical simulation, presented in Figure 90, demonstrate that as the number of scattering objects increases, the percentage of the energy contained in the surface layer decreases in a roughly linear fashion. This indicates that as more scattering objects are added, mode conversion can result in a significant loss in the amount of energy present at the surface, and available for time-reversal focusing.

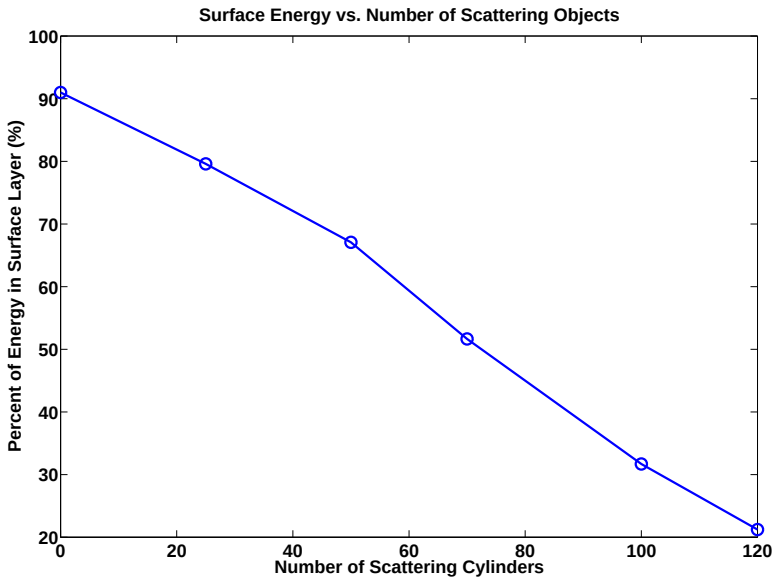

Figure 90: The percentage of energy confined to a surface layer for varying densities of scattering cylinders.

7.2 Scattering Object Shape

The relative size of the scattering object is not the only characteristic that can effect time-reversal focusing. Different types of objects will scatter and mode-convert energy differently. A comparison of two types of scattering objects is shown in order to characterize and compare the scattering from a sphere and cylinder of the same radius. Both objects are made from concrete and are placed in layered soil.

Beginning with a qualitative assessment, a uniformly excited array excites a differentiated Gaussian pulse which interacts with each of the objects. The results of scattering off a single cylinder were previously presented in Figure 87. Figure 91 presents identical data for a single 2.5 cm radius sphere. Both figures are time-snapshots of the propagation of the of waves through the solution space. These images are presented on a 40 dB pseudo-color amplitude scale from white (0 dB) to black (-40 dB). A comparison of the intensity of the reflected waves on the surface (X-Y plane) for the cylinder and the sphere shows a significantly stronger surface reflection from the

cylinder. Thus for two objects of equal radius, the cylinder reflects energy more strongly.

In order to more closely examine the scattered waves, it is necessary to observe the wave fields as a function of depth. Time-snapshots of the solution space as a function of depth are presented (X-Z plane) to enable a more clear assessment of the behavior of the scattered wave field. In these images, the incident wave field is subtracted and only the scattered waves are presented. In the snapshots of the scattered-only wave in Figures 87 and 91, the 0 dB level is adjusted once the incident field is removed to give better resolution to the scattered waves.

A comparison of Figures 87 and 91 confirms that the cylinder scatters significantly more energy than does the sphere. This is apparent in the 7 dB drop in displacement amplitude between the reflected Rayleigh wave for the cylinder (Fig. 87) and the sphere (Fig. 91). A qualitative comparison of the level of mode conversion for the two objects reveals that the difference in the amplitude of the reflected Rayleigh wave and the downward travelling wave is similar between the two objects: 17 dB of contrast for the cylinder and 15 dB for the sphere.

The similar ratios of reflected Rayleigh to mode-converted waves indicate that for these two types of scatterers, the relative levels of mode conversion are similar. This initial investigation of a single scattering object indicates that in a comparison of focusing resolution for cylinders or spheres, the focusing resolution is expected to be greater for cylinders since scattering is more effective, and with slightly less energy lost to mode conversion and downward scattering.

The surface wave energy calculation presented in Figure 90 is repeated for arrays of scattering spheres of 2.5 cm radius and the results are added to the data for cylinders. Figure 92 demonstrates that for small numbers of cylinders and spheres, the differences in mode conversion are not significant. As the number of scattering objects grows, the difference in the level of mode conversion becomes apparent. The

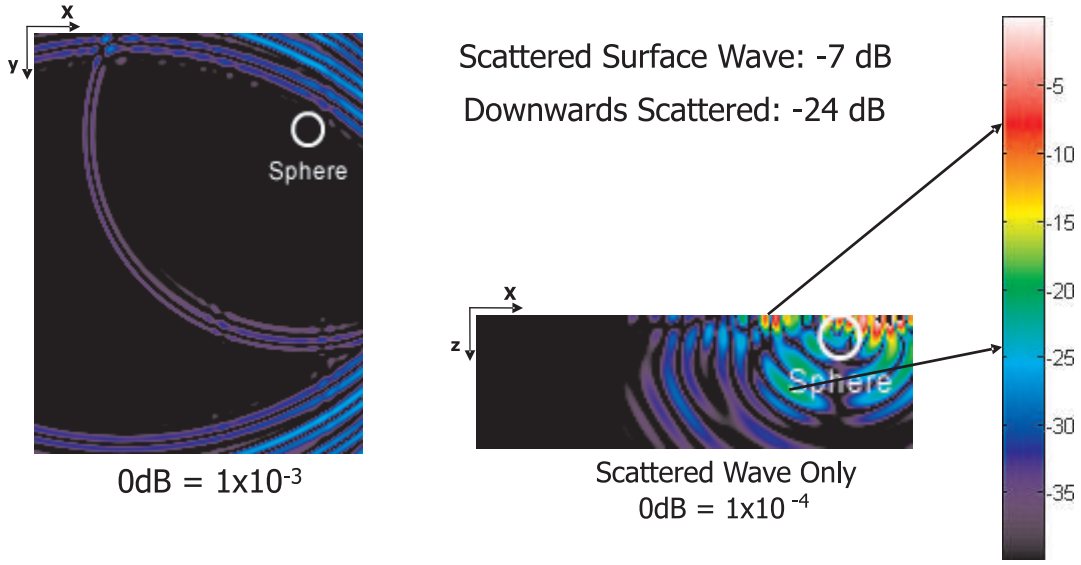

Figure 91: Snapshots of scattering and mode conversion from a single sphere. The X-Y section is a surface time-snapshot, while the X-Z section is a vertical plane through the solution space. The sources are the 12 bar-foot sources located as depicted in Figure 82.

indication is that for cylinders and spheres of the same radius, the cylinders tend to scatter energy more effectively, promoting more mode conversion and therefore more energy lost into the ground.

While understanding the specific differences between the scattering and mode conversion from 2.5 cm radius concrete cylinders and spheres may not be particularly informative, methods for assessing the varying levels of scattering mode conversion for different sizes and shapes of scattering objects are worthy of discussion. These differences in scattering and mode conversion may be contributing factors to focusing effectiveness.

Beyond the quantifiable effects of mode conversion, the effect of different scattering objects on focusing resolution can also be examined. The number and shape of the scattering objects should have an effect on the focusing resolution based both on how much energy each object converts from surface bound energy, and how effectively the objects scatter the surface waves to create high-order scattering on the surface.

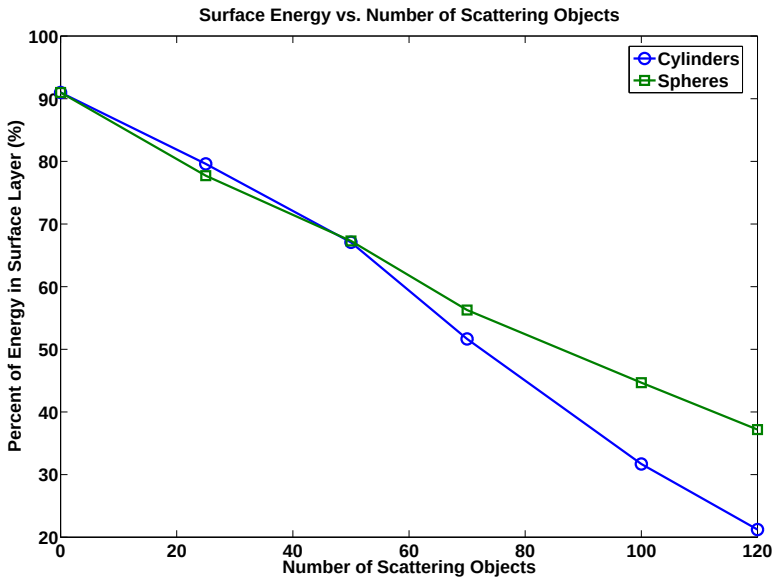

Figure 92: The percentage of energy confined to a surface layer for varying densities of scattering cylinders and spheres.

Figure 93 compares the 6 dB focusing spot size for no scattering objects, and two different concentrations of cylinders and spheres. This confirms that for these two identical scattering fields - one of cylinders and one of spheres, that the spheres will produce a poorer resolution at the focusing spot. The shape of the scattering objects present can have a measurable effect on time-reversal focusing for elastic waves.

7.3 Scattering Object Orientation

For an object such as a sphere, orientation is not important, but for an object such as a cylinder, its orientation in the propagation medium may have some effect on how much energy is mode converted from the object, or how effectively it scatters. In order to investigate this relationship, a field of 50 cylinders was created. Three different levels of random "tilt" were introduced. In the first set of cylinders, all cylinders were completely vertical. In a second set, each cylinder's orientation was allowed to vary by $\pm 5^\circ$ in any direction from vertical. In a third set, the random tilt of each cylinder was $\pm 10^\circ$ in any direction.

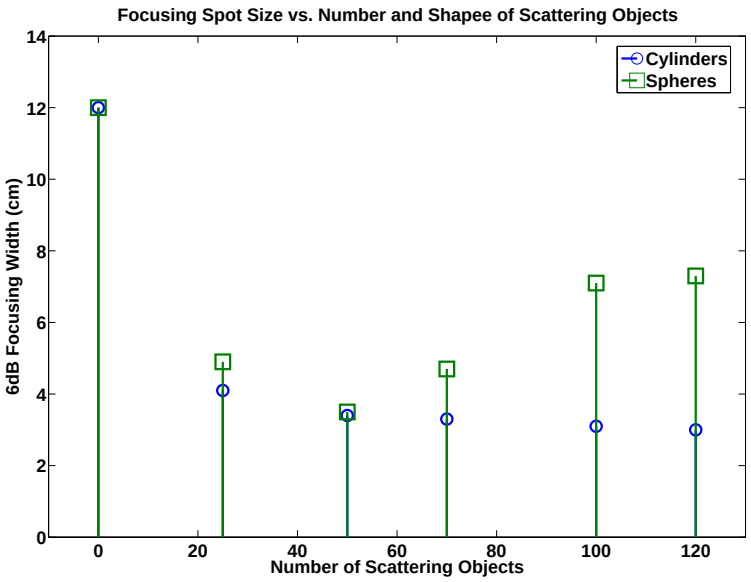

Figure 93: The focus spot size is compared for different numbers of scattering objects, and for two different scattering objects shapes.

Degrees of Random Tilt	6 dB Width	Peak Amplitude (dB)
$\pm 0°$	3.4 cm	-27.26 dB
$\pm 5°$	3.4 cm	-27.32 dB
$\pm 10°$	3.3 cm	-27.41 dB

Table 10: Time-reversal focusing results for varying the degree of random tilt of the cylinders in the scattering region. The 6 dB cross-range focus spot size and peak amplitude at the focus point are presented.

Time-reversal focusing was performed on each set of cylinders for a 900 Hz center frequency. The results, presented in Table 10 demonstrate that no significant impact on focusing resolution was observed. More drastic alterations of the orientation may have a more drastic effect, but the primary purpose of this simulation is to determine the effect of some undesired variation that may occur in experimental research burying cylinders. The conclusion is that for variations of less than $\pm 10°$, there is no significant effect on time-reversal focusing resolution.

7.4 Experimental Results

The numerical investigation of the impact of geometry-dependent scattering on time-reversal focusing has provided an opportunity to further characterize time-reversal focusing in an elastic medium, with finite-sized scattering objects. The numerical model, however, is simplistic. It is unable to completely account for effects such as imperfect coupling between excitation sources and the surface of the soil, the non-linearity of the propagation medium, the coupling between scattering objects and the medium, and ambient noise in the experiment.

Further, experimental observations are limited in the scope of their measurement capabilities. Without perturbing the medium, and with the experimental measurement equipment available (Section 4.2), wave fields can only be measured on the surface. Given all the additional variables, and armed with a better understanding of its behavior from the numerical model, it is useful to examine time-reversal focusing from an experimental standpoint.

To that end, the concrete cylinders described previously in Section 4.2.3, were used to create 50 and 70 cylinder layouts in the experimental facility. The experimental configuration mimics the numerical model setup as described in Figure 82. The data collection procedure has been previously described in Section 4.2. The cylinders are buried in the same locations as the cylinders in the numerical model. Figure 94 shows 50 buried cylinders in the experimental facility.

Time-reversal focusing is performed to a point in the center of the measurement region, as for the results from the FDTD model presented in Section 7.1. As in the model, a 900 Hz differentiated Gaussian pulse excitation is used to create the time-reversal focusing drive signals. The experimental results for time-reversal focusing spot size can be compared to the numerical results the cases of 50 and 70 cylinders. Table 11 demonstrates that there are significant differences in the predicted numerical and actual experimental effectiveness of time-reversal focusing for the arrays of

Figure 94: 50 concrete cylinders are buried in the experimental facility. The ground-contacting sensor array and elastic wave transducers are also visible in the photo.

Number of Scatterers	Experimental or Numerical	6 dB Width
50 Cylinders	Numerical	3.4 cm
50 Cylinders	Experimental	13.7 cm
70 Cylinders	Numerical	3.3 cm
70 Cylinders	Experimental	22.1 cm

Table 11: A comparison of time-reversal focusing 6 dB focusing spot size for numerical and experimental data.

scattering objects presented.

The numerical model is an extremely useful tool in modelling elastic wave behavior, but the drastic differences between numerical model and the experimental results clearly demonstrate that the model is unable to completely represent the conditions present in the experiment. While adding additional degrees of freedom to the model is beyond the scope of this investigation, some of the factors contributing to this difference should be noted.

First is the assumption of perfect coupling of the excitation signal into the ground.

The elastic wave transducers have both an internal transfer function, and a complex coupling interaction to the soil. The model completely ignores this contribution of the experimental system. In addition, propagation through the model is assumed to be perfectly linear and lossless. As previously mentioned, both of these assumptions are inaccurate. Soil is a particulate medium that is lossy, non-linear at higher amplitudes, and its particular qualities may be frequency dependent[14]. The cumulative effects of these differences leads, among other things, to the model over-estimating the high frequency content of the signals that will arrive at the focus point. This over-estimation causes the model to focus more tightly than the experimental work. Chapter 8 will examine some of these effects in more detail.

The model also assumes ideal coupling between any two media. This assumption becomes particularly important for the investigation of time-reversal focusing. Since the model assumes perfect, lossless coupling, it tends to overestimate the energy scattered by any particular object. For time-reversal focusing with scattering objects, this leads to an overly optimistic estimate of the mean-path length which directly correlates to the focusing spot resolution. This effect also causes the model to overestimate the resolution of time-reversal focusing.

Over the evolution of the experimental system, several modifications have been made to reduce the impact of the aforementioned factors. Averaging methods are used to reduce noise in experimental measurements, and to allow very low excitation levels - which behave almost linearly. The concrete cylinders were constructed by filling corrugated thin-walled pipe with concrete in order to improve coupling by minimizing slippage between the soil and the cylinders. There may be additional experimental modifications that could improve agreement, but future work should address these additional complexities in the numerical model.

While these effects do provide limitations for the utility of the model in its present form, future work could address the inaccuracies of the model in order to better

incorporate effects such as loss, physical coupling, and amplitude-dependent nonlinearity.

CHAPTER VIII

EFFECTS OF NON-LINEARITY AND NOISE ON TIME-REVERSAL FOCUSING

8.1 Motivation

The theory of time-reversal focusing is based on an assumption of linearity for time-reversal focusing to be completely effective (Section 2.2). Like many other theoretical requirements however, linearity is not completely satisfied when examining wave propagation through soil. Elastic wave propagation in soil is more complicated than in simple elastic media. Soil is a non-linear particulate medium where interparticle forces and physical characteristics including particle sizes, shapes, and density significantly impact the characteristics of the medium and thereby the types of wave propagation it supports [14].

Of particular interest in the case of experimental studies of time-reversal focusing in soil is the tradeoff between non-linear behavior and signal amplitude. The soil medium is quasi-linear when the waves excited within it are of a small amplitude, but as these amplitudes increase, wave propagation becomes increasingly non-linear [34]. This creates a challenge when attempting to perform time-reversal focusing in soils since there is a direct tradeoff between drive signal amplitude and signal-to-noise ratio. In most of the experiments performed in the experimental facility described in Sections 2.1 and 3.3, the drive signal amplitude of the elastic wave sources has been selected in the region where the result is some slight non-linear propagation. This amplitude has always been chosen in order to optimize the tradeoff between signal-to-noise ratio and the undesired non-linearity.

In this chapter, the impact of signal-to-noise ratio and drive signal amplitudes with respect to non-linearity and time-reversal focusing effectiveness will be examined

through a sequence of experiments. The first set of experiments to be performed will examine time-reversal focusing effectiveness by artificially varying the noise content of the drive signals and the amplitude of the drive signals in order to introduce non-linearity. The second set of experiments will examine the effect on time-reversal focusing when the drive signal is abruptly truncated. The length of the truncated signal will be shown to have an effect on both the focusing effectiveness and the noise level of the signal. Lastly, the impact of artificial noise and amplitude variations on chirp drive signals will be compared to the effects that are observed for time-reversal focusing drive signals.

8.2 Experimental Method

8.2.1 Experimental Setup

The sand tank in the experimental facility is cleared of all scattering objects and the experiments are performed in homogeneous damp compacted sand. A focusing point in the middle of the sand tank is chosen at X=150 cm and Y=0 cm and an array of 12 elastic wave transducers is used to create the time-reversal drive signals. Data is collected using the ground-contacting accelerometer array in the same method used in previous experiments employing this sensor array (Section 4.2).

8.2.2 Amplitude and Noise Modifications

For the "Noise vs. Amplitude" experiment to be discussed in Section 8.3, a method is developed to artificially vary the noise content and amplitude for the time-reversal drive signals.

In order to introduce noise into the time-reversal drive signals in a controlled way, an extremely low-noise or "clean" set of time-reversal drive signals is generated for each experiment using the procedure described in Section 4.2.2. Recall that the clean signal is generated by successively recording the drive signals and averaging the response 100 times. This averaging significantly reduces any random noise in

the drive signals that may have otherwise reduced their signal-to-noise ratio. Once a clean set of drive signals has been produced, a set of 12 band limited Gaussian white noise signals is also generated. There are 12 uncorrelated noise signals, $\Phi_{TR_k}(t)|_{k=1:12}$, one for each transducer in the array.

All the noise signals, $\Phi_{TR_k}(t)$, are the same length as the time-reversal drive signals, 4.096 seconds, and all the noise signals have the same total energy over their full length ($E_{\Phi_{TR_1}} = E_{\Phi_{TR_2}} = ... = E_{\Phi_{TR_{12}}}$). Recall that the result of the drive signal truncation procedure from Section 4.2.2 and Equations 42 - 51, a set of 12 time-reversal drive signals can be created. In Section 4.2.2, each of these signals contained only ambient noise, and each was generated using the same drive level, referred to here as A_1.

In order to study the effects of noise and non-linearity on time-reversal focusing, it will be necessary to add a few new steps to the procedure described in Section 4.2.2. New sets of time-reversal drive signals will be created, each with different drive levels and different amounts of added noise. Recall that the transfer function of the propagation through the experimental setup is not completely linear, so as the amplitude of the drive signal is varied, this will change the transfer function through the soil. Therefore, we must update the amplitude independent description of the time-reversal drive signals given in Section 4.2.2. The averaging procedure begins by taking 100 separate measurements, S_i, and averaging those to reduce ambient noise. Taking into account amplitude variations and weak non-linearity in the soil, Equation 42 can now be approximated as,

$$S_i(t,m) \approx A_m C(t) * T(t,m) + \Phi_i(t). \tag{53}$$

where A_m is the amplitude of the chirp signal. $T(t,m)$ is the quasi-linear time-domain transfer function or impulse response of the entire system. Note that this transfer function is not only a function of time, but also of the amplitude multiplier m of

the excitation chirp signal. This quasi-linear approximation holds true for the range of amplitudes used in these experiments. $\Phi_i(t)$ is the random noise that is recorded for the i^{th} iteration when generating the time-reversal drive signal according to the procedure described in Section 4.2.2.

Consistent with the addition of amplitude as a variable, the full length (untruncated) version of the impulse response is now,

$$T(t,m) = \mathcal{F}^{-1}\left\{\frac{\mathcal{F}\left\{\sum_{i=1}^{100} S_i(t,m)\right\}}{\mathcal{F}\left\{C(t)\right\}}\right\}. \tag{54}$$

Continuing through the procedure described in Section 4.2.2, this time-domain impulse response can be transformed into the frequency domain. The impulse response is then windowed in the frequency domain to remove extraneous information that lies outside the frequency range of interest. The new transfer function is then transformed back to the time domain to give a time-domain impulse response,

$$T_F(t,m) = \mathcal{F}^{-1}\left\{T(f,m)W_F(f)\right\}. \tag{55}$$

The bandpass filter, W_F is defined as,

$$W_F(f) = \begin{cases} 0 & : \quad 0 < f < 99.85\,\text{Hz} \\ 1 & : \quad 100 \leq f \leq 2\,\text{kHz} \\ 0 & : \quad f > 2\,\text{kHz}. \end{cases} \tag{56}$$

A "clean" impulse response is then be created through the truncation process described in Equation 49 to yield a new impulse response,

$$T_{truncated}(t,m) = T_F(t,m)W_T(t), \tag{57}$$

Where $W_T(t)$ is a window function defined in the time domain as,

$$W_T(t) = \begin{cases} 1 & : \quad 0 \leq t \leq 200\,\text{ms} \\ 0 & : \quad 200\,\text{ms} < t \leq 4.096\,\text{s}. \end{cases} \tag{58}$$

A time-reversal drive signal can then be created by convolving with the excitation chirp and time-reversing the signal to yield,

$$TR(t,m) = C(-t) * T_{truncated}(-t,m). \tag{59}$$

This procedure is completed for each of the 12 time-reversal focusing drive signals to create a set. The entire set of signals is then normalized to the maximum amplitude of the set of 12 signals. This yields a set of normalized drive signals,

$$TR_{norm_k}(t,m) = \frac{TR_k(t,m)}{\max\limits_{L=1:12}\left(\max\limits_{t}|TR_L(t,m)|\right)}. \tag{60}$$

The drive signals are normalized here in order to utilize the full resolution of the digital-to-analog output of the data acquisition system. The amplitude modifications, A_m, will be re-introduced later by an amplifier as part of the data acquisition system. However, the signals remain a function of m since the nonlinear component of the impulse response is a function of the excitation amplitude.

Once the signals are normalized, the set of 12 uncorrelated noise signals, Φ_{TR_k} is superimposed on the set of 12 clean time-reversal drive signals. This creates a set of noisy time-reversal drive signals,

$$TR_{noisy_k}(t,m) = TR_{norm_k}(t,m) + \Phi_{TR_k}(t). \tag{61}$$

The addition of the noise signals may increase the peak amplitude of the time-reversal drive signals. Recall that previous research has demonstrated that high amplitude signals alter the magnitude of the non-linear component of the signal that propagates through the quasi-linear elastic medium. Because the experiment will

modify the non-linear content of the signal using the amplifier in the data acquisition system, the signals are again normalized to maintain a consistent peak amplitude.

In order to create an entire set of signals, the amplitude of the noise signals, Φ_{TR_k}, can be modified in addition to the amplitude, A_m of the set of time-reversal drive signals. For the experiment in Section 8.3, 6 different noise levels (N_1 - N_6) and 5 drive levels (A_1 - A_5) will be used to generate a matrix of 30 sets of time-reversal drive signals. These 30 different sets of drive signals are each used to generate a time-reversal focusing data set. The 6 different noise levels, N_1 - N_6, are of increasing noise powers, such that as they are added to the clean time-reversal drive signals, the composite signal with a noise level N_1 has a higher signal to noise ratio than the signal with noise level N_6. The same set of noise signals, N_1 - N_6, is applied to all 5 amplitude level time-reversal drive signals. The amplitudes of the drive signals increase from A_1 to A_5 in a way such that A_m is m times as large as A_1.

In order to ensure that the amplitude modifications, A_m, are the dominant source of non-linearity, the signals are re-normalized after noise is added to each set. After the second normalization, the k^{th} time-reversal drive signal, of amplitude A_m and noise level N_n is,

$$TR_{noisy,norm_k}(t,m,n) = \delta(n,m)\big[TR_{norm_k}(t,m) + \Phi_{n,TR_k}(t)\big]. \tag{62}$$

where δ is defined as,

$$\delta(n,m) = \frac{A_m}{\max\limits_{k=1:12}\big(\max\limits_{t}|TR_{norm_k}(t,m) + \Phi_{n,TR_k}(t)|\big)}. \tag{63}$$

Because of this normalization procedure (Equations 60 - 63), the signal to noise ratio varies between signals using different drive amplitudes. Figure 95 shows the relationship between noise level, amplitude and signal to noise ratio for the matrix of 30 signals.

A flowchart of the procedure used to create these time-reversal excitation signals

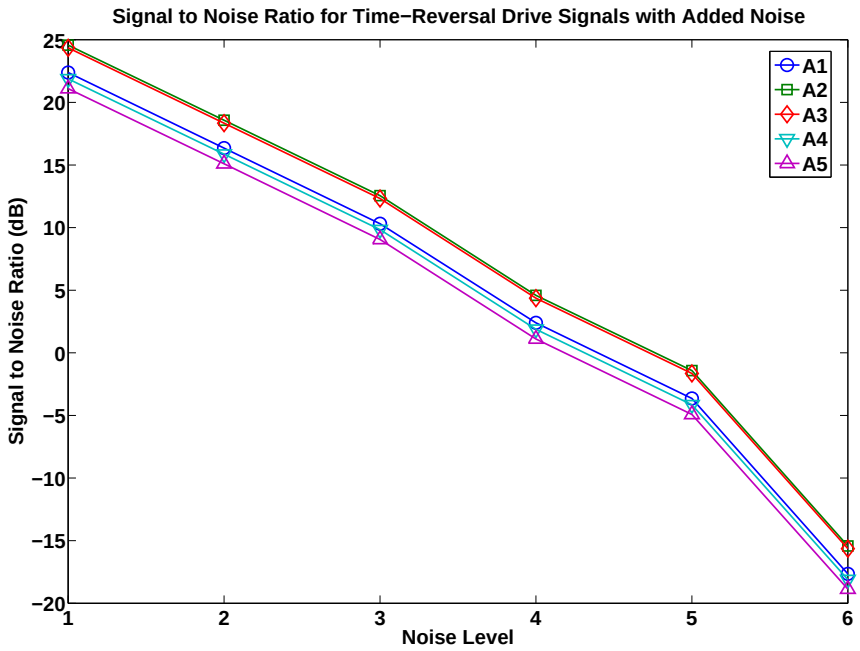

Figure 95: The signal to noise ratio of the energy contained in the time-reversal drive signals in the 30 signal matrix, after noise is added to each signal.

is depicted graphically in Figure 96. A set of signal graphs is also presented, showing several stages of the process. The excitation signal used in the sand tank is a 4.096 s swept frequency chirp signal described in Section 2.3.2. Once this chirp (Figure 97a) is used to create the clean time-reversal drive signal (Figure 97b), the noise signals (Figure 97c) are added to the time-reversal drive signal. This composite signal (Figure 97d) is used to excite the transducer array during time-reversal focusing. While the composite signal (Figure 97d) is used as the excitation signal, it may also be examined after removing the chirp, and compressing with a differentiated Gaussian pulse. Figure 97e shows the resulting pulse-compressed time-reversal drive signal.

8.2.3 Accounting for Normalization

The normalization procedure described in Section 8.2.2 is important to ensure that non-linearity is only introduced from the controlled amplitude modifications represented by the amplitude multiplier, A_m. Though they are necessary for experimental

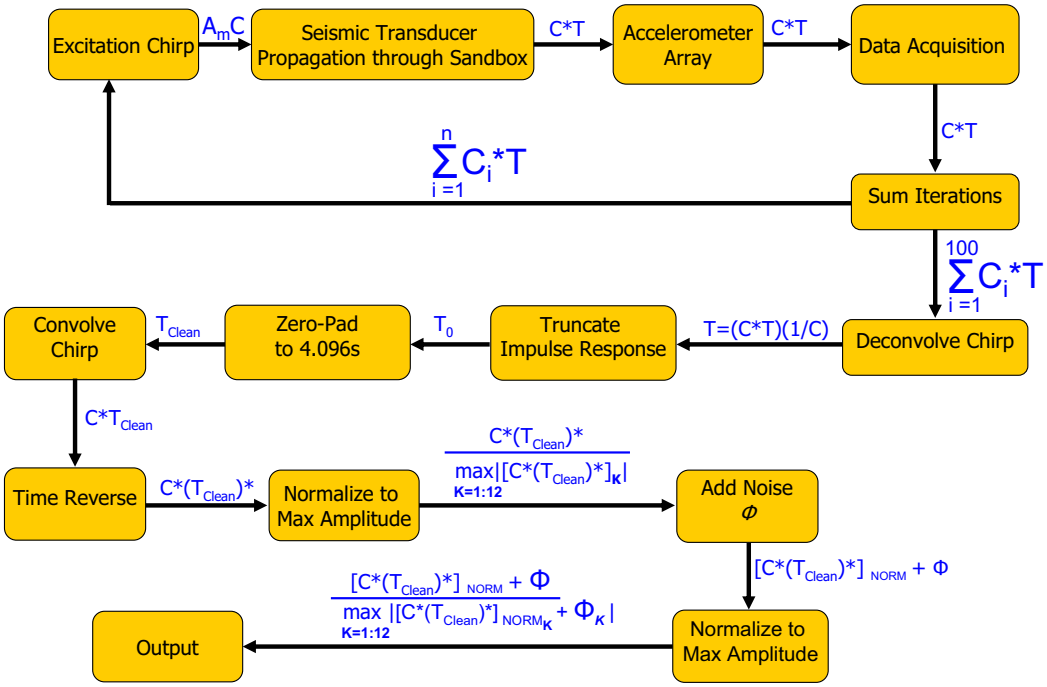

Figure 96: Flowchart showing the data acquisition and processing steps to create one of the time-reversal drive signals with added noise. The process is depicted for a single signal that is a member of the set of 12 signals used to collect a single data set.

control, the resulting amplitude modifications must be taken into account if different sets of time-reversal drive signals are to be compared using any metric which depends on signal amplitude to evaluate time-reversal focusing effectiveness.

In order to account for the amplitude normalization performed in Section 8.2.2, an equalization factor must be created for each set of experimental results that accounts for the reduction in amplitude caused by normalization of the time-reversal drive signals. This factor should also take into account the fact that a signal of amplitude A_m should be m times larger in amplitude than a signal of amplitude A_1 if linearity holds.

The equalization factor should consider the amount of energy in the *signal*, but not the added noise. The equalization factor begins with the noisy time-reversal

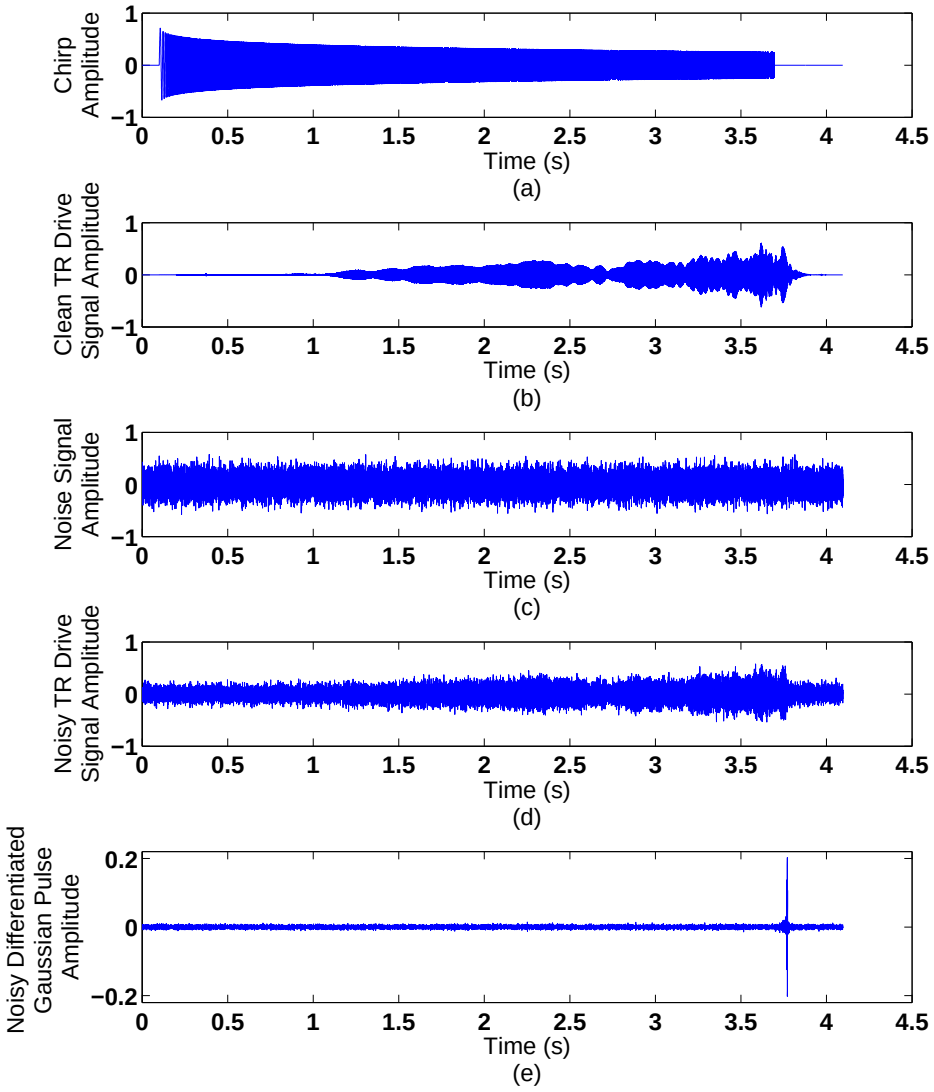

Figure 97: Signals used in the normalization procedure. a) The time-domain swept frequency chirp signal. b)The clean time-reversal drive signal after normalization. c)The Gaussian white noise signal that will be added to the time-reversal drive signal. d)The composite noisy time-reversal drive signal after normalization. e)The time-reversal drive signal after being pulse compressed using a 900 Hz differentiated Gaussian pulse.

drive signal, Equation 62. This excitation signal is compressed using a differentiated Gaussian pulse in the same manner as the final time-reversal focusing results,

$$TR_{DG_k}(t) = \mathcal{F}^{-1}\left\{\frac{\mathcal{F}\left\{TR_{noisy,norm_k}(t)\right\}\mathcal{F}\left\{\gamma(t)\right\}}{\mathcal{F}\left\{C(t)\right\}}\right\}, \tag{64}$$

where $\gamma(t)$ is the differentiated Gaussian pulse described in Section 2.3.2, and Equations 7-8 with a center frequency of 900 Hz. When the signal is compressed, most of the energy lies in the pulse, causing the peak of the differentiated Gaussian pulse to be much higher than the noise floor (Figure 97e). This peak amplitude value for each of the different noisy excitation signals is used as the equalization factor when comparing the time-reversal focusing results.

8.3 Noise vs. Amplitude Correlations in Time-Reversal Focusing

High amplitude drive signals are used to generate non-linear content in the time-reversal drive signals. The non-linearity is a result of the properties of the soil and the coupling between the soil and the elastic wave transducers. These non-linear effects are both amplitude and frequency dependent, and are more observable at high frequencies. Because of this, as a broadband excitation signal becomes increasingly non-linear, high frequency content will decrease in comparison to the low frequency content for the signal that is recorded at the focus point after propagating through the soil. While this behavior is known, there may also be an effect caused by the presence of noise in the time-reversal focusing signal. The results presented in this section examine the impact that noise has on the presence of non-linearity and focusing effectiveness in time-reversal focusing.

The first experiment examines the relationship between noise in the time-reversal drive signals and the non-linearity created by increasing the drive amplitude of the seismic sources. Previous experimental research has demonstrated a loss of high frequency information due to the generation of non-linear excitation signals [34], but these experiments have not examined the effect of non-linearity on time-reversal

focusing. A correlation may also exist between the signal-to-noise ratio, the amplitude of the excitation signals, the focusing effectiveness and the loss of high frequency information due to non-linear effects. In order to evaluate these relationships, a matrix of 30 sets of time-reversal focusing experiments are performed using 5 different drive signal amplitudes and 6 different levels of random noise superimposed over the transmitted time-reversal drive signals. These drive signals are described in detail in Section 8.2.

8.3.1 Amplitude vs. Frequency

A simple method of measuring the impact of non-linearity and noise on the frequency content of the recorded time-reversal focusing signal is to measure a ratio of high frequency to low frequency signal content for the signals that arrive at the focus point. Time-reversal focusing signals with varying amplitudes and levels of noise are created using the procedures outlined in Sections 8.2. Then the high frequency to low frequency ratio is generated by transforming the recorded time domain signal into the frequency domain and summing the amplitudes of each frequency component from 200 Hz to 800 Hz for the low frequency content, and from 800 Hz to 1.4 kHz for the high frequency content. These ratios are computed for the data recorded at the time-reversal focusing point for each of the 30 experiments. Each set of frequency data, $D(f)$, is self-normalized to its own maximum amplitude in the frequency domain (Equation 65) such that the peak amplitude of the largest frequency component is 0 dB.

$$D_{norm}(f) = \frac{D(f)}{\max_f |D(f)|}. \tag{65}$$

An example of the data used to compute the high frequency to low frequency ratios is presented in Figure 98. This data shows the frequency response at the focus

point for various drive levels, but a single noise level. While this allows for a qualitative evaluation, the ratios are a more quantitative assessment of frequency content. Further, the data varies over noise level as well as amplitude. The data demonstrates two trends. Figure 99 shows a drop in the high frequency to low frequency ratio (HF:LF) as the amplitude of the drive signal increases. This trend is a confirmation of the relationship between non-linearity and frequency content. As the excitation signal amplitude is increased, the large amplitude motion of the transducer causes the signal that propagates through the soil to become increasingly non-linear. This is due to the non-linear behavior of the soil when it is excited at high amplitudes. This non-linearity effectively causes attenuation in the high frequency range as the wave propagates. In addition, as the drive signal amplitude is increased, the coupling between the elastic wave transducer and the surface of the sand becomes less efficient in transferring energy from the transducer to the sand, which further impacts this ratio.

The second notable trend,demonstrated by Figure 100, is the drop in the HF:LF ratio as the signal-to-noise ratio is decreased. The noise introduced into the drive signals is bandlimited white noise. Because the noise energy is spectrally white, in a linear regime it should act as an offset for the entire spectrum. Without noise, the ratio of high frequency energy, E_H to low frequency energy, E_L, would be,

$$(HF:LF)_{noisefree} = \frac{E_H}{E_L} \tag{66}$$

Each bandlimited white noise signal has some amount of energy, E_Φ that is equally distributed across the frequency range of interest such that,

$$E_{\Phi_{LF}} = E_{\Phi_{HF}} \tag{67}$$

where LF and HF are the high frequency and low frequency bands of 200 Hz to 800 Hz and 800 Hz to 1.4 kHz respectively. Because $E_{\Phi_{LF}}$ and $E_{\Phi_{HF}}$ add equal amounts of

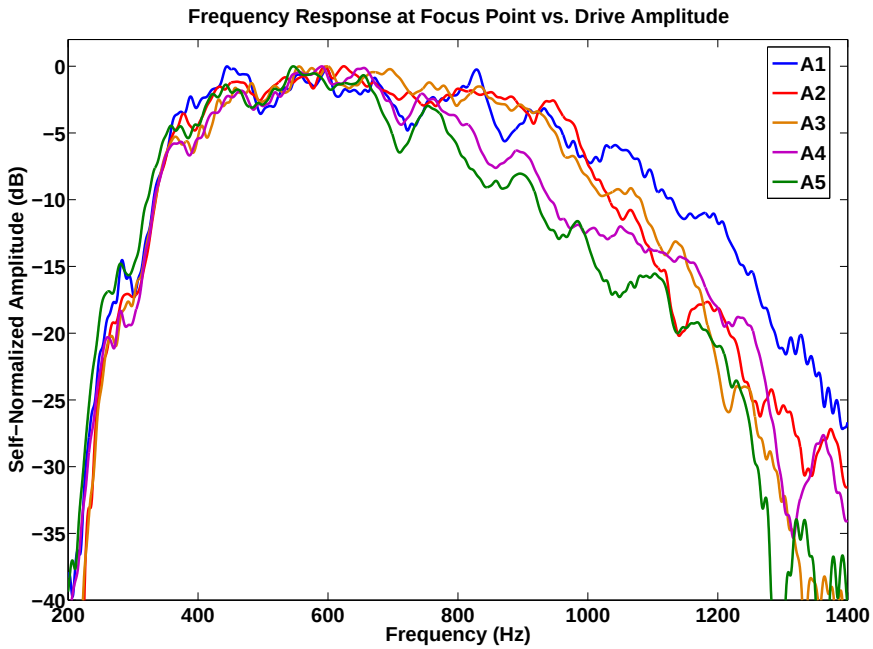

Figure 98: An example of the data used to compute the high frequency to low frequency ratios. This data shows the frequency response at the focus point for various drive levels, but a single noise level.

energy to both sides of the HF:LF ratio, this should have the effect of pushing the HF:LF ratio higher such that,

$$HF : LF = \frac{E_H + E_{\Phi_{HF}}}{E_L + E_{\Phi_{LF}}} > \frac{E_H}{E_L}. \tag{68}$$

Instead, we observe the opposite trend. As the noise level increases, decreasing the signal to noise ratio of the excitation signal, the data shows that additional high frequency energy is lost, reducing the HF:LF ratio.

The drop in high frequency energy as additional noise is added is attributable to the normalization of the composite noisy drive signal. When noise is superimposed on the clean drive signal, the peak amplitude of the composite signal increases. These larger peak amplitudes can drive the elastic wave transducers into a more nonlinear excitation. Since the goal is to test the impact of signal to noise ratio on time-reversal

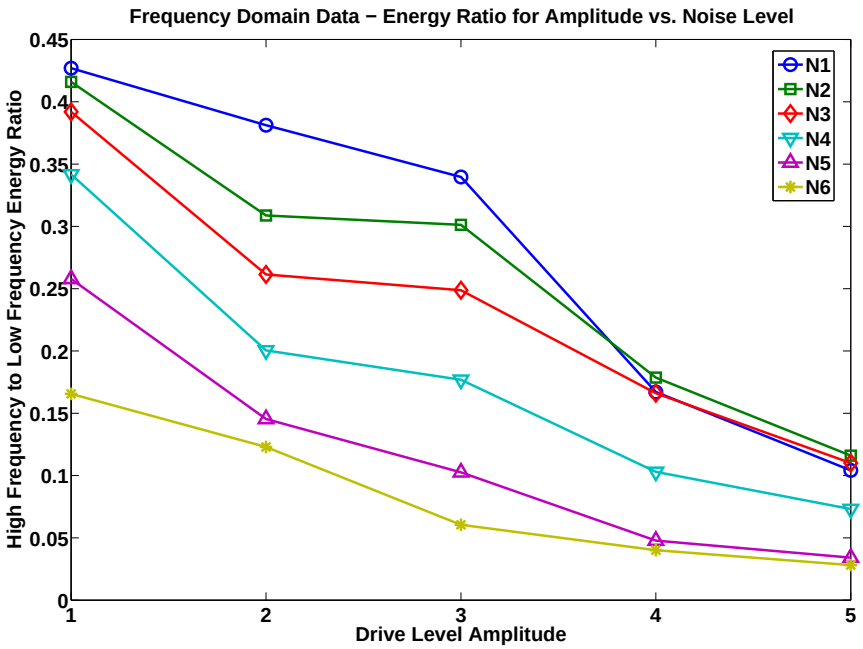

Figure 99: High Frequency to Low Frequency ratios of energy for the time-reversal focusing signals recorded at the desired focusing point. This graph presents the HF:LF ratios on curves of constant noise level for varying amplitudes.

focusing, the excitation signals must be generated in a way that isolates the effects of non-linearity caused by large amplitude excitation signals. In order to prevent this additional nonlinearity, the total amplitude of the new composite noisy signal is adjusted to maintain the same peak amplitude level as the clean drive signal. This normalization procedure was described in Section 8.2.3, and Equations 59 - 64. This peak-amplitude normalization is taken into account using the equalization factor described in Section 8.2.2 when evaluating time-reversal focusing effectiveness.

Because of the amplitude normalization, the drop in high frequency energy that occurs with the addition of noise may seem to be artificial. However, normalization of the composite signal can be seen as a method for avoiding high frequency loss due to the non-linear behavior that would be observed if excitation amplitudes were to be even higher. This experiment demonstrates that for time-reversal focusing, and truly for other excitation methods as well, reduction in high frequency energy will be caused

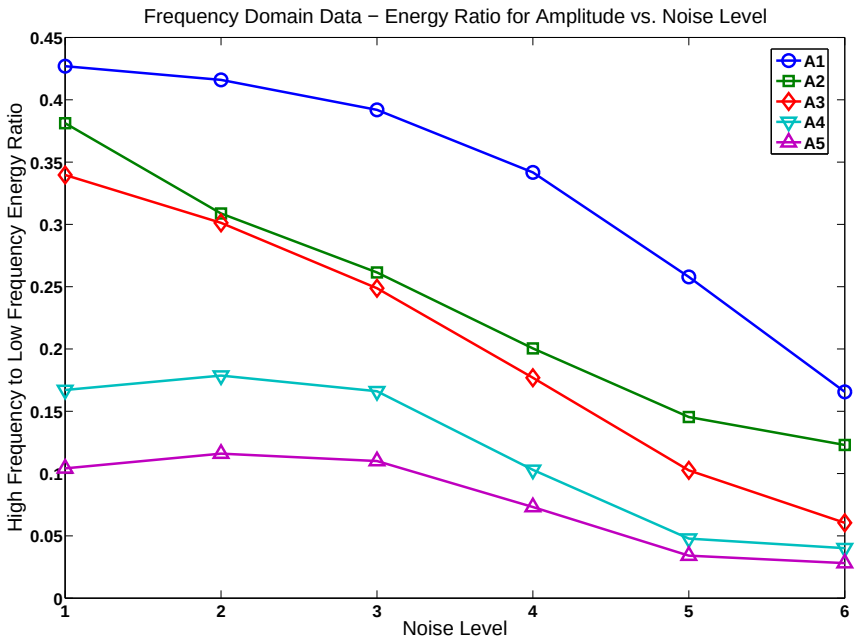

Figure 100: High Frequency to Low Frequency ratios of energy for the time-reversal focusing signals recorded at the desired focusing point. This graph presents the HF:LF ratios on curves of constant drive amplitude level for varying noise levels.

not only by non-linearity. Noise seems to enhance the non-linear loss. As the added noise drives the source-ground coupling into the non-linear regime, high frequency energy will continue to be lost. Figure 101 provides a summary of the results: both amplitude-induced nonlinearity and low signal-to-noise ratios can induce significant loss of high frequency energy in time-reversal focusing.

8.3.2 Focusing Effectiveness

High noise levels effectively reduce the amount of high frequency energy that reaches the focus point for time-reversal focusing. Since high frequency energy allows a focus spot to be resolved more tightly, the addition of noise, or an increase in excitation amplitude, should translate into a reduction in focusing spot resolution - the focusing spot size should increase. In this section, two different methods are employed to observe the impact of noise and excitation amplitude changes on focusing effectiveness.

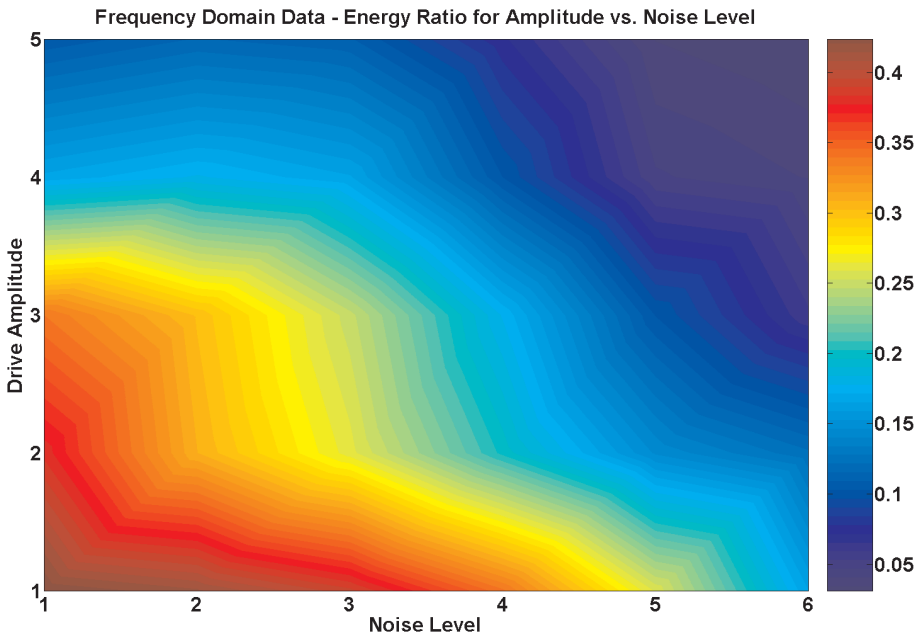

Figure 101: High Frequency to Low Frequency ratios of energy for the time-reversal focusing signals demonstrate that as non-linearity increases (through increasing drive levels), or as the signal-to-noise ratio worsens, additional high frequency energy will be lost at the time-reversal focus point.

The focusing spot size is evaluated by examining maximum amplitude data. This method has been used in previous experiments and is described in Section 4.3. The maximum amplitude over the entire time record is recorded at each measurement point in the scan region. This data is appropriately normalized using the techniques described in Sections 8.2.2 and 8.2.3. A trend is clearly present towards a larger spot size as the noise level increases, but the trend is not entirely consistent over the range of amplitudes and noise levels (Figure 102). This inconsistency is most likely due to the fact that any changes in focusing spot size are well within the measurement error of the sensor array due to the 3.429 cm spacing between the accelerometer array elements.

The array used in these experiments consists of 30 accelerometers in a 3 x 10

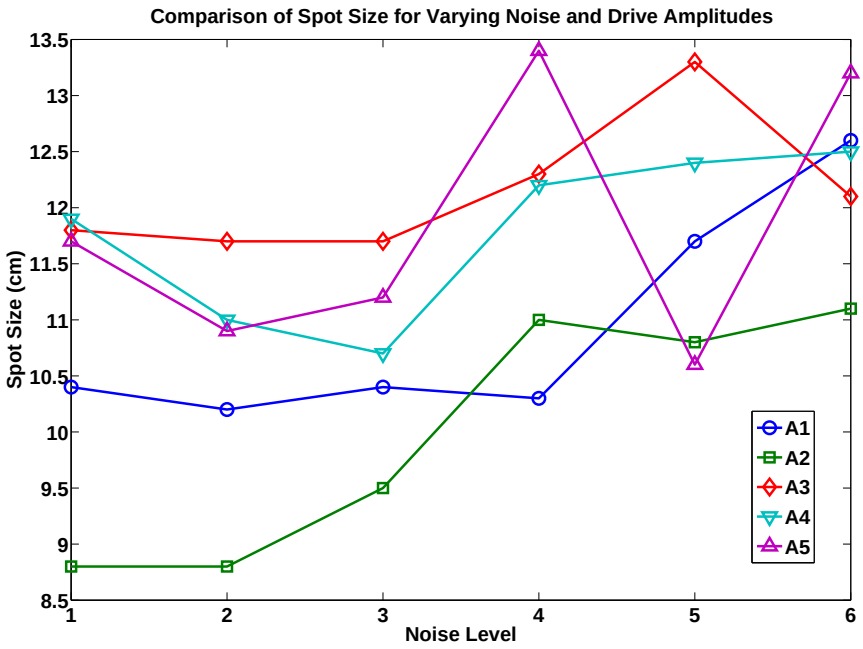

Figure 102: The time-reversal focusing spot size versus noise level and drive signal amplitude.

array spaced 3.429 cm apart in X and 10.287 cm in Y. The array and data collection procedure has been described previously in Section 4.2.1, and Figure 34. The measurements from the array are interlaced along the Y direction to synthetically generate a grid of measurement points with a spacing of 3.429 cm between measurement points in both X and Y (Figure 35). Because of the spacing between elements, spatial sampling limits the ability of the array to fully resolve the focus width.

8.3.3 Maximum Amplitude at Focus Point

An analysis of the focusing effectiveness and a measure of high frequency energy loss have been presented. Both of these metrics are self-normalized metrics; they measure signal energy or amplitude in relation to their own peak level or total energy. This type of normalization is appropriate for measurements where peak amplitude is less important, such as when measuring a self-contained ratio or a 6 dB spot width. Self-normalization does not allow for an adequate comparison of performance of real

efficiency of energy transfer or of actual amplitude. A comparison of peak focusing amplitudes allows for signals to be normalized to a common standard using the procedure described in Section 8.2.3 and then compared. The results demonstrate in absolute terms which excitation signals are most efficient at delivering high amplitude signals to the desired focus point.

Figure 103 shows the results of the maximum amplitude data for the noise levels vs. drive amplitude matrix of excitation signals. The results show that as the amplitude of the drive signal is increased, the peak amplitude at the focus point decreases. The trend is observable once the data has been normalized with respect to the energy that was contained in the excitation signal. This trend is consistent with the fact that the source-ground coupling becomes less efficient as the drive level increases. A second notable trend is that as noise amplitudes increase, peak signal levels at the focus point decrease. This trend is consistent with the effects described in Section 8.3.1, where focusing effectiveness was reduced by increasing noise levels. As the amplitude of the noise signal increases in relation to the clean drive signal, the composite signal becomes more non-linear and less efficient at transmitting energy to the focus point. Note that there is one anomalous measurement on the Amplitude 4 curve in Figure 103. This data point holds no experimental significance. It is a result of either a spurious measurement or a glitch that occurred during the data collection process of the experiment, but is included here for completeness.

8.4 Drive Signal Truncation

8.4.1 Truncation Method

In generating the time-reversal focusing results, a swept frequency chirp signal as described in Section 2.3.2 is always used as the initial experimental excitation signal. The chirp serves as an excellent interrogation signal because it allows energy to be spread out in time as the chirp sweeps through the frequency range of interest.

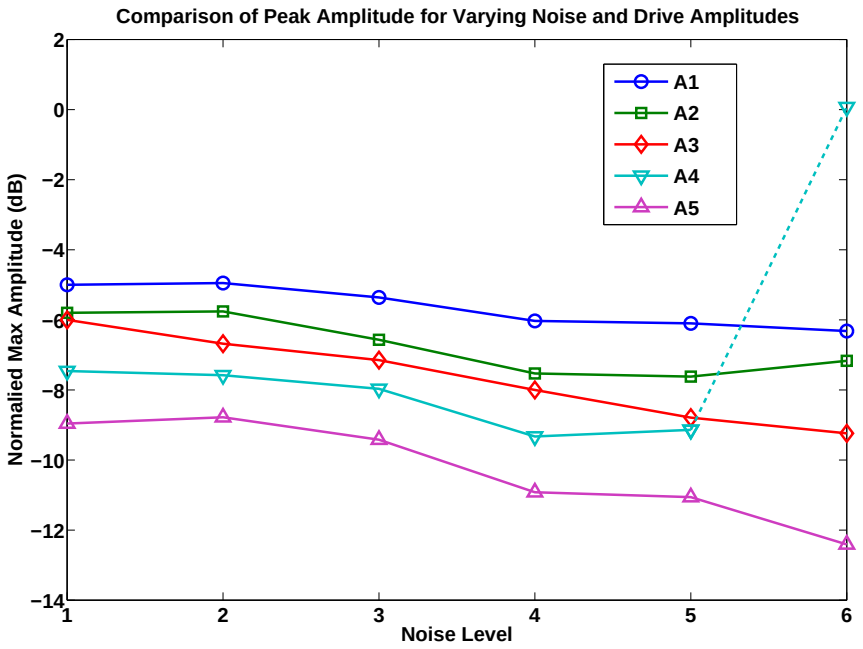

Figure 103: A comparison of normalized peak amplitudes at the focus point. The data is presented for all 6 noise levels, $N_1 - N_5$ and all 5 amplitude levels, $A_1 - A_5$.

Spreading the energy in time allows for lower amplitudes to be excited for longer periods of time, thereby minimizing the non-linear excitation that is caused by high amplitude excitations.

Choosing an interrogation signal with a long time duration also offers an opportunity to improve the signal-to-noise ratio by averaging noise over a long period. While the chirp signal is used as the interrogation pulse, the data is analyzed with respect to a differentiated Gaussian pulse. After the response to the chirp signal is recorded in the sand tank, it is transformed to the frequency domain and then the frequency domain transfer function of the chirp signal is removed. The remaining signal is the frequency domain impulse response of the experimental system, as was described in Equation 46 in Section 4.2.2. This impulse response is then convolved with a differentiated Gaussian pulse for analysis. As described in Section 4.2.2, the compression of the experimental data into a differentiated Gaussian pulse results in a signal that

is largely quiescent over the 4.096 s that are recorded. This means that the signal energy is concentrated over a very short duration, while the noise remains spread out over the entire time period, effectively improving the signal-to-noise ratio over the duration of the compressed pulse.

Section 4.2.2 described the use of a method to improve the signal-to-noise ratio of the time-reversal drive signal that employs pulse compression and signal truncation. The response to a chirp excitation is recorded at the focus point, then the impulse response is extracted from this data. Once the signal is compressed in the form of an impulse response, a ring-down can be observed as the response settles from the peak of the impulse (Figure 104). Recalling the description of the frequency domain transfer function from Equation 46, the pulse-compressed response at the focus point can be written as,

$$D(t) = \mathcal{F}^{-1}\Big\{T(f)\mathcal{F}\left\{\gamma(t)\right\}\Big\}. \tag{69}$$

After the ring-down, the rest of the signal should be nearly quiescent. During this quiescent period, noise overwhelms any contribution from the actual signal (Figure 105). Because there is a long period of time when noise obscures any signal contribution, that time segment of the signal may be removed by truncating the recorded signal and then zero-padding it to return it to its original length of 4.096 seconds (Figure 106). This procedure further improves the signal-to-noise ratio of the data with respect to a differentiated Gaussian pulse.

In addition to the improvements in signal-to-noise ratio, use of the chirp signal has another effect on the results: it allows for partial temporal separation of the quasi-linear and non-linear components of the response. This separation occurs when the chirp transfer function is removed from the recorded signal data. Because the chirp is swept frequency, any component at frequency, f_0 is only excited at a time, t_0. The energy from this frequency component should arrive at the focus point after

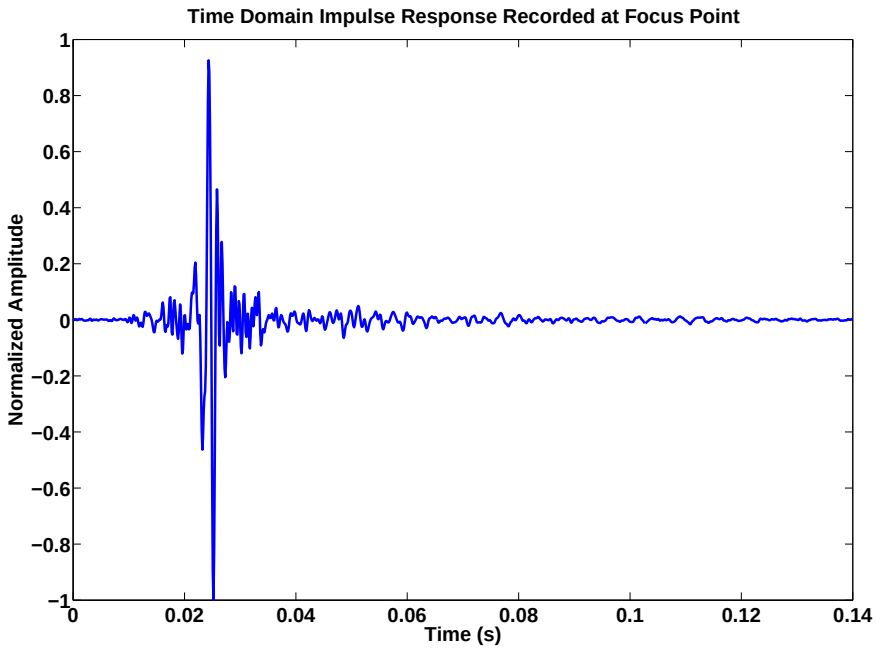

Figure 104: The time domain impulse response of the experimental system when recorded at the focus point. The entire response is 4.096 s long, but here the response is only shown for a portion of that time window.

some propagation delay (t_δ) at time $t_0 + t_\delta$. If instead, energy excited in the chirp at f_0 and t_0 is non-linear, some of this energy will arrive at the focus point as energy at some higher frequency f_1, but it will still arrive at the focus point at time $t_0 + t_\delta$. Linear energy transmitted at f_1 and time t_1 will arrive at the focus point at time $t_1 + t_\delta$.

When the signal is compressed later, the nonlinear component of $f_0 \Rightarrow f_1$ arrives at the focus point $t_1 - t_0$ seconds earlier than the linear component of f_1 that arrives at $t_1 + t_\delta$. These "early time" non-linear arrivals appear as late-time arrivals when analyzing the data because of the circular nature of the Fourier transform that is employed during pulse compression. When this resulting data is compressed to an impulse function, it becomes possible to separate the linear and non-linear components of the data. Figure 107 demonstrates this effect. The response to a large amplitude chirp excitation is recorded at a single point in the sand tank and then converted to

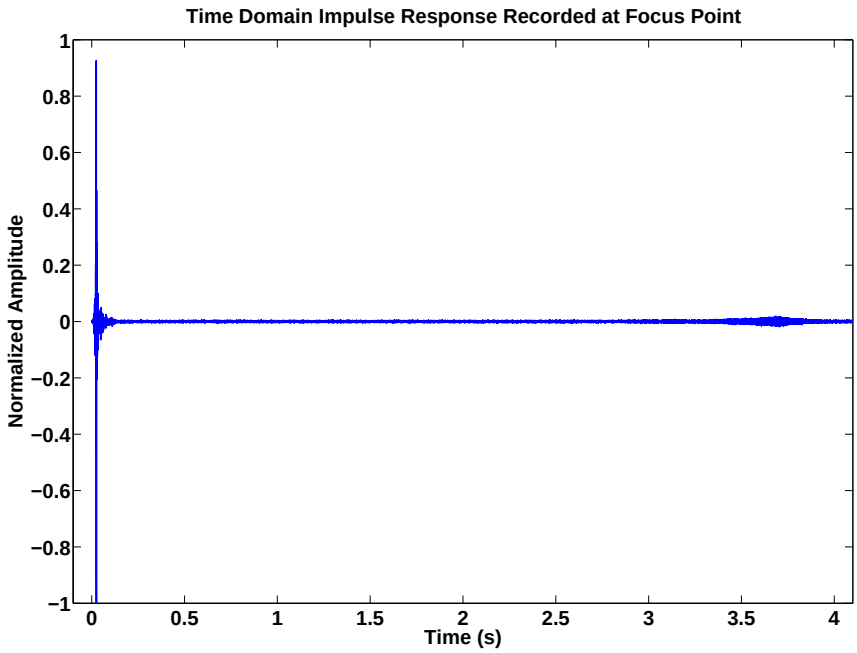

Figure 105: The full-length view of the impulse response. The impulse occurs at the beginning of the time record. A small amount of "late time" nonlinear energy is also observable from approximately 3.4 - 3.8 s.

an impulse response before being compressed with a differentiated Gaussian pulse. The large pulse near the beginning of the time record is the linear impulse response, while the smaller pulse near the end of the time record is the non-linear portion of the impulse response.

The purpose of this experiment is to examine drive signal truncation and its impacts on time-reversal focusing. Drive signal truncation affects two key parameters of the drive signal: the transmission or omission of the non-linear component of the drive signal, and the noise level in the signal. If the drive signal is truncated short enough that it removes some critical part of the signal before the ring down is complete, this could have an adverse impact on the effectiveness of time-reversal focusing. This experiment will examine the effects of drive signal truncation for a quasi-linear (A1) and a quasi-nonlinear amplitude (A4). The truncation length will be varied such that some portion of the original signal is retained. The length of the

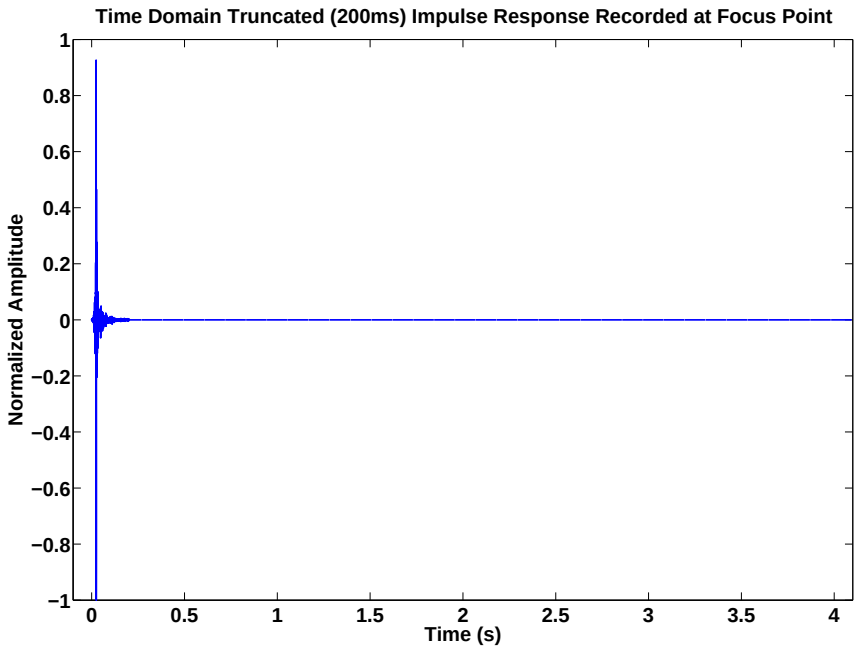

Figure 106: The full length impulse response after truncation and zero padding. The first 200 ms are the original signal while the remainder of the signal has been forced to zero.

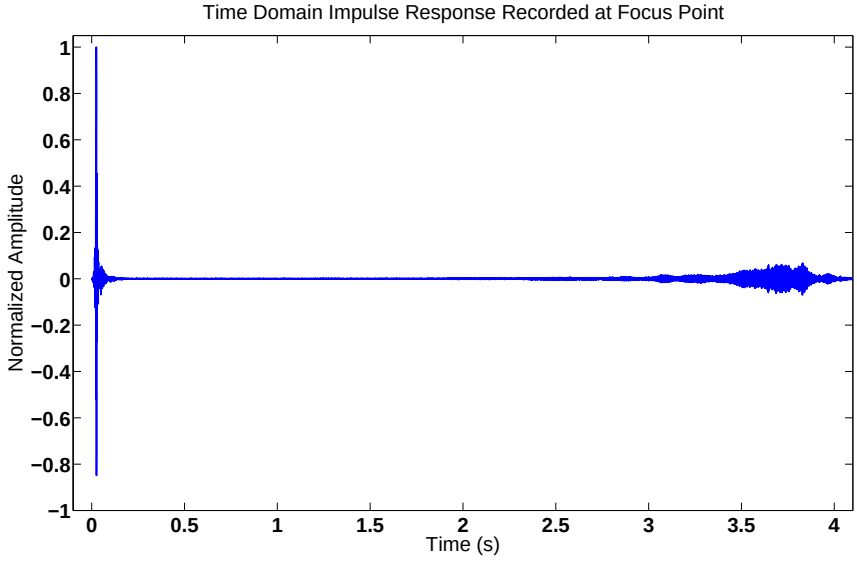

Figure 107: The time domain impulse response to a signal with a large nonlinear component appearing in "late time."

retained portion will vary from 200 ms to the entire 4.096 s signal. Five truncation lengths will be examined: 200 ms, 3 s, 3.5 s, 4 s and 4.096 s.

8.4.2 Normalization Method

Each of the experiments is normalized using a normalization procedure described in Sections 8.2.2 and 8.2.3 except for the changes listed here. The procedure for creating an averaged time-domain transfer function is the same, as described by Equation 54. At this point, the truncation length may be varied such that instead of a static 200 ms truncation length (as in Equation 49), $T_{truncated}$ is now,

$$T_{truncated}(t, m) = T_F(t, m)W_T(t), \tag{70}$$

where $W_T(t)$ is a window function defined in the time domain as,

$$W_T(t) = \begin{cases} 1 & : \quad 0 \leq t \leq t_0 \text{ ms} \\ 0 & : \quad t_0 \text{ ms} < t \leq 4.096 \text{ s}. \end{cases} \tag{71}$$

In Equation 71, t_0 is any one of five lengths: 200 ms, 3 s, 3.5 s, 4.0 s, or 4.096 s.

Each set of signals of a constant amplitude, (A_1 or A_4), has a set of 5 different truncation lengths: 200 ms, 3 s, 3.5 s, 4.0 s, and 4.096 s. These signals are normalized, but amplitude set is normalized as a group, so now for the signals of amplitude A_m, their normalization constant is,

$$NORM_{A_m} = \max_k \left(\max_t (T_{truncated_k}(t, m)) \right) \tag{72}$$

where k is the truncation length (200 ms, 3 s, etc.). The purpose of this single normalization is that these are essentially the same signal, just with different amounts of non-linear energy included. If we want to evaluate the effect of adding that non-linear energy back in, the non-linear energy should all be transmitted at the same amplitude in the time-reversal focusing experiment. This avoids the undesired addition of

additional nonlinearity caused by changes in the normalization factor. Since no noise signals are added in this experiment, the second normalization performed in Equation 62is redundant, and therefore not performed. Aside from these minor changes, the normalization and equalization methods for are the same as those described in Sections 8.2.2 and 8.2.3.

8.4.3 Results

The effects of the drive signal truncation on time-reversal focusing are first evaluated by considering the peak amplitude at the focus point. Each of the experiments is normalized using the normalization procedure described in Section 8.4.2. Figure 108 demonstrates that as the portion of the retained signal becomes longer, the peak amplitude at the focusing location decreases. Note that as the retained signal becomes longer the total energy in the drive signal is actually increasing, which, by itself, should push the peak amplitude higher. There are two explanations for the observed trend, which counters the traditional expectations.

First, longer signals have the effect of being noisier as was described in Section 8.4.1, so this result is consistent with the conclusions drawn in Section 8.3 that noise adversely effects time-reversal focusing. The additional noise in the drive signals results in effectively reducing the amplitude of the composite signal due to the normalization which is required to prevent additional non-linearity (See Section 8.3).

Second, a significant drop in the peak focusing amplitude is noted when the length of the truncated drive signal goes beyond 3 s (Figure 108). This is caused by the non-linearity that appears in late time due to the effects described earlier in this section. The drop in peak focusing amplitude is more pronounced for the higher amplitude excitation signals since the effect is based on the non-linearity of the signals. For the smaller amplitude (A1) signals, there is a slight upward trend from the 4 to 4.096 s points on the peak amplitude plot. It should be noted that this represents a change

of approximately 0.05 dB and is therefore within the range of a measurement error.

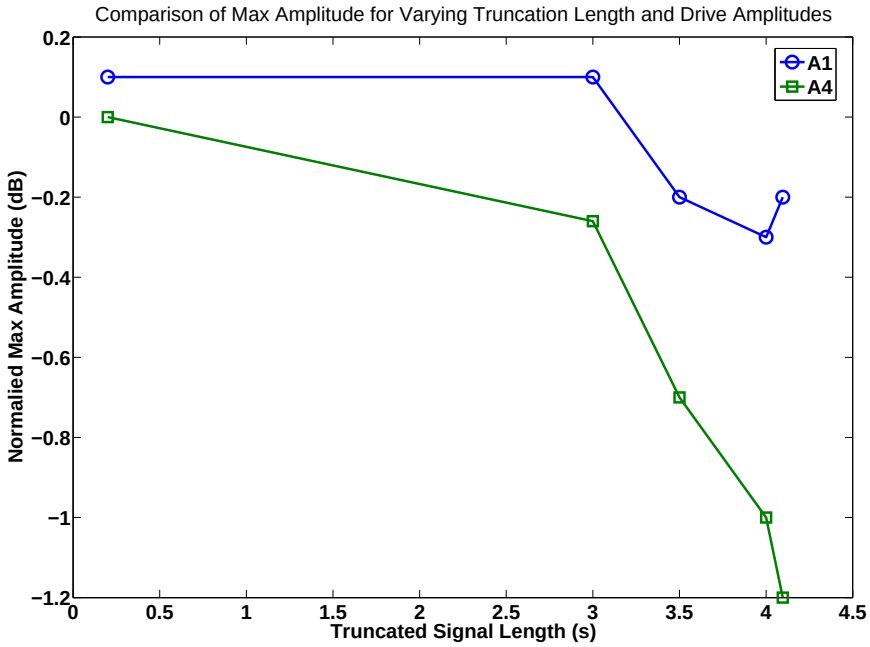

Figure 108: A comparison of the normalized peak amplitude at a focus point. Data is presented of varying truncation lengths for quasi-linear (A1) and quasi-non-linear (A4) excitation signals.

The impact of changes in the truncation length on the focusing effectiveness for time-reversal focusing can be effectively assessed using the focusing spot size ratio described in Section 4.3 and used in Section 8.3.2. Figure 109 demonstrates that for both the quasi-linear and quasi-nonlinear amplitudes, the focusing effectiveness drops off significantly as the un-truncated portion of the signal becomes longer. While additional noise in the signal may play a role in this, the effect of the nonlinearity is the dominant one. This is shown by the fact that the spot size for the A4 curve increases much more quickly than for the smaller amplitude A1 curve. As the nonlinear portions of the signal are re-introduced and the signal lengthens, focusing effectiveness begins to decline rapidly. This drop is more pronounced and more significant for the signals of amplitude A_4 with more non-linear content.

The measurement error due to the 3.429 cm spacing of the accelerometer array

elements will again prove to be a limiting factor for the spot size measurement. This means that the changes in spot size for the A_1 curve may be statistically insignificant, but the changes for the non-linear A_4 curve demonstrate a clear trend, increasing the spot size approximately than half of the spacing between accelerometers, yielding a result that demonstrates that non-linearity in the time-reversal process does adversely affect focusing effectiveness.

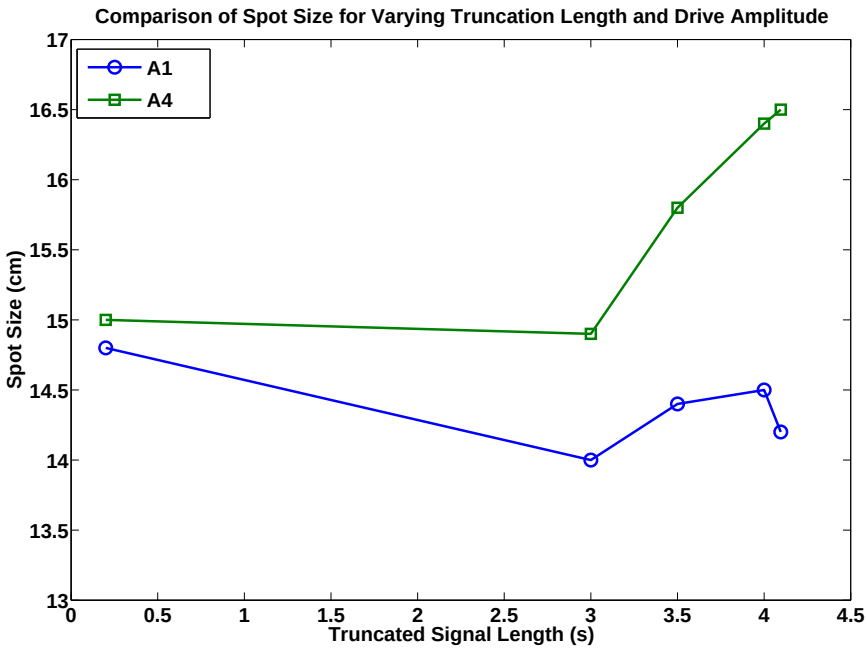

Figure 109: A comparison of the focusing spot size for varying truncation lengths for quasi-linear (A1) and quasi-non-linear (A4) excitation signals. All data is for the same focus point.

CHAPTER IX

CONCLUSION

This dissertation has investigated the behavior of time-reversal focusing in soils, which behaved as a quasi-linear elastic media. The investigation of time-reversal focusing began with a basic study of time-reversal using a linear finite-difference time-domain model of the soil. This computational model allowed time-reversal focusing to be studied in a linear, noise-free context. Initial numerical models showed time-reversal focusing to be effective in elastic media, including when a large number of scattering objects were present in the medium. When scattering objects were present, time-reversal focusing demonstrated superior focusing ability when compared to other excitation methods such as uniform excitation or time-delay focusing.

The numerical studies were followed by multiple investigations of experimental time-reversal focusing performed in sand. Time-reversal focusing effectiveness was evaluated first for experimental conditions similar to the numerical model, with multiple near-surface scattering objects present in the medium. Time-reversal focusing was shown to be effective in the experimental context as well. Further experiments examined time-reversal focusing in the more extreme case where the entire ballistic wave was blocked, and the only energy reaching the focus point was reflected from scattering objects in the medium. Time-reversal focusing was effective in focusing the remaining energy to the focus location which was in a shadowed region behind the large barrier that blocked the ballistic wave. A comparison to other focusing methods demonstrated that under these conditions, most focusing attempts with traditional methods will fail completely while time-reversal focusing does not.

Additional configurations of time-reversal focusing examined its effectiveness when scattering came from several different asymmetrical surface layers that altered the

propagation direction of the wavefronts as they left the source array. Time-reversal focusing was able to effectively direct energy to the focus point even when wavefronts were steered away from the focus location by the asymmetric surface layer. Continuing with investigations of asymmetry in time-reversal focusing, the impact of an asymmetrical or non-uniform excitation array was examined for time-reversal focusing in the presence of scattering objects. The results demonstrated that time-reversal performs well, and maintains a distinct advantage over other excitation methods. Time-reversal preferentially excites sources that have a more clear path to the focus point. This results in more energy being delivered to the focus location than for traditional methods, such as time-delay focusing.

In the previous experiments experimental time-reversal focusing provided significant gains over other excitation methods when scattering objects were present, but it failed to provide focusing resolutions as high those that were predicted by both the initial numerical investigations of time-reversal focusing and that have been predicted by other studies [2, 11, 12]. An investigation of the effects of scattering object geometry was undertaken to examine the effect scattering object shape, orientation, and number of scattering objects on focusing resolution in time-reversal focusing. Scattering object field density was found to have a strong, but diminishing effect on focusing resolution as the scattering object field density increased. Loss of surface wave energy available for focusing due to mode-conversion was found to be correlated with the density of the scattering object field. Initial data suggests that scattering object shape may also have some impact on the amount of energy lost to mode conversion.

Soil is a complicated non-linear medium which normally behaves in a quasi-linear fashion for the range of amplitudes in which the earlier experiments were performed. The impact of the weak non-linear nature of the soil on time-reversal focusing was examined through a study of time-reversal focusing behavior for a variety of amplitudes that generate different levels of non-linearity in the soil. This study of nonlinearity

was coupled with a study of the impact of noise on time-reversal focusing. It was determined that both non-linearity and noise have an impact on time-reversal focusing effectiveness. Further, the loss from these mechanisms seems to be interrelated. Noise seems to enhance non-linear loss in the soil.

REFERENCES

[1] Ing, R., Fink, M., and Casula, O., "Self-focusing rayleigh wave using a time reversal mirror," *Appl. Phys. Lett.*, vol. 68, pp. 161–163, Jan. 1996.

[2] Derode, A., Roux, P., and Fink, M., "Robust acoustic time reversal with high-order multiple scattering," *Phys. Rev. Lett.*, vol. 75, pp. 4206–4209, Dec. 1995.

[3] Scott, Jr., W. R., Martin, J. S., and Larson, G. D., "Experimental model for a seismic landmine detection system," *IEEE Trans. on Geoscience and Remote Sensing*, vol. 39, pp. 1155–1164, June 2001.

[4] Fink, M., Prada, C., Wu, F., and Cassereau, D., "Self focusing in inhomogeneous media with time reversal acoustic mirrors," *IEEE Ultrason. Symp.*, pp. 681–686, 1989.

[5] Fink, M., "Time-reversal of ultrasonic fields—part i: Basic principles," *IEEE Trans. Ultrason., Ferroelec., Freq. Contr.*, vol. 39, pp. 555–566, Sept. 1992.

[6] Wu, F., Thomas, J.-L., and Fink, M., "Time-reversal of ultrasonic fields—part ii: Experimental results," *IEEE Trans. Ultrason., Ferroelec., Freq. Contr.*, vol. 39, pp. 567–578, Sept. 1992.

[7] Carsten Draeger, D. C. and Fink, M., "Theory of time-reversal process in solids," *J. Acoust. Soc. Am.*, vol. 102, pp. 1289–1295, Sept. 1997.

[8] Chakroun, N., Fink, M. A., and Wu, F., "Time reversal processing in ultrasonic nondestructive testing," *IEEE Trans. Ultrason., Ferroelec., Freq. Contr.*, vol. 42, pp. 1087–1098, Nov. 1995.

[9] Achenbach, J. D. D., *Wave Propagation in Elastic Solids.* North-Holland, Jan. 1984.

[10] Carsten Draeger, D. C. and Fink, M., "Theory of time-reversal process in solids," *J. Acoust. Soc. Am.*, vol. 102, pp. 1289–1295, Sept. 1997.

[11] Borcea, L., Papanicolaou, G., and Tsogka, C., "Theory and applications of time reversal and interferometric imaging," *Inverse Problems*, vol. 19, pp. S139–S164, Apr. 2003.

[12] Blomgren, P., Papanicolaou, G., and Zhao, H., "Super-resolution in time-reversal acoustics," *J. Acoust. Soc. Am.*, vol. 111, pp. 230–248, Jan. 2002.

[13] Alexander M. Sutin, James A. TenCate, P. A. J., "Single-channel time reversal in elastic solids," *J. Acoust. Soc. Am.*, vol. 116, pp. 2779–2784, Nov. 2004.

[14] J. Carlos Santamarina, K. A. K. and Bracewell, M. A. F. N., *Soils and Waves*. West Sussex, England: John Wiley and Sons, LTD, 2001.

[15] Schröder, C. T., *On the Interaction of Elastic Waves with Buried Land Mines: an Investigation Using the Finite-Difference Time-Domain Method*. PhD thesis, Georgia Institute of Technology, July 2001.

[16] Martin, J. S., Scott, Jr., W. R., Larson, G. D., Rogers, P. H., and II, G. S. M., "Probing signal design for seismic landmine detection," *Proc. SPIE Defense and Security Symposium*, vol. 5415, Apr. 2004.

[17] Bracewell, R. N., *The Fourier Transform and Its Applications*. New York, NY: McGraw-Hill, third ed., 2000.

[18] Norville, P. D., Scott, Jr., W. R., and Larson, G. D., "An investigation of time reversal techniques in seismic landmine detection," *Proc. SPIE Defense and Security Symposium*, vol. 5415, Apr. 2004.

[19] Lamb, H., "On the propagation of tremors over the surgace of an elastic solid," *Phil. Trans. R. Soc.*, vol. A203, pp. 1–42, 1904.

[20] Viktorov, I., *Rayleigh and Lamb waves: physical theory and applications*. Plenum Press, 1967.

[21] Graff, K. F., *Wave Motion in Elastic Solids*. Oxford University Press, 1975.

[22] W.M Ewing, W. J. and Press, F., *Elastic waves in layered media*. McGraw-Hill, 1957.

[23] Miller, G. and Pursey, H., "On the partition of energy between elastic waves in a semi-infinite solid," *Proc. R. Soc.*, vol. A223, pp. 55–69, 1955.

[24] Auld, B. A., *Acoustic Fields and Waves in Solids*. Robert E. Krieger Publishing Company, 1990.

[25] Miller, G. and Pursey, H., "The field and radiation impedance of mechanical radiators on the free surface of a semi-infinite isotropic solid," *Proc. R. Soc.*, vol. A223, pp. 521–541, 1954.

[26] Cangellaris, A. C. and Wright, D. B., "Analysis of the numerical error caused by the stair-stepped approximation of a conducting boundary in fdtd simulations of electromagnetic phenomena," *IEEE Trans. on Antennas and Propagation*, vol. 39, pp. 1518–1525, Oct. 1991.

[27] Holland, R., "Pitfalls of staircase meshing," *IEEE Trans. on Electromagnetic Compatibility*, vol. 35, pp. 434–439, Nov. 1993.

[28] Norville, P. D. and Scott, Jr., W. R., "An investigation of time reversal techniques in seismic landmine detection," *J. Acoust. Soc. Am*, vol. 118, pp. 735–744, Aug. 2005.

[29] Alam, M. and McClellan, J. H., "Near field imaging of subsurface targest using active arrays and elastic waves," *IEEE Digital Signal Processing Workshop*, Aug. 2004.

[30] Alam, M., McClellan, J. H., Norville, P. D., and Scott, Jr., W. R., "Time-reverse imaging for the detection of landmines," *Proc. SPIE Defense and Security Symposium*, vol. 5415, Apr. 2004.

[31] Alam, M., McClellan, J. H., and Scott, Jr., W. R., "Multi-channel spectrum analysis of surface waves," *37th Asilomar Conference on Signals, Systems and Computers*, 2003.

[32] Steiglitz, K. and McBride, L., "A technique for the identification of linear systems," *IEEE Trans. Atomat. Contr.*, vol. AC-10, pp. 461–464, 1965.

[33] James S. Martin, G. D. L. and Scott, Jr., W. R., "An investigation of surface-contacting sensors for the seismic detection of buried landmines," *J. Acoust. Soc. Am*, vol. 120, pp. 2676–2685, Nov. 2006.

[34] Gregg D. Larson, James S. Martin, P. H. R. W. R. S. and McCall, II, G. S., "Impact of non-linear effects on high-frequency seismic landmine detection," *Demining Technology Forum Information Journal*, vol. 3, no. 20, 2002.

[35] Derode, A. and Fink, M., "Partial coherence of transient ultrasonic fields in anisotropic random media: Application to coherent echo detection," *J. Acoust. Soc. Am.*, vol. 101, pp. 690–704, July 1997.

[36] Mickael Tanter, J.-L. T. and Fink, M., "Influence of boundary conditions on time reversal focusing through heterogeneous media," *Appl. Phys. Lett.*, vol. 72, pp. 2511–2514, May 1999.

[37] Mickael Tanter, J.-L. T. and Fink, M., "Time reversal and the inverse filter," *J. Acoust. Soc. Am.*, vol. 108, pp. 223–234, July 2000.

[38] Thomas, J.-L., Roux, P., and Fink, M., "Inverse problem in wave scattering with an acoustic time-reversal mirror," *IEEE Ultrason. Symp.*, pp. 1143–1148, 1993.

[39] Thomas, J.-L., Wu, F., and Fink, M., "Self focusing on extended objects with time reversal mirror, applications to lithotripsy," *IEEE Ultrason. Symp.*, pp. 1809–1814, 1994.

[40] Casserau, D. and Fink, M., "Time-reversal of ultrasonic fields—part iii: Theory of the closed time-reversal cavity," *IEEE Trans. Ultrason., Ferroelec., Freq. Contr.*, vol. 39, pp. 579–592, Sept. 1992.

[41] Alam, M., Cever, V., McClellan, J. H., Larson, G. D., and Scott, Jr., W. R., "Optimal maneuvering of seismic sensors for localization of subsurface targets," *Trans. on Geoscience and Remote Sensing*, 2007.

VITA

Pelham Norville was born in Mobile, Alabama, USA in 1979. He graduated with a B.S. degree in electrical engineering from Auburn University, Auburn, AL in 2001. He continued his education at the Georgia Institute of Technology where he received an M.S. degree in Electrical and Computer Engineering in 2003 and a Masters of Business Administration (MBA) and Ph.D. in electrical and computer engineering in 2007. His technical interests include wave propagation, acoustics, seismic detection of buried objects, time-reversal focusing and numerical modelling of wave propagation using the finite-difference time-domain technique.